

# WADD-ASD-TDR-62-475

ASD-TDR-62-475

B-1

## RESPONSE OF MISSILE STRUCTURES TO IMPULSE LOADING

TECHNICAL DOCUMENTARY REPORT ASD-TDR-62-475

MARCH 1963

**Reproduced From  
Best Available Copy**

Flight Dynamics Laboratory  
Aeronautical Systems Division  
Air Force Systems Command  
Wright-Patterson Air Force Base, Ohio

**DISTRIBUTION STATEMENT A**  
Approved for Public Release  
Distribution Unlimited

Project No. 6906, Task No. 690601

# 20011030 043

[Prepared under Contract No. AF 33(616)-7956

by

T. Wah

L. U. Rastrelli

N. L. Basdekas

R. C. DeHart

Southwest Research Institute, San Antonio 6, Texas]

6289

Lovelace Foundation - Document Library

Aerospace Medicine and Biocastrology

## NOTICES

When Government drawings, specifications, or other data are used for any purpose other than in connection with a definitely related Government procurement operation, the United States Government thereby incurs no responsibility nor any obligation whatsoever; and the fact that the Government may have formulated, furnished, or in any way supplied the said drawings, specifications, or other data, is not to be regarded by implication or otherwise as in any manner licensing the holder or any other person or corporation, or conveying any rights or permission to manufacture, use, or sell any patented invention that may in any way be related thereto.

Qualified requesters may obtain copies of this report from the Armed Services Technical Information Agency, (ASTIA), Arlington Hall Station, Arlington 12, Virginia.

This report has been released to the Office of Technical Services, U.S. Department of Commerce, Washington 25, D.C., in stock quantities for sale to the general public.

Copies of this report should not be returned to the Aeronautical Systems Division unless return is required by security considerations, contractual obligations, or notice on a specific document.

## FOREWORD

This Project, (6906) "Nuclear Weapon Effects on Space Vehicles;" and Task, (690601) "Determination of High Altitude Nuclear Weapon Effects on Space Vehicles," are a part of the Air Force Systems Command applied research program 710A," NUCLEAR WEAPONS EFFECTS."

The study was initiated by the Flight Dynamics Laboratory, WWRMD, under Project No. 6906, Task No. 690601. The project officer was Mr. L. E. Gilbert. The investigation was conducted by the Southwest Research Institute during the period from 1 March 1961 through 31 March 1962.


## ABSTRACT

Procedures for analytically predicting the response of missile bodies to blast loadings are presented. The investigation involves the behavior of cylindrical shells (with various end-closures) and circular, flat plates. The numerical results obtained from the analytical methods compare favorably with the experimental data acquired during the study.

## PUBLICATION REVIEW

This technical documentary report has been reviewed and is approved.

FOR THE COMMANDER:

  
RICHARD F. HOENER  
Chief, Structures Branch  
Flight Dynamics Laboratory

# TABLE OF CONTENTS

	<u>Page</u>
1. INTRODUCTION . . . . .	1
2. ANALYTICAL PROCEDURES . . . . .	2
2.1 Response of Cylindrical Shells to Impulsive Loadings . . . . .	2
2.1.1 Linear-Elastic, Small Deflection Theory . . . . .	2
2.1.2 Linear-Elastic, Large Deflection Theory . . . . .	6
2.2 Dynamic Response of Circular Plates . . . . .	13
2.2.1 Large Amplitudes . . . . .	13
2.2.1.1 Equations of Motion . . . . .	14
2.2.1.2 Integration Procedure . . . . .	15
2.2.1.3 Forced Vibration . . . . .	19
2.2.1.4 Summary of Integration Procedure . . . . .	21
2.2.1.5 Numerical Example . . . . .	24
2.2.2 Plastic Collapse . . . . .	26
2.2.2.1 Summary of the Hudson Approach . . . . .	27
2.2.2.2 An Elementary Approximation to the Solution . . . . .	27
2.2.2.3 The Exact Solution for a Rigid-Perfectly Plastic Material . . . . .	29
2.2.2.4 General Remarks . . . . .	30
References . . . . .	32
3. NUMERICAL ANALYSIS - CYLINDRICAL SHELLS (LINEAR-ELASTIC, SMALL DEFLECTIONS) . . . . .	33
3.1 Simply Supported End-Closures . . . . .	33
3.2 Fixed End-Closures . . . . .	34
3.3 Elastic End-Closures . . . . .	50
4. DISCUSSION . . . . .	55
APPENDIX I - METHODS OF ANALYSIS (LINEAR-ELASTIC, SMALL DEFLECTION THEORY) . . . . .	59
I.1 Frequency and Displacement Equations . . . . .	61
I.2 Lagrangian Equations of Motion . . . . .	65
I.3 Development of Load Spectrums . . . . .	68
References . . . . .	76
APPENDIX II - EXPERIMENTAL PROGRAM . . . . .	77
II.1 Objectives . . . . .	77
II.2 Model Design . . . . .	77
II.2.1 Cylindrical Shells . . . . .	77
II.2.2 Circular Flat Plates . . . . .	77
II.3 Instrumentation . . . . .	77
II.4 Test Program . . . . .	77
APPENDIX III - EXPERIMENTAL RESULTS . . . . .	89
III.1 Pressure-Time Measurements . . . . .	89
III.2 High-Speed Photography Data . . . . .	93
References . . . . .	102

# LIST OF ILLUSTRATIONS

Figure		Page
2.1	Variation of Frequency Parameter with Stiffness Parameter . . . . .	7
2.2	Variation of Time Function With $\tau(t)$ . . . . .	12
2.3	A Sketch of the Diaphragm Configurations at Two Successive Instants, $t$ and $t+dt$ . The Various Quantities Which Enter into the Several Geometric and Kinematic Relations are Portrayed Here . . . . .	28
3.1	Variation of Loading Function with Time . . . . .	35
3.2	Variation of $q_{mn}(t)$ and Radial Displacement $w(t)$ at $x = L/2$ , $\phi = 0^\circ$ for Cylindrical Shell . . . . .	37
3.3	Variation of $q_{mn}(t)$ and Radial Displacement $w(t)$ at $x = L/2$ , $\phi = 0^\circ$ for Cylindrical Shell . . . . .	37
3.4	Variation of $q_{mn}(t)$ and Radial Displacement $w(t)$ at $x = L/2$ , $\phi = 0^\circ$ for Cylindrical Shell . . . . .	38
3.5	Variation of $q_{mn}(t)$ and Radial Displacement $w(t)$ at $x = L/2$ , $\phi = 0^\circ$ for Cylindrical Shell . . . . .	38
3.6	Variation of $q_{mn}(t)$ and Radial Displacement $w(t)$ at $x = L/2$ , $\phi = 0^\circ$ for Cylindrical Shell . . . . .	39
3.7	Variation of $q_{mn}(t)$ and Radial Displacement $w(t)$ at $x = L/2$ , $\phi = 0^\circ$ for Cylindrical Shell . . . . .	39
3.8	Variation of $q_{mn}(t)$ and Radial Displacement $w(t)$ at $x = L/2$ , $\phi = 0^\circ$ for Cylindrical Shell . . . . .	40
3.9	Variation of $q_{mn}(t)$ and Radial Displacement $w(t)$ at $x = L/2$ , $\phi = 0^\circ$ for Cylindrical Shell . . . . .	40
3.10	Variation of $q_{mn}(t)$ and Radial Displacement $w(t)$ at $x = L/2$ , $\phi = 0^\circ$ for Cylindrical Shell . . . . .	41
3.11	Variation of $q_{mn}(t)$ and Radial Displacement $w(t)$ at $x = L/2$ , $\phi = 0^\circ$ for Cylindrical Shell . . . . .	41
3.12	Variation of $q_{mn}(t)$ and Radial Displacement $w(t)$ at $x = L/2$ , $\phi = 0^\circ$ for Cylindrical Shell . . . . .	42
3.13	Variation of $q_{mn}(t)$ and Radial Displacement $w(t)$ at $x = L/2$ , $\phi = 0^\circ$ for Cylindrical Shell . . . . .	42
3.14	Variation of $q_{mn}(t)$ and Radial Displacement $w(t)$ at $x = L/2$ , $\phi = 0^\circ$ for Cylindrical Shell . . . . .	46
3.15	Variation of $q_{mn}(t)$ and Radial Displacement $w(t)$ at $x = L/2$ , $\phi = 0^\circ$ for Cylindrical Shell . . . . .	46
3.16	Variation of $q_{mn}(t)$ and Radial Displacement $w(t)$ at $x = L/2$ , $\phi = 0^\circ$ for Cylindrical Shell . . . . .	47
3.17	Variation of $q_{mn}(t)$ and Radial Displacement $w(t)$ at $x = L/2$ , $\phi = 0^\circ$ for Cylindrical Shell . . . . .	47

# LIST OF ILLUSTRATIONS (Cont'd)

Figure		Page
3.18	Variation of $q_{mn}(t)$ and Radial Displacement $w(t)$ at $x = L/2$ , $\phi = 0^\circ$ for Cylindrical Shell . . . . .	48
3.19	Variation of $q_{mn}(t)$ and Radial Displacement $w(t)$ at $x = L/2$ , $\phi = 0^\circ$ for Cylindrical Shell . . . . .	48
3.20	Variation of Circular Frequency with Elastic Restraint (R) . . . . .	53
3.21	Variation of $q_{mn}(t)$ and Radial Displacement $w(t)$ at $x = L/2$ , $\phi = 0^\circ$ for Cylindrical Shell . . . . .	53
3.22	Variation of $q_{mn}(t)$ and Radial Displacement $w(t)$ at $x = L/2$ , $\phi = 0^\circ$ for Cylindrical Shell . . . . .	54
3.23	Variation of $q_{mn}(t)$ and Radial Displacement $w(t)$ at $x = L/2$ , $\phi = 0^\circ$ for Cylindrical Shell . . . . .	54
4.1	Variation of Maximum Radial Displacement with One-Half of Product of Peak Incident Overpressure and Positive Phase Duration . . . . .	56
I.1	Notation for Cylindrical Shell . . . . .	62
I.2	Cylindrical Shell Stress Resultant Notation . . . . .	62
I.3	Loading Spectrum at Points on Front Half of Cylinder . . . . .	69
I.4	Schematic of Pressure Profile for Shell at Element $\phi = \phi_1$ . . . . .	69
I.5	Incident Overpressure and Dynamic Pressure versus Time . . . . .	72
I.6	Variation of Drag Coefficient with Cylinder Element . . . . .	72
I.7	Time of Arrival of Shock Front on Cylinder Surface . . . . .	73
I.8	Variation of Critical Times ( $t_i$ ) and Diffraction Phase Duration ( $t_D$ ) with Cylinder Element . . . . .	73
I.9	Variation of Critical Pressure ( $P_i$ ) to Peak Incident Overpressure ( $P_I$ ) Ratios with Cylinder Element . . . . .	74
I.10	Pressure Profiles Along Various Elements of Cylindrical Surface . . . . .	74
II.1	Type CC Cylindrical Shell Model . . . . .	78
II.2	Type CA Cylindrical Shell Model . . . . .	78
II.3	Type CB Cylindrical Shell Models . . . . .	79
II.4	Fixture for Circular, Flat Plate Models . . . . .	79
II.5	Model Positions for Shots A1, A2, and A3 . . . . .	82
II.6	Model Positions for Shots B1, B2, and B3 . . . . .	82
II.7	Model Positions for Shots C1 and C2 . . . . .	83
II.8	Model Positions for Shots D, F, G, and H . . . . .	83

# LIST OF ILLUSTRATIONS (Cont'd)

<u>Figure</u>		<u>Page</u>
II. 9	End Plate Failure in Model CC1 after Shot A3 . . . . .	84
II. 10	End Plate and Shell Failure in Model CC1 after Shot B3 . . . . .	84
II. 11	Slight Reduction in Shell Diameter in Model CC2 after Shot B1 . . . . .	85
II. 12	Shell and End Plates Permanent Deformations in Model CC2 after Shot B2 . .	85
II. 13	Shell and End Plate Permanent Deformations in Model CC3 after Shot C1 . . .	86
II. 14	End Plate Deformations in Model CC4 after Shot C7 . . . . .	86
II. 15	End Plate Deformation in Model CC5 after Shot 8 . . . . .	87
II. 16	Shell Deformation in Model CA2 after Shot 7 . . . . .	87
II. 17	Failure State of Models Used in Shots D, F, and H . . . . .	88
III. 1	Peak Overpressure vs Scaled Distance for Spherical TNT in Free-Air at Sea Level . . . . .	90
III. 2	Reflection Factors for TNT Explosions at Low Hob over Various Surfaces . . .	91
III. 3	Peak Overpressure versus Range for TNT . . . . .	92
III. 4	Radial Displacements at $x = L/2$ , $\phi = 0^\circ$ Obtained from High Speed Photograph of Cylindrical Models . . . . .	97
III. 5	Radial Displacements at $x = L/2$ , $\phi = 0^\circ$ Obtained from High Speed Photograph of Cylindrical Models . . . . .	97
III. 6	Radial Displacements at $x = L/2$ , $\phi = 0^\circ$ Obtained from High Speed Photograph of Cylindrical Models . . . . .	98
III. 7	Radial Displacements at $x = L/2$ , $\phi = 0^\circ$ Obtained from High Speed Photograph of Cylindrical Models . . . . .	98
III. 8	Radial Displacements at $x = L/2$ , $\phi = 0^\circ$ Obtained from High Speed Photograph of Cylindrical Models . . . . .	99
III. 9	Radial Displacements at $x = L/2$ , $\phi = 0^\circ$ Obtained from High Speed Photograph of Cylindrical Models . . . . .	99
III. 10	Radial Displacements at $x = L/2$ , $\phi = 0^\circ$ Obtained from High Speed Photograph of Cylindrical Models . . . . .	100
III. 11	Radial Displacements at $x = L/2$ , $\phi = 0^\circ$ Obtained from High Speed Photograph of Cylindrical Models . . . . .	100
III. 12	Radial Displacements at $x = L/2$ , $\phi = 0^\circ$ Obtained from High Speed Photograph of Cylindrical Models . . . . .	101
III. 13	Radial Displacements at $x = L/2$ , $\phi = 0^\circ$ Obtained from High Speed Photograph of Cylindrical Models . . . . .	101

# LIST OF TABLES

<u>Table</u>		<u>Page</u>
3.1	Frequencies and Related Quantities for Cylindrical Shells with Simply Supported End-Closures . . . . .	36
3.2	Computed Maximum Radial Displacements (Columns A) and Corresponding Time of Occurrence (Columns B) at $x = L/2$ , $\phi = 0^\circ$ for Cylinders with Simply-Supported End-Closures . . . . .	43
3.3	Frequencies and Related Quantities for Cylindrical Shells with Fixed End-Closures . . . . .	45
3.4	Computed Maximum Radial Displacements (Columns A) and Corresponding Time of Occurrence (Columns B) at $x = L/2$ , $\phi = 0^\circ$ for Cylinders with End-Closures . .	49
3.5	Frequencies and Related Quantities for Cylinders with Elastic End-Closures . . .	52
4.1	Comparison of Experimental (High-Speed Photography) and Computed (Linear-Elastic, Small Deflection Theory) Radial Displacements for Cylindrical Shells . .	57
I.1	Critical Times and Pressures ( $P_I = 33$ psi, $t_+ = 1$ msec) $D/U = 0.53$ msec . . . . .	75
II.1	Summary of Experimental Program . . . . .	80
III.1	Peak Overpressure in Mach Reflection Region (Experimental Data) . . . . .	94
III.2	Time of Arrival, Positive Phase Duration in Mach Reflection Region (Experimental Data) . . . . .	95
III.3	Summary of Peak Incident Overpressures and Positive Phase Durations . . . . .	96

## 1. INTRODUCTION

In evaluating the vulnerability of missile systems to nuclear antimissile weapons, one aspect of considerable importance is the response of the vehicle's structure. The analytical (and to a lesser extent, the experimental) information presented in this report is directed towards developing procedures for predicting the response of missile bodies as represented by cylindrical shells with various types of end-closures.

Within the concept of structural response, the most significant parameters which constitute a measurement of the damage a missile will sustain as the result of blast loadings are the deformations and accelerations. Consequently, each of the analytical procedures set out to initially define the time dependent variation of the displacement components. Once this is accomplished, it becomes a simple matter to obtain accelerations as functions of time. For the particular shock sensitive components associated with each missile system, this would provide an indication of the critical acceleration forces to be expected.

It is analytically expeditious to subdivide the overall missile structure into two parts, each representing different vulnerability aspects. The first is to consider the cylinders' end-closures only insofar as their restraint contributes to deformational response of the shell. Here, it is implied that the missile shell itself is most vulnerable to nuclear weapon effects. The other approach is to consider the cylinder end-closures themselves. For example, a flat, circular plate would require careful analysis if it can be shown its response is considerably more severe than that experienced by the shell.

Accordingly, in Section 2, comparatively straightforward analytical procedures for acquiring displacements that are reasonably accurate and not unnecessarily laborious are presented. For the cylindrical shell, both the small and large deflection, linear-elastic theories are used. In the small deflection approach, the effect of end-closures (simple, fixed and elastic support) are considered. Two treatments of the circular, flat plate are presented: one entails the dynamic response of circular plates at large amplitudes and the other the plastic collapse of circular plates under blast loadings. Each analytical procedure is carried out in sufficient detail so as to present results which are immediately applicable to specific problems.

In Section 3, extensive numerical computations are presented for the analytical procedure based on the linear-elastic, small displacement shell theory. In evaluating the analytical procedures for predicting the response of cylindrical shell structures to blast loadings, there are several logical, as well as practical, reasons for initially investigating the adequacy of the simplest method. Foremost among these reasons is the fact that these methods provide numerical solutions for a wide variety of variables with a minimum expenditure in computational effort. The extent to which various load and time parameters and certain approximations influence the numerical answers and cause these predicted answers to approach or deviate from the experimental results can be quickly determined.

Moreover, once these numerical solutions are available, they also become of value in forming a foundation for subsequent, more complex analytical procedures. This approach has been adopted in the numerical analysis of the cylindrical shells. In Section 3 are the results of the calculations using analytical methods based on linear-elastic, small displacement theory. Included are comparisons of various combinations of overpressure and positive phase durations.

The information and data obtained in the limited experimental portion of the program are presented in Appendices I and II. These data (involving the radial displacements) are compared with the analytical results in Section 4.

---

Manuscript released by the authors July 1962 for publication as an ASD Technical Documentary Report.

## 2. ANALYTICAL PROCEDURES

### 2.1 Response of Cylindrical Shells to Impulsive Loadings

#### 2.1.1 Linear-Elastic, Small-Deflection Theory

The development of the necessary equations for the analysis of cylindrical shells begins with the displacement [Equation(I. 12)] and frequency [Equation(I. 13)] equations in Appendix I. We assume that the cylinder's end-closures consist of elastic media which offer unequal, elastic restraint against rotation. For generality, we define these elastic restraints as  $S_1$  at  $x = 0$  and  $S_2$  at  $x = L$  where  $S$  is the stiffness per unit length of the medium or the moment required to rotate a unit length of the medium through an angle of one radian.

The boundary conditions are taken as

$$\left. \begin{aligned} M_{x\phi} \Big|_{x=0} - S_1 \frac{\partial w}{\partial x} \Big|_{x=0} &= 0 \\ M_{x\phi} \Big|_{x=L} - S_2 \frac{\partial w}{\partial x} \Big|_{x=L} &= 0 \\ w \Big|_{x=0} &= 0 \\ w \Big|_{x=L} &= 0 \end{aligned} \right\} \quad (2.1)$$

The first two equations denote the condition of continuity between the shell and the end-closures. The condition that the radial displacements are zero at the shell's boundaries appears reasonable, particularly for end-closures (such as flat plates) which offer a high degree of transverse restraint. Since

$$M_{x\phi} = D \left[ \frac{\partial^2 w}{\partial x^2} - \frac{n^2}{a^2} w \right]$$

Equations (2.1) may be rewritten as follows

$$\left. \begin{aligned} \frac{\partial^2 w}{\partial x^2} \Big|_{x=0} - R_1 \frac{\partial w}{\partial x} \Big|_{x=0} &= 0 \\ \frac{\partial^2 w}{\partial x^2} \Big|_{x=L} - R_2 \frac{\partial w}{\partial x} \Big|_{x=L} &= 0 \\ w \Big|_{x=0} &= 0 \\ w \Big|_{x=L} &= 0 \end{aligned} \right\} \quad (2.2)$$

where

$$R = \frac{SL}{D}$$

Utilizing Equations (2.2) in Equations (I.12) (Appendix I) we obtain the following set of linear, homogeneous equations

$$\left. \begin{aligned} \sum_j C_j &= 0 \\ \sum_j C_j e^{\lambda_j} &= 0 \\ \sum_j \lambda_j^2 C_j - R_1 \sum_j \lambda_j C_j &= 0 \\ \sum_j \lambda_j^2 C_j e^{\lambda_j} - R_2 \sum_j \lambda_j C_j e^{\lambda_j} &= 0 \end{aligned} \right\} (j = 1, 2, 3, 4) \quad (2.3)$$

Since  $\lambda_1 = \kappa$ ,  $\lambda_2 = -\kappa$ ,  $\lambda_3 = i\kappa$ ,  $\lambda_4 = -i\kappa$  (see Appendix I), Equations (2.3) yield the following coefficient determinant which must vanish in order for these equations to be consistent.

$$\begin{vmatrix} 1 & 1 & 1 & 1 \\ e^{\kappa} & e^{-\kappa} & e^{i\kappa} & e^{-i\kappa} \\ \kappa - R_1 & \kappa + R_1 & -(\kappa + iR_1) & -(\kappa - iR_1) \\ (\kappa - R_2)e^{\kappa} & (\kappa + R_2)e^{-\kappa} & -(\kappa + iR_2)e^{i\kappa} & -(\kappa - iR_2)e^{-i\kappa} \end{vmatrix} = 0 \quad (2.4)$$

Expanding the determinant, we have

$$\begin{aligned} \Delta &= 8i[2\kappa^2 \sinh \kappa \sin \kappa + \kappa(R_1 - R_2)(\sinh \kappa \cos \kappa - \cosh \kappa \sin \kappa) \\ &\quad + R_1 R_2(1 - \cosh \kappa \cos \kappa)] = 0 \end{aligned} \quad (2.5)$$

Given the appropriate values of  $R_1$  and  $R_2$ , the corresponding values of  $\kappa$  may be determined, thereby providing the necessary values for  $\alpha_1 = \lambda_1/L = \kappa/L$  for the frequency equation [Equation (I.13)].

The related displacement equations are

$$\begin{aligned} u_{mn}(x, \phi, t) &= \frac{K_3 \kappa C}{\Gamma_1 K_1 L} \cos m\phi \sin \omega_{mn} t \left\{ 2\kappa^2 \left( \sin \kappa \cosh \frac{\kappa x}{L} + \sinh \kappa \cos \frac{\kappa x}{L} \right) \right. \\ &\quad + \kappa R_1 \left[ \Gamma_2 \left( \sinh \frac{\kappa x}{L} + \sin \frac{\kappa x}{L} \right) + \Gamma_4 \left( -\cosh \frac{\kappa x}{L} \right) \right] + 2\kappa R_2 \left( \cos \kappa \cosh \frac{\kappa x}{L} \right. \\ &\quad \left. - \cosh \kappa \cos \frac{\kappa x}{L} \right) - R_1 R_2 \left[ \Gamma_3 \left( \sinh \frac{\kappa x}{L} + \sin \frac{\kappa x}{L} \right) \right. \\ &\quad \left. \left. + \Gamma_2 \left( \cos \frac{\kappa x}{L} - \cosh \frac{\kappa x}{L} \right) \right] \right\} \end{aligned} \quad (2.6)$$

$$\begin{aligned}
v_{mn}(x, \phi, t) = & \frac{K_2 C}{\Gamma_1 K_1} \sin m\phi \sin \omega_{mnt} \left\{ 2\kappa^2 \left( \sin \kappa \sinh \frac{\kappa x}{L} + \sinh \kappa \sin \frac{\kappa x}{L} \right) \right. \\
& + \kappa R_1 \left[ \Gamma_2 \left( \cosh \frac{\kappa x}{L} - \cos \frac{\kappa x}{L} \right) + \Gamma_4 \left( \sin \frac{\kappa x}{L} - \sinh \frac{\kappa x}{L} \right) \right] \\
& + 2\kappa R_2 \left( \cos \kappa \sinh \frac{\kappa x}{L} - \cosh \kappa \sin \frac{\kappa x}{L} \right) - R_1 R_2 \left[ \Gamma_3 \left( \cosh \frac{\kappa x}{L} \right. \right. \\
& \left. \left. - \cos \frac{\kappa x}{L} \right) + \Gamma_2 \left( \sin \frac{\kappa x}{L} - \sinh \frac{\kappa x}{L} \right) \right] \left. \right\} \quad (2.7)
\end{aligned}$$

$$\begin{aligned}
w_{mn}(x, \phi, t) = & \frac{C}{\Gamma_1} \cos m\phi \sin \omega_{mnt} \left\{ 2\kappa^2 \left( \sin \kappa \sinh \frac{\kappa x}{L} + \sinh \kappa \sin \frac{\kappa x}{L} \right) \right. \\
& + \kappa R_1 \left[ \Gamma_2 \left( \cosh \frac{\kappa x}{L} - \cos \frac{\kappa x}{L} \right) + \Gamma_4 \left( \sin \frac{\kappa x}{L} - \sinh \frac{\kappa x}{L} \right) \right] \\
& + 2\kappa R_2 \left( \cos \kappa \sinh \frac{\kappa x}{L} - \cosh \kappa \sin \frac{\kappa x}{L} \right) - R_1 R_2 \left[ \Gamma_3 \left( \cosh \frac{\kappa x}{L} \right. \right. \\
& \left. \left. - \cos \frac{\kappa x}{L} \right) + \Gamma_2 \left( \sin \frac{\kappa x}{L} - \sinh \frac{\kappa x}{L} \right) \right] \left. \right\} \quad (2.8)
\end{aligned}$$

where

$$\begin{aligned}
\Gamma_1 &= 2\kappa^2 \sin \kappa + \kappa R_1 (\sinh \kappa - \cosh \kappa + \sin \kappa - \cos \kappa) + 2\kappa R_2 \cos \kappa \\
&\quad + R_1 R_2 (\sinh \kappa - \cosh \kappa + \sin \kappa + \cos \kappa) \\
\Gamma_2 &= \sin \kappa + \sinh \kappa \\
\Gamma_3 &= \cosh \kappa - \cos \kappa \\
\Gamma_4 &= \cosh \kappa + \cos \kappa
\end{aligned}$$

Having defined the relation for the deflections, it then becomes a simple matter to obtain the accelerations as functions of time.

For the case where the elastic restraints at either end of the cylinder are equal ( $R_1 = R_2 = R$ ), Equation (2.5) reduces to

$$\Delta = 8i[\kappa^2 \sinh \kappa \sin \kappa + R^2(1 - \cosh \kappa \cos \kappa)] = 0 \quad (2.9)$$

and Equation 2.8 becomes:

$$\begin{aligned}
w_{mn}(x, \phi, t) = & \frac{C}{\Gamma_1} \cos m\phi \sin \omega_{mn} t \left\{ 2\kappa^2 \left( \sin \kappa \sinh \frac{\kappa x}{L} + \sinh \kappa \sin \frac{\kappa x}{L} \right) \right. \\
& - \kappa R \left[ \Gamma_2 \left( \cos \frac{\kappa x}{L} - \cosh \frac{\kappa x}{L} \right) + \Gamma_3 \left( \sinh \frac{\kappa x}{L} + \sin \frac{\kappa x}{L} \right) \right] \\
& \left. - R^2 \left[ \Gamma_3 \left( \cosh \frac{\kappa x}{L} - \cos \frac{\kappa x}{L} \right) + \Gamma_2 \left( \sin \frac{\kappa x}{L} - \sinh \frac{\kappa x}{L} \right) \right] \right\}
\end{aligned} \quad (2.10)$$

where

$$\Gamma_1' = 2\kappa \sin \kappa + R(\kappa + R)[\sinh \kappa - \cosh \kappa + \sin \kappa + \cos \kappa]$$

Similar expressions for  $u_{mn}(x, \phi, t)$  and  $v_{mn}(x, \phi, t)$  are found by using the relations

$$\left. \begin{aligned}
u_{mn}(x, \phi, t) &= \frac{K_3}{K_1} \frac{\partial w_{mn}(x, \phi, t)}{\partial x} \\
v_{mn}(x, \phi, t) &= -\frac{K_2}{mK_1} \frac{\partial w_{mn}(x, \phi, t)}{\partial \phi}
\end{aligned} \right\} \quad (2.11)$$

If the cylinder's end-closures are extremely rigid such that the boundary conditions may be assumed fixed, then  $R \rightarrow \infty$  and Equations (2.5) and (2.8) reduce to

$$\Delta = 1 - \cosh \kappa \cos \kappa = 0 \quad (2.12)$$

$$\begin{aligned}
w_{mn}(x, \phi, t) = & \frac{C}{\Gamma_1''} \cos m\phi \sin \omega_{mn} t \left[ \Gamma_3 \left( \cos \frac{\kappa x}{L} - \cosh \frac{\kappa x}{L} \right) \right. \\
& \left. + \Gamma_2 \left( \sinh \frac{\kappa x}{L} - \sin \frac{\kappa x}{L} \right) \right]
\end{aligned} \quad (2.13)$$

where

$$\Gamma_1'' = \sinh \kappa - \cosh \kappa + \sin \kappa + \cos \kappa$$

For the condition where the cylinder's end-closures are such that the boundaries are simply supported, then  $R = 0$  and Equations (2.5) and (2.8) become

$$\Delta = \sinh \kappa \sin \kappa = 0 \quad (2.14)$$

$$w_{mn}(x, \phi, t) = C_4 \cos m\phi \sin \omega_{mn} t \sin \frac{\kappa x}{L} \quad [\text{Ref. Eq. (2.3)}] \quad (2.15)$$

Equations (2.12) and (2.14) provide the extreme values of  $\kappa$ . That is, for the cylindrical shell with both edges fixed, Equation (2.12) gives

$$\kappa = \frac{1}{2} [2n + 1] \pi = n'\pi \quad (n = 1, 2, 3, \dots) \quad (2.16)$$

whereas for the simply supported boundaries, Equation (2.14) gives

$$\kappa = n\pi \quad (n = 1, 2, 3, \dots) \quad (2.17)$$

Similarly, from Equation (2.9), we obtain the variation of  $\kappa$  with the term representing the end-closures' stiffnesses. This is shown in Figure 2.1.

### 2.1.2 Linear-Elastic, Large Deflection Theory\*

In order to avoid the prohibitive difficulties associated with a detailed analysis and thereby obtain a solution that will lead to useful information, we assume that:

- (a) The elements normal to the middle surface remain normal and unstretched (extensional or membrane vibrations)
- (b) The cylinder wall is thin (say  $\frac{h}{a} < \frac{1}{30}$ )
- (c) The longitudinal (u) and tangential (v) displacement components are small compared to the radial displacement (w).

For the equations of motion, we have

$$\left. \begin{aligned} \frac{\partial N_{xx}}{\partial x} + \frac{\partial N_{xy}}{\partial y} &= \rho h \ddot{u} \\ \frac{\partial N_{xy}}{\partial x} + \frac{\partial N_{yy}}{\partial y} &= \rho h \ddot{v} \end{aligned} \right\} \quad (2.18)$$

Following the format of Fung and Sechler<sup>(2.1)</sup>, we define the strain components at the shell's middle surface as

$$\left. \begin{aligned} \epsilon_x &= \frac{\partial u}{\partial x} + \frac{1}{2} \left( \frac{\partial w}{\partial x} \right)^2 \\ \epsilon_y &= \frac{\partial v}{\partial y} + \frac{1}{2} \left( \frac{\partial w}{\partial y} \right)^2 - \frac{w}{a} \\ \gamma_{xy} &= \frac{\partial u}{\partial y} + \frac{\partial v}{\partial x} + \frac{\partial w}{\partial x} \frac{\partial w}{\partial y} \end{aligned} \right\} \quad (2.19)$$

By neglecting the inertia terms in the x and y directions (this corresponds to a first order approximation in the perturbation procedure) and introducing the stress function  $F(x, y)$  where Equations (2.17) are satisfied by

$$\frac{\partial^2 F}{\partial y^2} = N_{xx}, \quad \frac{\partial^2 F}{\partial x^2} = N_{yy}, \quad - \frac{\partial^2 F}{\partial x \partial y} = N_{xy}$$

\*Notation in this section same as that given in Appendix I except where noted.

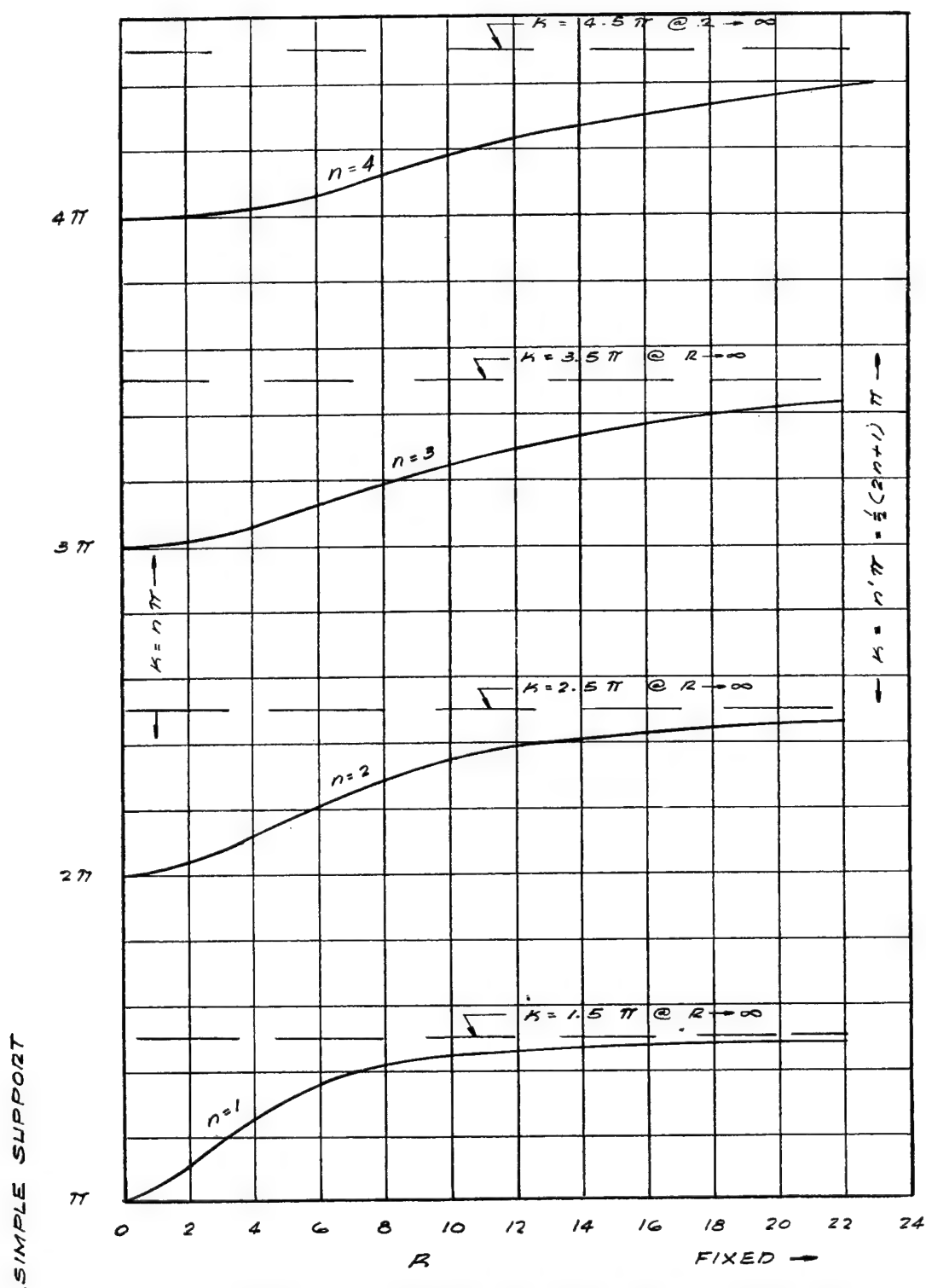


FIGURE 2.1. VARIATION OF FREQUENCY PARAMETER  
WITH STIFFNESS PARAMETER  
(See Eq. 2.9)

we obtain the compatibility equation

$$\nabla^4 F = Eh \left[ \left( \frac{\partial^2 w}{\partial x \partial y} \right)^2 - \frac{\partial^2 w}{\partial x^2} \frac{\partial^2 w}{\partial y^2} - \frac{1}{a} \frac{\partial^2 w}{\partial x^2} \right] \quad (2.20)$$

and the equation of motion for the radial displacement

$$\begin{aligned} \nabla^4 w = \frac{1}{D} \left[ \frac{\partial^2 w}{\partial x^2} \frac{\partial^2 F}{\partial y^2} - 2 \frac{\partial^2 w}{\partial x \partial y} \frac{\partial^2 F}{\partial x \partial y} + \frac{\partial^2 w}{\partial y^2} \frac{\partial^2 F}{\partial x^2} \right. \\ \left. + \frac{1}{a} \frac{\partial^2 F}{\partial x^2} + p(x, \phi, t) - \rho \ddot{w} \right] \end{aligned} \quad (2.21)$$

The problem now becomes one of assuming a form for the radial displacement, using it to determine the stress function from Equation (2.20) which, in turn, is applied to Equation (2.21). The latter equation suggests that the radial displacement may be of the form

$$w(x, y, t) = f(t) \cdot G(x, y)$$

where  $G(x, y)$  denotes the mode shape.

The most appropriate expression is one which is sufficiently complete so as to embrace all the significant parameters but not unduly complex so as to complicate the analysis and introduce refinements that are not commensurate with the required accuracy of the final numerical answers.

As an example of a simple mode shape, we take

$$w(x, y, t) = f(t) [\sin ax \cos \beta y + \psi \sin ax \cos \gamma y] \quad (2.22)$$

where  $a = \pi/L$ ,  $\beta = 1/a$ ,  $\gamma = m/a$ , and  $m$  denotes the number of circumferential half waves. Using Equation (2.22) in Equation (2.20) and after extensive algebraic manipulation, we arrive at the following expression for the stress function

$$\begin{aligned} F = \frac{Eh [f(t)]^2 a^2}{4} [K_1 \cos 2\beta y + K_2 \cos 2\gamma y + K_3 \cos (\beta - \gamma)y + K_4 \cos (\beta + \gamma)y \\ + K_5 \cos 2ax + K_6 \cos (\beta - \gamma)y \cos 2ax + K_7 \cos (\beta + \gamma)y \cos 2ax \\ + K_8 \sin ax \cos \beta y + K_9 \sin ax \cos \gamma y] \end{aligned} \quad (2.23)$$

where

$$\begin{aligned} K_1 &= -\frac{1}{8\beta^2} & K_4 &= -\frac{\psi}{(\beta + \gamma)^2} & K_7 &= \frac{\psi(\beta - \gamma)^2}{[4a^2 + (\beta + \gamma)^2]^2} \\ K_2 &= -\frac{\psi^2}{8\gamma^2} & K_5 &= \frac{\beta^2 + \psi^2\gamma^2}{8a^4} & K_8 &= \frac{4}{f(t)a(a^2 + \beta^2)^2} \\ K_3 &= -\frac{\psi^2}{(\beta - \gamma)^2} & K_6 &= \frac{\psi(\beta + a)^2}{[4a^2 + (\beta - \gamma)^2]^2} & K_9 &= \frac{4\psi}{f(t)a(a^2 + \gamma^2)^2} \end{aligned}$$

For a radial displacement equation of the form

$$w(x, y, t) = f(t)[\sin ax \cos \beta y + \sin ax \cos \gamma y + \Phi \sin ax] \quad (2.24)$$

the stress function is as follows

$$\begin{aligned} F = & \frac{Eh[f(t)]^2 a^2}{4} [K_1 \cos 2\beta y + K_2 \cos 2\gamma y + K_3 \cos (\beta - \gamma)y + K_4 \cos (\beta + \gamma)y \\ & + K_5 \cos 2\gamma x + K_6 \cos (\beta - \gamma)y \cos 2ax + K_7 \cos (\beta + \gamma)y \cos 2ax \\ & + K_8 \cos 2ax \cos \beta y + K_9 \cos 2ax \cos \gamma y + K_{10} \cos \beta y + K_{11} \cos \gamma y \\ & + K_{12} \sin ax \cos \beta y + K_{13} \sin ax \cos \gamma y + K_{14} \sin ax] \end{aligned} \quad (2.25)$$

where  $K_1$  through  $K_7$ ,  $K_{12}$  and  $K_{13}$  are the same as those given for Equation (2.23) (except that  $\psi = 1$ ) and

$$\begin{aligned} K_8 &= \frac{2\Phi\beta^2}{(4a^2 + \beta^2)^2} & K_{10} &= \frac{2\Phi}{\beta^2} \\ K_9 &= \frac{2\Phi\gamma^2}{(4a^2 + \beta^2)^2} & K_{11} &= \frac{2\Phi}{\gamma^2} \end{aligned}$$

As a final example, for

$$w(x, \phi, t) = f(t)[\Lambda \sin ax \cos \beta y + \sin ax \cos \gamma y + \chi \sin^2 ax] \quad (2.26)$$

the stress function becomes

$$\begin{aligned} F = & \frac{Eh[f(t)]^2 a^2}{4} [K_1 \cos 2\beta y + K_2 \cos 2\gamma y + K_3 \cos (\beta - \gamma)y + K_4 \cos (\beta + \gamma)y \\ & + K_5 \cos 2ax + K_6 \cos (\beta - \gamma)y \cos 2ax + K_7 \cos (\beta + \gamma)y \cos 2ax \\ & + K_8 \sin ax \cos \beta y + K_9 \sin ax \cos \gamma y + K_{10} \sin 3ax \cos \beta y \\ & + K_{11} \sin 3ax \cos \gamma y] \end{aligned} \quad (2.27)$$

where  $K_1$  through  $K_4$ ,  $K_6$ , and  $K_7$  are identical to those for Equation (2.23) (for  $\psi = 1$ ) and

$$K_5 = \frac{\gamma^2 + (\beta\Lambda)^2 - \frac{4\chi}{af(t)}}{8a^4}$$

$$K_8 = \frac{[1 - a\gamma^2\chi f(t)]^4}{f(t)a(a^2 + \gamma^2)^2}$$

$$K_9 = \frac{[1 - a\beta^2\chi f(t)] 4\psi}{f(t)(a^2 + \beta^2)^2}$$

$$K_{10} = \frac{\chi\gamma^2}{(9a^2 + \gamma^2)^2}$$

$$K_{11} = \frac{\chi\beta^2\psi}{(9a^2 + \beta^2)^2}$$

The Galerkin procedure may now be used to find the differential equation for the time function  $f(t)$ , thereby providing not only the deflection, but also the acceleration as a function of time. The Galerkin equation will have the form

$$\int_0^L \int_0^{2\pi a} \left\{ D\nabla^4 w - \left[ \frac{\partial^2 w}{\partial x^2} \frac{\partial^2 F}{\partial y^2} - 2 \frac{\partial^2 w}{\partial x \partial y} \frac{\partial^2 F}{\partial x \partial y} + \frac{\partial^2 w}{\partial y^2} \frac{\partial^2 F}{\partial x^2} + \frac{1}{a} \frac{\partial^2 F}{\partial x^2} \right. \right. \\ \left. \left. + p(x, \phi, t) - \rho \ddot{w} \right] w(x, \phi, t) \right\} dx dy = 0 \quad (2.28)$$

where, for example, the stress functions (F) derived from the radial displacement expression  $w(x, \phi, t)$  would be those from Equations (2.22) and (2.23), (2.24) and (2.25), or (2.26) and (2.27).

In order to obtain a solution for Equation (2.28), it is first necessary to specify the external loading conditions,  $p(x, \phi, t)$ . One satisfactory relation is the following

$$p(x, \phi, t) = \left( p_0 + p_1 \cos \frac{y}{a} \right) \tau(t) \quad (2.29)$$

where, for example,

$$\tau(t) = e^{-\delta t}$$

or

$$\tau(t) = ct$$

The differential equation for the time function is of the form

$$\ddot{J} + A_1 J^3 + A_2 J^2 + A_3 J = A_4 \tau(t) \quad (2.30)$$

where  $J = f(t)/a$  and  $A_1, \dots, A_4$  are coefficients reflecting the particular characteristics of the mode shape and load function. As a particular example, we take  $L = 36$  inches,  $A = 6$  inches,  $h = .036$  inch,  $E = 2.9 \times 10^6$  psi,  $\nu = 0.25$  and  $\rho = 24.7 \times 10^{-6}$  lb-sec<sup>2</sup>/in<sup>3</sup> as the properties of the cylindrical shell. For the mode shape defined in Equation (2.26) (with  $\chi = 0$ ,  $\Lambda = 1.0$  or 0, and  $n = 2$ ) and the loading defined as

$$p(x, \phi, t) = p_0 (1 + B \cos \beta y) e^{-\delta t}$$

the numerical values of the coefficients are as follows:

For  $\Lambda = 1$ :  $p_0 = 70$  psi,  $B = 4/7$  and  $\delta = 2.77 \times 10^{-2}$

$$A_1 = 23.4, A_2 = -14.3, A_3 = 5.8, A_4 = 3.72 \times 10^{-3}$$

For  $\Lambda = 0$ :  $p_0 = 70$  psi,  $B = 4/7$ , and  $\delta = 2.77 \times 10^{-2}$

$$A_1 = 10.4, A_2 = -1.1, A_3 = 0.3, A_4 = 1.65 \times 10^{-3}$$

The variation of  $J$  as a function of  $\tau(t)$  is given in Figure 2.2. Accordingly, the maximum radial displacements for  $\Lambda = 1$  and  $\Lambda = 0$  are respectively

$$w_{\max} = 0.022''$$

$$w_{\max} = 0.11''$$

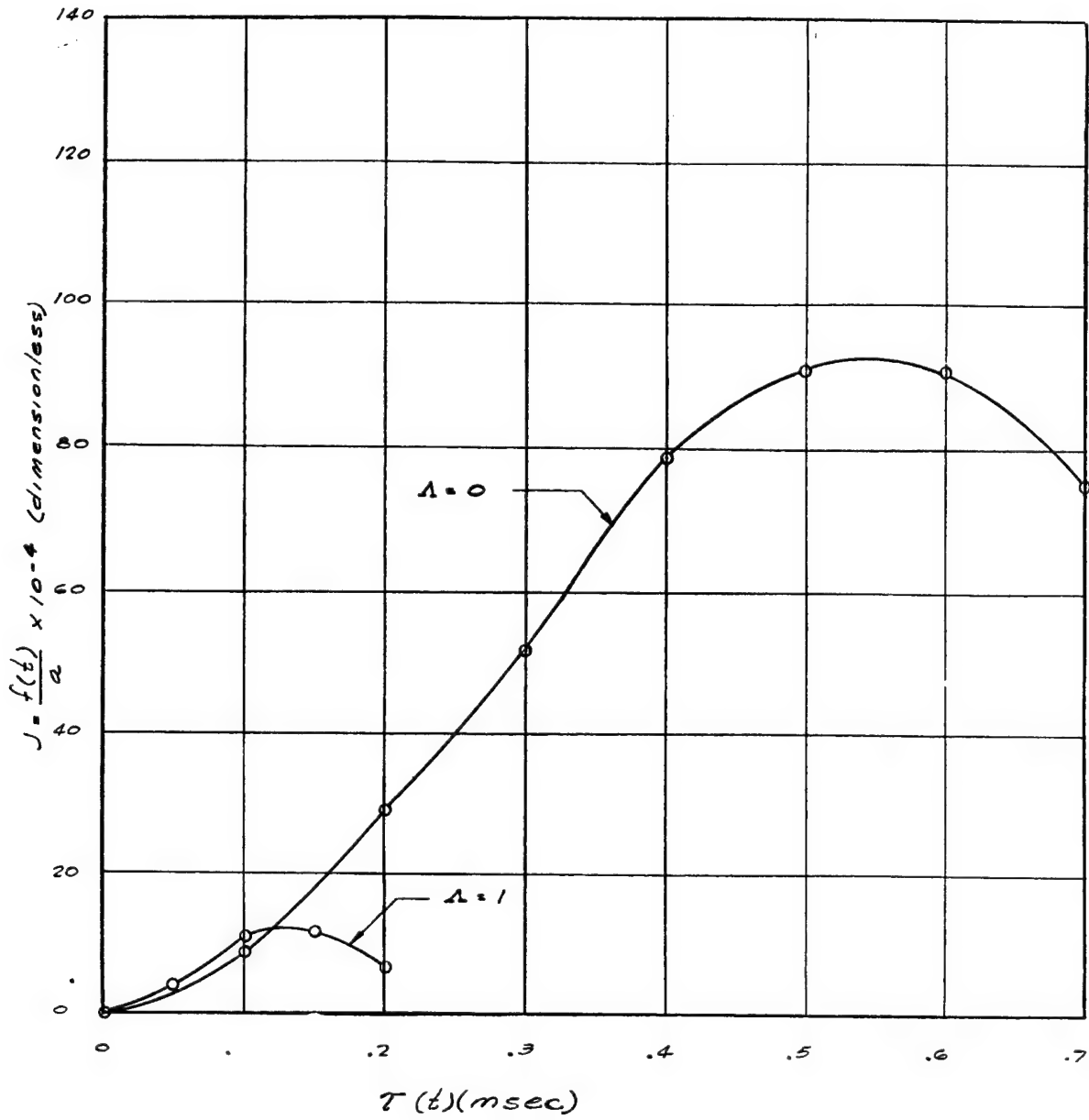


FIGURE 2.2. VARIATION OF TIME FUNCTION WITH  $\tau(t)$   
(See Eq. 2.30)

## 2.2 Dynamic Response of Circular Plates

### 2.2.1 Large Amplitudes

#### LIST OF SYMBOLS

a	radius of circular plate (in.)
D	$= \frac{Eh^3}{12(1-\nu^2)}$ , flexural rigidity of plate (lb in.)
E	modulus of elasticity of plate (lb/in <sup>2</sup> )
f, F, G	functions of time
h	thickness of plate (in.)
J <sub>n</sub> , I <sub>n</sub> , Y <sub>n</sub> , K <sub>n</sub>	Bessel functions of order n
N	$= (N_r + N_t)/(1 + \nu)$ (lb in <sup>-1</sup> )
N*	buckling load of circular plate (lb in <sup>-1</sup> )
N <sub>r</sub> , N <sub>t</sub>	stress resultants in the radial and tangential directions, respectively (lb in <sup>-1</sup> )
p	natural frequency of plate (sec <sup>-1</sup> )
r, $\theta$	cylindrical coordinates
$\bar{r}$	$= \frac{r}{a}$
t	time (sec)
$\bar{t}$	$= \frac{th}{a^2} \sqrt{\frac{E}{12(1-\nu^2)\rho^*}}$
v	velocity (in. sec <sup>-1</sup> )
$\bar{v}$	$= v \frac{a^2}{h^2} \sqrt{\frac{12(1-\nu^2)\rho^*}{E}}$
w	lateral deflection of plate (in.)
$\bar{w}$	$= \frac{w}{h}$
$\rho$	mass per unit area of plate (lb sec <sup>2</sup> in <sup>-3</sup> )
$\rho^*$	mass density of plate material (lb sec <sup>2</sup> in <sup>-4</sup> )
$\nabla^4$	$= (\nabla^2)^2 = \text{biharmonic operator} = \left( \frac{\partial^2}{\partial r^2} + \frac{1}{r} \frac{\partial}{\partial r} + \frac{1}{r^2} \frac{\partial^2}{\partial \theta^2} \right)^2$

It is well known that when the lateral deflections are large the behavior of plates is governed by two coupled nonlinear partial differential equations usually credited to von Kármán. (2.2) The dynamic analogue of these equations has been derived by G. Hermann. (2.3) Chu and Hermann (2.4) have calculated the fundamental frequencies of rectangular plates at large amplitudes by an energy procedure.

However, a theoretically exact solution of the dynamical equations even for the case of free vibrations is nonexistent. The case of forced vibrations had apparently not been studied at all. It is to be realized that, owing to the nonlinearity of the equations, the free and forced vibration problems cannot be solved separately and superposed, neither can advantage be taken of the concept of normal modes as is usual in the linear case.

In 1955, Berger<sup>(2.5)</sup> proposed a set of equations which may be termed a simplified version of the von Kármán system. The merit of his method lies in decoupling the two equations, so that one of them assumes a quasi-linear form and can readily be integrated. He showed further that his equations yielded solutions remarkably close to those obtained by more elaborate procedures using von Kármán's equations, at least as regards deflections. Berger, it must be remarked, confined himself to the static case.

Nash and Modeer<sup>(2.6)</sup> extended the Berger equations to the dynamic case for rectangular plates and showed that the free vibration problem can be treated to yield results which are reasonably close to the results obtained by Chu and Hermann. (2.4)

In what follows, the dynamical equations à la Berger are extended to circular plates. By using an approximate step-by-step procedure, it is shown that not only the free vibration but also the forced vibration problem may be solved using the elementary concept of normal modes. It is necessary to add that although the basic Berger formulation has a quasi-linear form for the static case, it is nonlinear for the dynamic case and cannot be solved with comparable ease.

#### 2.2.1.1 Equations of Motion

For the dynamical case, the Berger equations for circular plates may be written in the form

$$\left. \begin{aligned} \nabla^4 w - \alpha^2 \nabla^2 w + \frac{\rho}{D} \frac{\partial^2 w}{\partial t^2} &= \frac{f(r, \theta, t)}{D} \\ \frac{\alpha^2 h^2}{12} &= \frac{\partial u}{\partial r} + \frac{1}{2} \left( \frac{\partial w}{\partial r} \right)^2 + \frac{u}{r} + \frac{1}{r} \frac{\partial v}{\partial \theta} + \frac{1}{2r^2} \left( \frac{\partial w}{\partial \theta} \right)^2 = \epsilon_r + \epsilon_t \end{aligned} \right\} \quad (2.31)$$

in which  $\nabla^4 = (\nabla^2)^2$  is the biharmonic operator,  $\rho$  is the mass of the plate per unit of area,  $w$  is the lateral deflection,  $u$  and  $v$  the radial and tangential displacements,  $D = \frac{Eh^3}{12(1-\nu^2)}$  is the flexural rigidity of the plate,  $h$  its thickness,  $E$  is the elastic modulus,  $\nu$  is Poisson's ratio and  $f$  a given forcing function.

The radial and tangential strains  $\epsilon_r$  and  $\epsilon_t$  may be expressed in terms of the stress resultants  $N_r$  and  $N_t$  as follows

$$\left. \begin{aligned} \epsilon_r &= \frac{1}{hE} (N_r - \nu N_t) \\ \epsilon_t &= \frac{1}{hE} (N_t - \nu N_r) \end{aligned} \right\} \quad (2.32)$$

It follows from (2.32) and the second of (2.31) that

$$\frac{\alpha^2 h^2}{12} = \frac{1-\nu}{hE} (N_r + N_t) = \frac{Nh^2}{12D} \quad (2.33)$$

In the Berger formulation,  $\alpha$  is constant throughout the plate and thus  $N$ , which has the same dimension as a stress resultant, is also constant throughout the plate. [The simplicity of the Berger equations apparently derives from the basic assumption that  $(N_r + N_t)$  is constant.]

From Equations (2.33) and the second of (2.31) one finds

$$\frac{Nh^2}{12D} = \frac{\partial u}{\partial r} + \frac{1}{2} \left( \frac{\partial w}{\partial r} \right)^2 + \frac{u}{r} + \frac{1}{r} \frac{\partial v}{\partial \theta} + \frac{1}{2r^2} \left( \frac{\partial w}{\partial \theta} \right)^2$$

In view of the assumed constancy of  $N$  with respect to  $r$  and  $\theta$ , one may multiply by  $r dr d\theta$  and integrate over the plate to find

$$\begin{aligned} \frac{N}{D} \iint \frac{h^2}{12} r dr d\theta &= \iint \left( \frac{\partial u}{\partial r} + \frac{u}{r} \right) r dr d\theta + \iint \frac{1}{r} \frac{\partial v}{\partial \theta} r dr d\theta + \\ &+ \frac{1}{2} \iint \left[ \left( \frac{\partial w}{\partial r} \right)^2 + \frac{1}{r^2} \left( \frac{\partial w}{\partial \theta} \right)^2 \right] r dr d\theta \end{aligned}$$

If the boundary conditions are such that  $u$  and  $v$  vanish at the boundaries, the first two integrals on the right-hand side are evanescent and there must follow

$$\left. \begin{aligned} \frac{Nh^2 \pi a^2}{12D} &= \frac{1}{2} \int_0^{2\pi} \int_0^a \left( \frac{\partial w}{\partial r} \right)^2 + \frac{1}{r^2} \left( \frac{\partial w}{\partial \theta} \right)^2 r dr d\theta \\ \nabla^4 w - \frac{N}{D} \nabla^2 w + \frac{\rho}{D} \frac{\partial^2 w}{\partial t^2} &= \frac{f(r, \theta, t)}{D} \end{aligned} \right\} \quad (2.34)$$

using (2.33) the first of (2.31) may be written

The problem now reduces to the integration of the system (2.34).

#### 2.2.1.2 Integration Procedure

It is seen from the first of (2.34) that  $N$  is a function of time alone and that the second of (2.34) is effectively nonlinear. The problem of finding the dynamic response of such a system cannot be solved by superposition of the separate solutions of free vibrations and of the steady state problem.

A step-by-step integration procedure is here proposed for the integration of the system (2.34). The assumption is made that  $N$ , which is proportional to the sum of the membrane tensions ( $N_r + N_t$ ), remains constant at  $\bar{N}$  for a sufficiently short interval of time  $\Delta$ . It is evident that the second of (2.34) assumes a linear form and may be readily integrated.  $\bar{N}$  is evaluated from the first of (2.34) at the beginning of each time interval. The nonlinear problem is thus reduced to a series of linear problems in time.

Even this simplification, it may be noted, still involves a prodigious amount of labor. For, since the normal modes of vibration are a function  $\bar{N}$ , they are a function of time also. Furthermore, the forcing function  $f(r, \theta, t)$  has to be expanded in a series of the normal modes appropriate to that time interval.

Thus, the general procedure is as follows: Starting with the given initial conditions, evaluate  $\bar{N}$  from the first of (2.34). Use this value of  $\bar{N}$  to solve the homogeneous part of the second of (2.34) and determine the natural frequencies. Expand the forcing function in terms of the normal modes and determine a particular solution of the second of (2.34). Use the initial conditions at time zero to determine the deflection and velocity at the end of the time interval  $\Delta$ . Use the latter as the initial condition for the second time interval  $\Delta$ . Repeat this procedure up to any desired time  $t = s\Delta$ .

(Some of the tediousness of this procedure may be reduced if one ignores the change in the normal functions at each time interval, using throughout instead the functions appropriate to the initial interval, but taking account of the change in the natural frequencies at each interval.)

Returning now to the second of (2.34), let

$$w = R(r)\Theta(\theta) \sin pt \quad (2.35)$$

where  $R$  is a function of  $r$  alone and  $\Theta$  is a function of  $\theta$  alone. On substitution into the homogeneous part of the second of (2.34) and dividing out the common factor  $\sin pt$  there follows

$$\nabla^4(R\Theta) - \frac{\bar{N}}{D} \nabla^2(R\Theta) - \frac{p^2 \rho}{D} R\Theta = 0$$

which may be written in the form

$$\left( \nabla^2 + \frac{\alpha^2}{a^2} \right) \left( \nabla^2 - \frac{\beta^2}{a^2} \right) (R\Theta) = 0 \quad (2.36)$$

where

$$\left. \begin{aligned} \alpha^2 &= \frac{\bar{N}a^2}{2D} \left[ \left( 1 + \frac{4p^2 \rho D}{\bar{N}^2} \right)^{1/2} - 1 \right] \\ \beta^2 &= \frac{\bar{N}a^2}{2D} \left[ \left( 1 + \frac{4p^2 \rho D}{\bar{N}^2} \right)^{1/2} + 1 \right] \end{aligned} \right\} \quad (2.37)$$

$$\beta^2 - \alpha^2 = \frac{\bar{N}a^2}{D} \quad (2.38)$$

$$p = \sqrt{\frac{D}{\rho} \frac{\alpha\beta}{a^2}} \quad (2.39)$$

Equation (2.36) shows that the complete solution may be obtained by adding together, with appropriate arbitrary constants, the solutions of the two equations

$$\left. \begin{aligned} \left( \nabla^2 + \frac{\alpha^2}{a^2} \right) R\Theta &= 0 \\ \left( \nabla^2 - \frac{\beta^2}{a^2} \right) R\Theta &= 0 \end{aligned} \right\} \quad (2.40)$$

On letting

$$\Theta = \cos(n\theta - \gamma_n) \quad (2.41)$$

Equations (2.40) yield two ordinary differential equations for the determination of  $R$

$$\left. \begin{aligned} \frac{d^2 R}{dr^2} + \frac{1}{r} \frac{dR}{dr} + \left( \frac{\alpha^2}{a^2} - \frac{n^2}{r^2} \right) R &= 0 \\ \frac{d^2 R}{dr^2} + \frac{1}{r} \frac{dR}{dr} - \left( \frac{\beta^2}{a^2} + \frac{n^2}{r^2} \right) R &= 0 \end{aligned} \right\} \quad (2.42)$$

The solutions of (2.42) are, respectively

$$R = A J_n \left( \frac{\alpha r}{a} \right) + C Y_n \left( \frac{\alpha r}{a} \right)$$

and

$$R = BI_n \left( \frac{\beta r}{a} \right) + DK_n \left( \frac{\beta r}{a} \right)$$

in which  $J_n$  and  $Y_n$  denote Bessel functions of the order  $n$  of the first and second kinds, respectively.  $I_n$  and  $K_n$  are the modified Bessel functions of the first and second kinds, and  $A$ ,  $B$ ,  $C$ , and  $D$  are arbitrary constants. (The notation for the Bessel functions is that used in Reference 2.7.)

In the case of a solid plate,  $Y_n$  and  $K_n$  are inadmissible because of the singularity at  $r = 0$ , and the general solution of the system (2.42) is thus

$$R = A_n J_n \left( \frac{ar}{a} \right) + B_n I_n \left( \frac{\beta r}{a} \right) \quad (2.43)$$

The general solution of the homogeneous part of the second of (2.34) may now be written

$$w = \left\{ A_n J_n \left( \frac{ar}{a} \right) + B_n I_n \left( \frac{\beta r}{a} \right) \right\} \left\{ \cos n\theta + C_n \sin n\theta \right\} \left\{ \sin p_n t + D_n \cos p_n t \right\} \quad (2.44)$$

The frequency equation and the ratio  $B_n/A_n$  may be obtained from the boundary conditions.

In the case of a simply supported plate, one has

$$\left. \begin{aligned} w &= 0 \\ \frac{\partial^2 w}{\partial r^2} + \nu \left( \frac{1}{r} \frac{\partial w}{\partial r} + \frac{1}{r^2} \frac{\partial^2 w}{\partial \theta^2} \right) &= 0 \end{aligned} \right\} \text{ at } r = a \quad (2.45)$$

and in the case of a clamped plate

$$\left. \begin{aligned} w &= 0 \\ \frac{\partial w}{\partial r} &= 0 \end{aligned} \right\} \text{ at } r = a \quad (2.46)$$

Substitution of (2.44) into (2.45) yields

$$\left. \begin{aligned} \frac{B_n}{A_n} &= - \frac{J_n(a)}{I_n(\beta)} \\ a \frac{J_{n+1}(a)}{J_n(a)} + \beta \frac{I_{n+1}(\beta)}{I_n(\beta)} &= \frac{\beta^2 + a^2}{1 - \nu} \end{aligned} \right\} \quad (2.47)$$

and the substitution of (2.44) into (2.46) leads to

$$\left. \begin{aligned} \frac{B_n}{A_n} &= \frac{J_n(a)}{I_n(\beta)} \\ a \frac{J_{n+1}(a)}{J_n(a)} + \beta \frac{I_{n+1}(\beta)}{I_n(\beta)} &= 0 \end{aligned} \right\} \quad (2.48)$$

The second of (2.47) is the frequency equation for the simply supported plate and the second of (2.48) for the clamped plate. These equations, together with (2.38), are sufficient for the determination of the natural frequencies  $p_n$  for given values of  $N$ .

Defining

$$\left. \begin{aligned} \frac{\bar{N}}{N^*} &= \phi \\ N^* &= \frac{4.2D}{a^2} \text{ with } \nu = 0.3, \text{ for a simply supported plate} \\ &= \frac{14.68D}{a^2} \text{ for a clamped plate} \end{aligned} \right\} \quad (2.49)$$

the frequency equation for the simply supported plate may be written

$$\left. \begin{aligned} a \frac{J_{n+1}(a)}{J_n(a)} + \beta \frac{I_{n+1}(\beta)}{I_n(\beta)} &= \frac{\beta^2 + a^2}{1 - \nu} \\ \beta^2 - a^2 &= 4.2\phi \\ \nu &= 0.3 \end{aligned} \right\} \quad (2.50)$$

and that for the clamped plate

$$\left. \begin{aligned} a \frac{J_{n+1}(a)}{J_n(a)} + \beta \frac{I_{n+1}(\beta)}{I_n(\beta)} &= 0 \\ \beta^2 - a^2 &= 14.68\phi \end{aligned} \right\} \quad (2.51)$$

Equations (2.50) and (2.51) may be solved for various values of the parameter  $\phi$  and the values of  $a$  and  $\beta$  so derived may be tabulated or graphed as functions of  $\phi$ .

It will be noted from (2.45) and (2.46) that the ratio  $\frac{B_{nj}}{A_{nj}} = \frac{J_n(a_j)}{I_n(\beta_j)}$  whether the plate is simply supported or clamped.

Letting

$$J_n\left(\frac{a_j r}{a}\right) - \frac{J_n(a_j)}{I_n(\beta_j)} I_n\left(\frac{\beta_j r}{a}\right) = R_{nj} \quad (2.52)$$

one may write the deflection function (2.44), corresponding to the  $(nj)^{\text{th}}$  frequency as follows

$$w_{nj} = R_{nj} \left\{ A_{nj} \cos n\theta + B_{nj} \sin n\theta \right\} \left\{ \sin p_{nj}t + D_{nj} \cos p_{nj}t \right\} \quad (2.53)$$

in which  $A_{nj}$ ,  $B_{nj}$  and  $D_{nj}$  are new arbitrary constants, to be determined from the initial conditions. It may be seen that (2.53) may be written in the form

$$w_{nj} = R_{nj} \left\{ A_{nj}(t) \cos n\theta + B_{nj}(t) \sin n\theta \right\} \quad (2.54)$$

where

$$\left. \begin{aligned} A_{nj}(t) &\equiv A_{nj} \left\{ \sin p_{nj}t + D_{nj} \cos p_{nj}t \right\} \\ B_{nj}(t) &\equiv B_{nj} \left\{ \sin p_{nj}t + D_{nj} \cos p_{nj}t \right\} \end{aligned} \right\} \quad (2.55)$$

Any arbitrary deflection satisfying the boundary conditions, and therefore the solution of the homogeneous part of the first of (2.34) appears finally in the form

$$w^c = \sum_{n=0}^{\infty} \sum_{j=1}^{\infty} R_{nj} A_{nj}(t) \cos n\theta + \sum_{n=1}^{\infty} \sum_{j=1}^{\infty} R_{nj} B_{nj}(t) \sin n \quad (2.56)$$

where the superscript "c" on the left denotes "complementary function."

### 2.2.1.3 Forced Vibration

In seeking a particular solution of the first of (2.34), it will be supposed that the forcing function  $f(r, \theta, t)$  can be expanded in terms of the principal modes in the form

$$f(r, \theta, t) = F(t) \sum_n \sum_j R_{nj} (r_{nj} \cos n\theta + s_{nj} \sin n\theta) \quad (2.57)$$

A particular solution of (2.34) is sought in the form

$$w^P = \sum_n \sum_j R_{nj} \left\{ a_{nj}(t) \cos n\theta + b_{nj}(t) \sin n\theta \right\} \quad (2.58)$$

in which  $a_{nj}$  and  $b_{nj}$  are undetermined time functions.

Inasmuch as  $R_{nj} \cos n\theta$  and  $R_{nj} \sin n\theta$  satisfy the homogeneous part of the first of (2.34) there must follow

$$\nabla^4 \begin{pmatrix} R_{nj} \cos n\theta \\ R_{nj} \sin n\theta \end{pmatrix} - \frac{N}{D} \nabla^2 \begin{pmatrix} R_{nj} \cos n\theta \\ R_{nj} \sin n\theta \end{pmatrix} = \frac{P_{nj}^2}{D} \begin{pmatrix} R_{nj} \cos n\theta \\ R_{nj} \sin n\theta \end{pmatrix} \quad (2.59)$$

Substituting (2.58) into the first of (2.34) and making use of (2.59) one finds

$$\left. \begin{aligned} \ddot{a}_{nj} + P_{nj}^2 a_{nj} &= \frac{F(t) f_{nj}}{\rho} \\ \ddot{b}_{nj} + P_{nj}^2 b_{nj} &= \frac{F(t) s_{nj}}{\rho} \end{aligned} \right\} \quad (2.60)$$

Let the particular solutions of these equations be

$$\left. \begin{aligned} a_{nj} &= g_{nj} G(t) \\ b_{nj} &= h_{nj} G(t) \end{aligned} \right\} \quad (2.61)$$

From (2.58) and (2.61), one gets

$$w^P = \sum_n \sum_j R_{nj} (g_{nj} \cos n\theta + h_{nj} \sin n\theta) G(t) \quad (2.62)$$

The complete solution of the first of (2.34) may now be obtained by adding (2.56) and (2.62)

$$w = w^C + w^P = \sum_{n=0}^{\infty} \sum_{j=1}^{\infty} R_{nj} [A_{nj}(t) + g_{nj} G(t)] \cos n\theta + \sum_{n=1}^{\infty} \sum_{j=1}^{\infty} R_{nj} [B_{nj}(t) + h_{nj} G(t)] \sin n\theta \quad (2.63)$$

Let the initial conditions be

$$\left. \begin{aligned} w &= \phi(r) \psi(\theta) \\ \dot{w} &= \chi(r) \mu(\theta) \end{aligned} \right\} \text{ at } t = 0$$

These can always be expanded in Fourier-Bessel series of the form

$$\left. \begin{aligned} w &= \sum_{j=1}^{\infty} \sum_{n=0}^{\infty} R_{nj} H_{nj} \cos n\theta + \sum_{j=1}^{\infty} \sum_{n=1}^{\infty} R_{nj} L_{nj} \sin n\theta \\ \dot{w} &= \sum_{j=1}^{\infty} \sum_{n=0}^{\infty} R_{nj} M_{nj} \cos n\theta + \sum_{j=1}^{\infty} \sum_{n=0}^{\infty} R_{nj} N_{nj} \sin n\theta \end{aligned} \right\} \quad (2.64)$$

where

$$\left. \begin{aligned} \lambda H_{nj} &= \int_0^{2\pi} \int_0^a \phi(r) \psi(\theta) R_{nj} \cos n\theta r dr d\theta \\ \lambda L_{nj} &= \int_0^{2\pi} \int_0^a \phi(r) \psi(\theta) R_{nj} \sin n\theta r dr d\theta \quad n \neq 0 \\ \lambda M_{nj} &= \int_0^{2\pi} \int_0^a \chi(r) \mu(\theta) R_{nj} \cos n\theta r dr d\theta \\ \lambda N_{nj} &= \int_0^{2\pi} \int_0^a \chi(r) \mu(\theta) R_{nj} \sin n\theta r dr d\theta \quad n \neq 0 \end{aligned} \right\} \quad (2.65)$$

in which

$$\begin{aligned} \lambda &= 2\pi \int_0^a R_{nj} r dr, \quad n = 0 \\ &= \pi \int_0^a R_{nj} r dr, \quad n \neq 0 \end{aligned}$$

From (2.63) and (2.64), using (2.65), one finds

$$\left. \begin{aligned} w &= \sum_{n=0}^{\infty} \sum_{j=1}^{\infty} R_{nj} U_{nj} \cos n\theta + \sum_{n=1}^{\infty} \sum_{j=1}^{\infty} R_{nj} W_{nj} \sin n\theta \\ \dot{w} &= \sum_{n=0}^{\infty} \sum_{j=1}^{\infty} R_{nj} V_{nj} \cos n\theta + \sum_{n=1}^{\infty} \sum_{j=1}^{\infty} R_{nj} Z_{nj} \sin n\theta \end{aligned} \right\} \quad (2.66)$$

in which

$$\begin{aligned} U_{nj} &= \frac{1}{p_{nj}} \left\{ M_{nj} - g_{nj} \dot{G}(0) \right\} \sin p_{nj} t + \left\{ H_{nj} - g_{nj} G(0) \right\} \cos p_{nj} t + g_{nj} G(t) \\ V_{nj} &= \left\{ M_{nj} - g_{nj} \dot{G}(0) \right\} \cos p_{nj} t - p_{nj} \left\{ H_{nj} - g_{nj} G(0) \right\} \sin p_{nj} t + g_{nj} \dot{G}(t) \\ W_{nj} &= \frac{1}{p_{nj}} \left\{ N_{nj} - h_{nj} \dot{G}(0) \right\} \sin p_{nj} t + \left\{ L_{nj} - h_{nj} G(0) \right\} \cos p_{nj} t + h_{nj} G(t) \\ Z_{nj} &= \left\{ N_{nj} - h_{nj} \dot{G}(0) \right\} \cos p_{nj} t - p_{nj} \left\{ L_{nj} - h_{nj} G(0) \right\} \sin p_{nj} t + h_{nj} \dot{G}(t) \end{aligned}$$

The deflection is now completely known and the acceleration may also be determined. It is to be remembered, however, that this solution is valid only for the time interval  $(t - \tau)$  during which the parameter  $\bar{N}$  is supposed to remain constant. In Equation (2.66), therefore, the time variable must be  $(t - \tau)$  instead of  $t$ . The parameter  $\bar{N}$  is determined by the first of Equations (2.34) with  $t$  taken at the beginning of the time interval  $(t - \tau)$ . Thus

$$\bar{N} = \frac{6D}{\pi a^2 h^2} \int_0^{2\pi} \int_0^a \left[ \left( \frac{\partial w}{\partial r} \right)^2 + \frac{1}{r^2} \left( \frac{\partial w}{\partial \theta} \right)^2 \right] r dr d\theta \quad t = \tau \quad (2.67)$$

Using (2.63) and (2.66) and (2.50) and (2.51), Equation (2.67) may be written

$$\begin{aligned} \beta^2 - \alpha^2 = & \frac{6}{h^2} \left[ 2 \int_0^a \left\{ \sum_{j=1}^{\infty} \sum_{k=1}^{\infty} R_{0j}^1 R_{0k}^1 H_{0j} H_{0k} \right\} r dr + \right. \\ & + \int_0^a \left\{ \sum_{n=1}^{\infty} \sum_{j=1}^{\infty} \sum_{k=1}^{\infty} R_{nj}^1 R_{nk}^1 (H_{nj} H_{nk} + L_{nj} L_{nk}) \right\} r dr + \\ & \left. + \int_0^a \left\{ \sum_{n=1}^{\infty} \sum_{j=1}^{\infty} \sum_{k=1}^{\infty} n^2 R_{nj} R_{nk} (H_{nj} H_{nk} + L_{nj} L_{nk}) \right\} \frac{dr}{r} \right] \quad (2.68) \end{aligned}$$

in which  $R_{nj}^1 = \frac{dR_{nj}}{dr}$

The integrals in (2.68) cannot, unfortunately, be readily obtained in closed form, and recourse must be had to numerical integration.

#### 2.2.1.4 Summary of Integration Procedure

In numerical integration it is advantageous to use nondimensional quantities. These will be distinguished by placing a bar over the corresponding symbols. Let

$$\bar{w} = \frac{w}{h}$$

$$\bar{t} = \frac{th}{a^2} \sqrt{\frac{E}{12(1 - \nu^2)\rho^*}}$$

where  $\rho^*$  is the mass density of material of the plate

$$\bar{r} = \frac{r}{a}$$

Let  $s$  denote the number of intervals  $\Delta$  from time zero. Then the deflections and velocities at the end of the  $s^{\text{th}}$  interval are given by

$$\left. \begin{aligned} \bar{w}_s &= \sum_{j=1}^{\infty} \sum_{n=0}^{\infty} R_{nj_s} U_{nj_s} \cos n\theta + \sum_{j=1}^{\infty} \sum_{n=1}^{\infty} R_{nj_s} W_{nj_s} \sin n\theta \\ \dot{\bar{w}}_s &= \sum_{j=1}^{\infty} \sum_{n=0}^{\infty} R_{nj_s} V_{nj_s} \cos n\theta + \sum_{j=1}^{\infty} \sum_{n=1}^{\infty} R_{nj_s} Z_{nj_s} \sin n\theta \end{aligned} \right\} \quad s \geq 1 \quad (2.69)$$

The  $R_{nj}$  are defined by Equation (2.52) and:

$$\left. \begin{aligned}
U_{nj_s} &= \frac{1}{p_{nj_s}} \left\{ M_{nj_s} - g_{nj_s} \dot{G}[\Delta(s-1)] \right\} \sin(p_{nj_s} \Delta) + \\
&\quad + \left\{ H_{nj_s} - g_{nj_s} G[\Delta(s-1)] \right\} \cos(p_{nj_s} \Delta) + g_{nj_s} G[\Delta s] \\
V_{nj_s} &= \left\{ M_{nj_s} - g_{nj_s} \dot{G}[\Delta(s-1)] \right\} \cos(p_{nj_s} \Delta) - \\
&\quad - p_{nj_s} \left\{ H_{nj_s} - g_{nj_s} G[\Delta(s-1)] \right\} \sin(p_{nj_s} \Delta) + g_{nj_s} \dot{G}[\Delta s] \\
W_{nj_s} &= \frac{1}{p_{nj_s}} \left\{ N_{nj_s} - h_{nj_s} \dot{G}[\Delta(s-1)] \right\} \sin(p_{nj_s} \Delta) + \\
&\quad + \left\{ L_{nj_s} - h_{nj_s} G[\Delta(s-1)] \right\} \cos(p_{nj_s} \Delta) + h_{nj_s} G[\Delta s] \\
Z_{nj_s} &= \left\{ N_{nj_s} - h_{nj_s} \dot{G}[\Delta(s-1)] \right\} \cos(p_{nj_s} \Delta) - \\
&\quad - p_{nj_s} \left\{ L_{nj_s} - h_{nj_s} G[\Delta(s-1)] \right\} \sin(p_{nj_s} \Delta) + h_{nj_s} \dot{G}[\Delta s]
\end{aligned} \right\} \quad s \geq 1 \quad (2.70)$$

and

$$\left. \begin{aligned}
H_{nj_s} &= \frac{\sum_{k=1}^{\infty} \int_0^1 U_{nk_{s-1}} R_{nk_{s-1}} R_{nj_s} \bar{r} d\bar{r}}{\int_0^1 R_{nj_s}^2 \bar{r} d\bar{r}}, \quad n \geq 0, \quad s \geq 2 \\
M_{nj_s} &= \frac{\sum_{k=1}^{\infty} \int_0^1 V_{nk_{s-1}} R_{nk_{s-1}} R_{nj_s} \bar{r} d\bar{r}}{\int_0^1 R_{nj_s}^2 \bar{r} d\bar{r}}, \quad n \geq 0, \quad s \geq 2 \\
L_{nj_s} &= \frac{\sum_{k=1}^{\infty} \int_0^1 W_{nk_{s-1}} R_{nk_{s-1}} R_{nj_s} \bar{r} d\bar{r}}{\int_0^1 R_{nj_s}^2 \bar{r} d\bar{r}}, \quad n > 0, \quad s \geq 2 \\
N_{nj_s} &= \frac{\sum_{k=1}^{\infty} \int_0^1 Y_{nk_{s-1}} R_{nk_{s-1}} R_{nj_s} \bar{r} d\bar{r}}{\int_0^1 R_{nj_s}^2 \bar{r} d\bar{r}}, \quad n > 0, \quad s \geq 2
\end{aligned} \right\} \quad (2.71)$$

and  $H_{nj_1}$ ,  $L_{nj_1}$ ,  $M_{nj_1}$ , and  $N_{nj_1}$  are defined by the initial conditions.

The natural frequencies are given by

$$p_{nj_s} = \beta_{nj_s} a_{nj_s} \quad s \geq 1 \quad (2.72)$$

$$\left. \begin{aligned}
\beta_s^2 - \alpha_s^2 = 12 \int_0^1 \left\{ \sum_{j=1}^{\infty} \sum_{k=1}^{\infty} R'_{Oj_s} R'_{Ok_s} H_{Oj_s} H_{Ok_s} \right\} \bar{r} d\bar{r} + \\
+ 6 \int_0^1 \left\{ \sum_{n=1}^{\infty} \sum_{j=1}^{\infty} \sum_{k=1}^{\infty} R'_{nj_s} R'_{nk_s} (H_{nj_s} H_{nk_s} + L_{nj_s} L_{nk_s}) \right\} \bar{r} d\bar{r} + \\
+ 6 \int_0^1 \left\{ \sum_{n=1}^{\infty} \sum_{j=1}^{\infty} \sum_{k=1}^{\infty} n^2 R_{nj_s} R_{nk_s} (H_{nj_s} H_{nk_s} + L_{nj_s} L_{nk_s}) \right\} \frac{dr}{r}
\end{aligned} \right\} \begin{matrix} s \geq 1 \\ (2.73) \end{matrix}$$

with

$$R'_{Oj_s} = \frac{dR_{Oj_s}}{d\bar{r}}$$

Some of the above relations may be simplified by noting that if  $\Delta$  is taken sufficiently small

$$\begin{aligned}
R_{nj_s - 1} &\approx R_{nj} \\
\int_0^1 R_{nk_s - 1} R_{nj_s} \bar{r} d\bar{r} &\approx 0 \quad k \neq j
\end{aligned}$$

Equations (2.71) then become

$$\left. \begin{aligned}
H_{nj_s} &\approx U_{nj_s - 1} & n \geq 0 \\
M_{nj_s} &\approx V_{nj_s - 1} & n \geq 0 \\
L_{nj_s} &\approx W_{nj_s - 1} & n > 0 \\
N_{nj_s} &\approx Y_{nj_s - 1} & n > 0
\end{aligned} \right\} \begin{matrix} s \geq 2 \\ (2.74) \end{matrix}$$

Equation (2.73) simplifies to

$$\begin{aligned}
\beta_s^2 - \alpha_s^2 = 12 \sum_j \sum_k \xi_{ojk} H_{Oj_s} H_{Ok_s} + 6 \sum_n \sum_j \sum_k \xi_{nj_k} (H_{nj_s} H_{nk_s} + L_{nj_s} L_{nk_s}) + \\
+ 6 \sum_n \sum_j \sum_k \eta_{nj_k} n^2 (H_{nj_s} H_{nk_s} + L_{nj_s} L_{nk_s})
\end{aligned} \quad (2.75)$$

where

$$\left. \begin{aligned}
\xi_{ojk} &= \int_0^1 R'_{Oj_o} R'_{Ok_o} \bar{r} d\bar{r} \\
\xi_{nj_k} &= \int_0^1 R'_{nj_o} R'_{nk_o} \bar{r} d\bar{r} \\
\eta_{nj_k} &= \int_0^1 R_{nj_o} R_{nk_o} \frac{d\bar{r}}{\bar{r}}
\end{aligned} \right\} \quad (2.76)$$

If the right-hand side of (2.75) is evaluated for any value of  $s$ , then setting

$$\begin{aligned}
\beta_s^2 - \alpha_s^2 &= 4.2 \phi & \text{for simply supported plate} \\
&= 14.68 \phi & \text{for clamped plate}
\end{aligned}$$

one may determine  $\phi$  and thereby the values of  $\alpha_{nj_s}$  and  $\beta_{nj_s}$  if these have been tabulated for various values of  $\phi$ . [See note under Equation (2.51).] Equation (2.72) may then be used to determine the nondimensional frequencies.

#### 2.2.1.5 Numerical Example

The response of a circular plate to a loading pulse will be investigated by the method described on the preceding page.

A blast of short duration is best treated as an impulse. Assuming that the blast is delivered uniformly over the area of the plate, let

$$\pi a^2 \int_0^\epsilon f(t) dt = I$$

$\epsilon$  being the time at which the pulse decays to zero.

By the momentum principle, the uniform starting velocity is

$$v_0 = \frac{I}{M} \quad (2.77)$$

where  $M$  is the total mass of the plate.

The plate under consideration has the following geometric and material properties

$$a = 6", \quad E = 30 \times 10^6 \text{ psi}, \quad \rho^* = 7.34 \times 10^{-4} \text{ lb sec}^2 \text{ in}^{-4}$$

Thus,

$$\frac{a^2}{h^2} \sqrt{\frac{12(1 - \nu^2)\rho^*}{E}} = 0.45 \text{ sec in}^{-1}$$

The initial velocity  $v_0$ , calculated from the characteristics of the charge (used in an experiment, the details of which are omitted here) and relation (2.77) above gives an estimated initial velocity of 893 in. sec<sup>-1</sup>. Thus, the nondimensional initial velocity is

$$\bar{v}_0 = 893 \times 0.45 \approx 400$$

The response of the plate will be analyzed on the assumption that the plate receives a uniform velocity of 400 while at rest.

The parameter

$$\frac{h}{a^2} \sqrt{\frac{E}{12(1 - \nu^2)\rho^*}} = 61.6$$

Thus

$$\bar{t} = 61.6 t$$

This gives the relation between nondimensional time  $\bar{t}$  and true time  $t$ . The nondimensional time interval  $\Delta$  will be taken as 0.0616. This corresponds to a true time interval of one millisecond.

The basic equations given in Section 2.2.1.4 can be simplified considerably because of axial symmetry. In what follows, the bars over the nondimensional quantities will be dropped. No confusion can arise as all quantities henceforth are nondimensional.

Equations (2.69) become

$$\left. \begin{aligned} w_s &= \sum_{j=1}^{\infty} R_{oj1} U_{oj_s} \\ \dot{w}_s &= \sum_{j=1}^{\infty} R_{oj1} V_{oj_s} \end{aligned} \right\} s \geq 1 \quad (2.78)$$

From Equations (2.70), (2.71) and (2.74)

$$\left. \begin{aligned} H_{oj_s} &= U_{oj_{s-1}} = \frac{M_{oj_{s-1}}}{P_{oj_{s-1}}} \sin(p_{oj_{s-1}} \Delta) + H_{oj_{s-1}} \cos(p_{oj_{s-1}} \Delta) \\ M_{oj_s} &= V_{oj_{s-1}} = M_{oj_{s-1}} \cos(p_{oj_{s-1}} \Delta) - P_{oj_{s-1}} H_{oj_{s-1}} \sin(p_{oj_{s-1}} \Delta) \end{aligned} \right\} s \geq 2 \quad (2.79)$$

The initial conditions give

$$\begin{aligned} H_{oj1} &= 0 \\ M_{oj1} &= v_o \int_0^1 R_{oj1} r dr \bigg/ \int_0^1 R_{oj1}^2 r dr \end{aligned}$$

where

$$R_{oj} = J_0(a_{j1} r) - \frac{J_0(a_{j1})}{I_0(a_{j1})} I_0(a_{j1} r)$$

with

$$\begin{aligned} a_{j1} &= 2.222 \text{ for } j = 1 \\ &= 5.452 \text{ for } j = 2 \end{aligned}$$

$$p = a_{j1}^2$$

Thus

$$\left. \begin{aligned} U_{oj1} &= \frac{M_{oj1}}{P_{oj1}} \sin(p_{oj1} \Delta) \\ V_{oj1} &= M_{oj1} \cos(p_{oj1} \Delta) \end{aligned} \right\} \quad (2.80)$$

From Equation (2.72)

$$P_{oj_s} = a_{oj_s} \beta_{oj_s} \quad s \geq 1 \quad (2.81)$$

Using  $j = 1, 2$  only, Equation (2.73) becomes

$$\begin{aligned} \beta_s^2 - a_s^2 &= 12 H_{o1s}^2 \int_0^1 \left( \frac{dR_{o1s}}{dr} \right)^2 r dr + 24 H_{o1s} H_{o2s} \int_0^1 \frac{dR_{o1s}}{dr} \frac{dR_{o2s}}{dr} r dr + \\ &+ 12 H_{o2s}^2 \int_0^1 \left( \frac{dR_{o2s}}{dr} \right)^2 r dr \quad s \geq 1 \end{aligned} \quad (2.82)$$

Assuming that the plate is simply supported

$$\beta_s^2 - a_s^2 = 4.2 \phi_s$$

Thus,  $\phi_s$  is known, and  $a_s$  and  $\beta_s$  may be read from charts already prepared.

## 2.2.2 Plastic Collapse

### LIST OF SYMBOLS

$v$	initial velocity given to membrane, a constant
$U$	radial velocity of flat portion of membrane, positive outward
$R$	radius of flat portion of membrane
$\dot{R}$	radial velocity of bending wave
$a$	initial radius of membrane
$h$	initial thickness of membrane
$\rho$	mass density of membrane material
$t$	time
$r$	radius of position of any particle in the flat portion of membrane at any time
$r_0$	initial radius corresponding to $r$
$H$	thickness of membrane at any time
$\sigma_r$	radial stress
$\sigma_\theta$	circumferential stress
$\sigma$	yield stress in tension
$\epsilon_r, \epsilon_\theta$	natural (logarithmic) strains in the radial and circumferential directions
$Z$	distance of central flat portion from initial plane of the diaphragm
$\nu$	Poisson's ratio
$E$	modulus of elasticity
$\beta$	$= R/a$
$\mu$	$= U/v$
$\eta$	$= H/h$
$c^2$	$= \sigma / \rho$
$\xi$	$= vt/a = Z/a$
$\delta$	$= 4\sigma / \rho v^2$
$\kappa$	$= [(4\sigma / \rho v^2) \sigma (1 - \nu) / E]^{1/2}$

In investigating this problem it was discovered that there are certain existing solutions to corresponding problems in underwater shock which have been satisfactorily verified experimentally. While the problems of blast effects in air or of soft radiation are by no means the same as the effects of blast loads underwater, they are sufficiently similar to warrant the supposition that, as a first approximation, the two problems may be studied by identical procedures.

The solution to the plastic collapse of a diaphragm proposed by Hudson<sup>(2.8)</sup>, and a similar solution by Frederick<sup>(2.9)</sup>, refer specifically to underwater shock. It is proposed now to use the results of these analyses, particularly that by Hudson, to predict the collapse of plates due to blast effects in air. These predictions will then be subjected to experimental checks under the test program at present being formulated. If it is found that the discrepancies between theoretical and experimental results are sufficiently serious, a fresh theoretical analysis will then be undertaken. It is believed that this approach will lead to the greatest economy of effort in the overall program.

#### 2.2.2.1 Summary of the Hudson Approach

The problem attacked by Hudson is the damage done by underwater explosions to thin metal circular diaphragms, air backed, and held rigidly at the peripheries. The material of the diaphragm is supposed to be rigid-perfectly plastic. Although Hudson has also given an approximate solution for a work-hardening material, the primary difference noted is that in the work-hardening solution the apex of the cone (the final shape assumed by the diaphragm) is rounded off, whereas in the perfectly plastic material the apex is a point. For the present purposes, it appears sufficient to fix attention on the solution for the rigid-perfectly plastic material.

The shape assumed by the diaphragm at any time  $t < t_s$ , where  $t_s$  is the total time for deflection or "swing time," is that of a truncated cone as shown in Figure 2.3. The flat central region travels with a constant speed  $v$  normal to its plane, decreasing in radius with its motion, the diaphragm finally assuming the shape of a cone with a zero thickness at the apex.

While an explicit form of the solution of the equations of motion is not given even for the highly idealized model proposed by Hudson, certain special cases can be solved and information gleaned regarding the following:

- (1) The radius  $R$  of the bending wave (see Fig. 2.3) as a function of time
- (2) The diaphragm profile at each instant
- (3) The thickness distribution
- (4) Displacement-time curves of particles in diaphragm
- (5) Stress and strain distributions
- (6) The center deflection as a function of  $v$
- (7) The total time for the deformation to take place

The solutions given by Hudson are summarized below.

#### 2.2.2.2 An Elementary Approximation to the Solution

When the acceleration of the material in the flat central portion is negligibly small throughout the motion, i.e.,  $U$  is a constant, the solution is as follows

$$\left. \begin{aligned} U &= v^2/2c & (a) \\ R &= a - ct & (b) \\ H &= h \left( \frac{R}{a} \right) (v/c)^2 & (c) \\ Z &= \frac{v}{c} (a - R) & (d) \end{aligned} \right\} \quad (2.83)$$

The thickness distribution in the deformed diaphragm given by (2.83 c) shows a dimpling tendency at the center. In fact, at the last moment, the thickness becomes zero at the center. However, as the variation of the thickness with  $R$  is so rapid near  $R = 0$ , the tiny pinhole may not be very apparent experimentally.

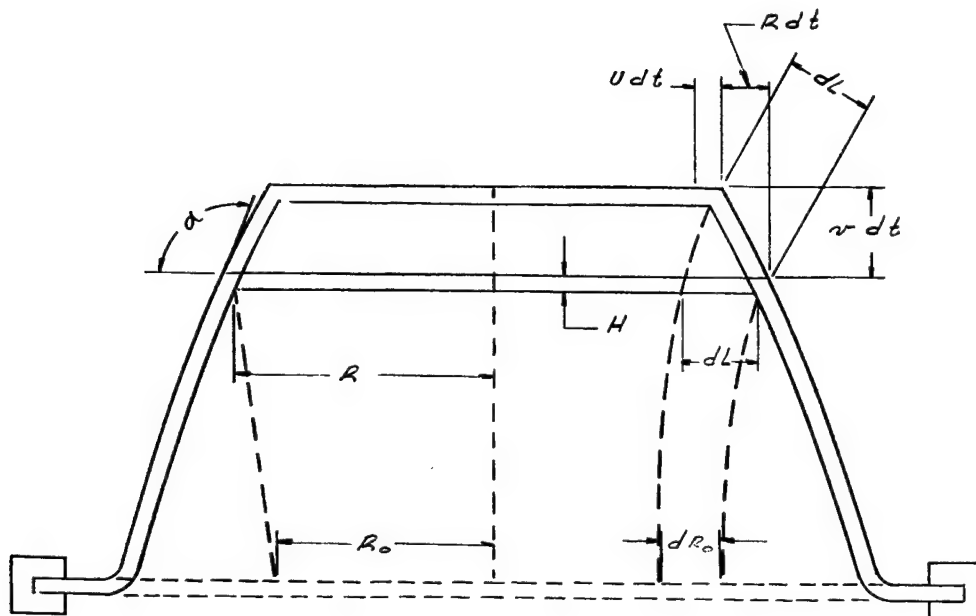


FIGURE 2.3. A SKETCH OF THE DIAPHRAGM CONFIGURATIONS AT TWO SUCCESSIVE INSTANTS,  $t$  AND  $t+dt$ . THE VARIOUS QUANTITIES WHICH ENTER INTO THE SEVERAL GEOMETRIC AND KINEMATIC RELATIONS ARE PORTRAYED HERE

Equation (2.83 d) shows that the diaphragm assumes a conical shape whose center deflection is proportional to the initial velocity  $v$ .

The total time of deflection  $t_s$  is given by

$$t_s = a/c \quad (2.84)$$

### 2.2.2.3 The Exact Solution for a Rigid-Perfectly Plastic Material

$$\left. \begin{aligned} \frac{R}{a} = \beta(\mu) &= \left( \frac{\mu^2 - x_1}{\kappa^2 - x_1} \right)^{\frac{1}{2}(x_1 - 1)/(x_1 - x_2)} \times \left( \frac{\mu^2 - x_1}{\kappa^2 - x_2} \right)^{\frac{1}{2}(x_2 - 1)/(x_2 - x_1)} & (a) \\ \frac{H}{h} = \eta(\mu) &= \left( \frac{\mu^2 - x_1}{\kappa^2 - x_1} \right)^{-2(x_1)/(x_1 - x_2)} \times \left( \frac{\mu^2 - x_2}{\kappa^2 - x_2} \right)^{-2(x_2)/(x_2 - x_1)} & (b) \\ \frac{Z}{a} = \zeta(\mu) &= \int_{\kappa}^{\mu} \frac{2\mu^2}{(\mu^2 - x_1)(\mu^2 - x_2)} \beta(\mu) d\mu & (c) \end{aligned} \right\} \quad (2.85)$$

where  $x_1, x_2$  are the smaller and larger (positive) roots respectively of the quadratic equation

$$x^2 - (2\delta - 3)x + 2 = 0 \quad (2.86)$$

It is to be noted that the initial conditions are

$$\beta = \eta = 1, \mu = \kappa \text{ when } \zeta = 0$$

Equation (2.85 c) is not integrable in terms of elementary functions.

For positive values of  $\delta$ , which are the only ones of physical interest, the roots of (2.86) occur in pairs of positive values for  $\frac{3}{2} + \sqrt{2} \leq \delta \leq \infty$  and as pairs of negative values for  $0 \leq \delta \leq \frac{3}{2} - \sqrt{2}$  (a very small range). For intermediate values of  $\delta$ , the roots are complex. Hudson confines himself to a consideration of values of  $\delta \geq \frac{3}{2} + \sqrt{2}$ . At the lower limit of this range, corresponding to very large  $v$ , or small  $\sigma$ , values, we have  $x_1 = x_2 = \sqrt{2}$ . As  $\delta$  becomes very large,  $\sqrt{2} > x_1 \rightarrow 0$  and  $\sqrt{2} < x_2 \rightarrow \infty$ .

A case of considerable interest arises when  $\kappa^2$  coincides with one of the roots of (2.86).

From (2.85), it is seen that the only possibility is for  $\mu^2$  itself to be constant and equal to  $\kappa^2$ . It can then be shown that either  $0 \leq \mu = \kappa \leq 1$ , or  $\mu = -\kappa \leq -1$ . The first case only is admissible, since the second precludes  $\mu = \kappa$  initially. Thus, we have

$$0 \leq \mu^2 = \kappa^2 = x_1 = \left( \delta - \frac{3}{2} \right) - \left\{ \left( \delta - \frac{3}{2} \right)^2 - 2 \right\}^{1/2} \leq 1$$

and

$$\delta \geq 3$$

The solution is then as follows

$$\left. \begin{aligned}
 R &= a - \frac{1 - \kappa^2}{2\kappa} vt = a - \frac{1 - \kappa^2}{2\kappa} Z & (a) \\
 H &= h \left( \frac{R}{a} \right)^{4(\kappa^2)/(1 - \kappa^2)} & (b) \\
 U &= \kappa v & (c) \\
 \delta &= 4 \frac{c^2}{v^2} = \frac{\kappa^4 + 3\kappa^2 + 2}{2\kappa^2} \geq 3 & (d)
 \end{aligned} \right\} \quad (2.87)$$

For  $\kappa = 1$ ,  $\delta = 3$  and  $v = (2/\sqrt{3})c$ , and the deformed diaphragm is cylindrical, i.e., it ruptures completely.

For other allowed values of  $\kappa (= \mu)$ , this solution is quite similar to the elementary approximation presented earlier, even quantitatively, provided  $\delta$  is large. For it follows then

$$\kappa \approx 1/\delta^{1/2} = v/2c \ll 1, \quad (\delta \gg 3)$$

and (2.87) reduces to (2.83).

Another case of interest arises if  $\kappa$  has any desired positive value within reason and  $\delta$  is very large. Then  $x_1$  is small and  $x_2$  is large. Assume that  $\kappa^2/x_2 \ll 1$ , as is  $\mu^2/x_2$  (since  $\mu^2$  varies from  $\kappa^2$  to  $x_1$ ). Under these simplifying conditions, it is possible to derive an approximate integral of (2.85 c). It is then found that

$$x_1 \approx 1/\delta, \quad x_2 \approx 2\delta \gg 1$$

Then providing  $\delta$  is large enough

$$\left. \begin{aligned}
 \frac{Z}{a} &= \frac{vt}{a} = 2Uv/(v^2 - U^2) [1 - (R/a)] & (a) \\
 \frac{H}{h} &= \left( \frac{R}{a} \right)^{(v/c)^2} & (b) \\
 \frac{U}{v} &= \frac{v}{2c} \left\{ 1 + \left( 4\kappa^2 \frac{c^2}{v^2} - 1 \right) \left( \frac{R}{a} \right)^{16(c/v)^2} \right\}^{1/2} & (c)
 \end{aligned} \right\} \quad (2.88)$$

It may be shown that this approximation is uniform over the range of  $U/v$  from  $\kappa$  to  $v/2c$ , and the range of  $R/a$  from 1 to 0; but the nearer  $\kappa$  is to 1 the larger  $\delta$  must be. If  $\kappa = 0$ , which is the case of a material which has strictly no elastic strain range, the deflected shape of the diaphragm described by (2.88 a) is conical near the center with a central deflection the same as that given by the elementary theory under 2.2.2.2.

#### 2.2.2.4. General Remarks

It may be noted that the modulus of elasticity  $E$  enters into the definition of  $\kappa$ . This is because, although the elastic phase of the material is neglected in the specification of the deformations, an estimate has been made of the initial conditions at the end of the elastic range. The time at which elastic phase is completed is of the order of magnitude of 3% of  $t_s$  for some steels. Thus, it is generally immaterial whether time is reckoned from the end of the elastic strain range or before it.

Whether the above analysis, developed with specific reference to diaphragms, would apply to plates of the proportions of interest in the present research program can only be determined by careful experimentation and photographic records of the deformation.

Some additional results which may be of value in checking the theory are

$$\left. \begin{aligned} \sigma_r &= \sigma_\theta = \sigma \\ \epsilon_r &= \epsilon_\theta = \log (r/r_o) \\ \epsilon_H &= \log H/h \end{aligned} \right\} \quad (2.89)$$

## REFERENCES

- 2.1 Fung, Y. C. and Sechler, E. E., "Instability of Thin Elastic Shells," Proc., First Symposium of Naval Structural Mechanics, Pergamon Press, New York, 1960.
- 2.2 Th. von Kármán, "Encyklopädie der Mathematischen Wissenschaften," vol IV<sub>4</sub>, p 349, 1910.
- 2.3 G. Hermann, "Influence of Large Amplitudes on the Flexural Motions of Elastic Plates," NACA TN 3578.
- 2.4 Hu-Nan Chu and G. Hermann, "Influence of Large Amplitudes on Free Flexural Vibrations of Rectangular Plates," Journal of Applied Mechanics, p 532, December 1956.
- 2.5 H. M. Berger, "A New Approach to the Analyses of Large Deflections of Plates," Journal of Applied Mechanics, p 465, December 1955.
- 2.6 W. A. Nash and J. R. Modeer, "Certain Approximate Analyses of the Nonlinear Behavior of Plates and Shallow Shells." Proceedings of the Symposium on the Theory of Thin Elastic Shells, Delft, August 1959, Interscience Publishers, Inc., New York, 1960.
- 2.7 N. W. McLachlan, "Bessel Functions for Engineers, Edition, Oxford, 1955.
- 2.8 G. E. Hudson, "A Theory of the Dynamic Plastic Deformation of a Thin Diaphragm," Journal of Applied Physics, Vol. 22, No. 1, Jan. 1951, p 1.
- 2.9 Daniel Frederick, "A Simplified Analysis of Circular Membrane Subjected to an Impulsive Loading Producing Large Plastic Deformations," 4th Midwestern Conference on Solid Mechanics, 1959, p 18.

### 3. NUMERICAL ANALYSIS - CYLINDRICAL SHELLS (LINEAR-ELASTIC, SMALL DEFLECTIONS)

The computations utilized the following geometries and materials for the cylindrical models used in the experimental investigation

$$\begin{aligned} a &= 6'' & \nu &= 1/3 \\ L &= 36'' & E &= 2.9 \times 10^7 \text{ (psi)} \\ h &= .036'' & \rho &= 7.36 \times 10^{-4} \left( \frac{\text{lb-sec}^2}{\text{in}^4} \right) \end{aligned}$$

The analyses began with determining the free vibration circular frequency utilizing the values obtained for the frequency factor ( $\psi$ ) in Equation (I. 13) for the appropriate values of  $\kappa$  [ see Eqs. (2. 9), (2. 16) or (2. 17)] in the relationship

$$\omega_{mn} = (12.3\psi_{mn})^{1/2} \times 10^4 \quad (3. 1)$$

The variation of the circular frequency with the end-closure stiffness (R) for various values of m and n are shown in Figure 3. 20.

The computations in all cases were directed toward obtaining pertinent radial displacements from the relation

$$w(x, \phi, t) = \sum w_{mn}(x, \phi) q_{mn}(t) \quad (3. 2)$$

Values for  $q_{mn}(t)$  in Equation (3. 1) were acquired from Equation (I. 27) [ or in finite difference form, Eq. (I. 28)], which entailed obtaining the generalized force and generalized mass.

#### 3. 1 Simply Supported End-Closures

For the generalized force [ see Eq. (I. 27); Appendix I], taking the loading as being uniformly distributed along the length of the shell, we have

$$Q_{mn}(t) = a \int_0^{2\pi} \left[ P(\phi, t) \int_0^L w_{mn}(x, \phi) dx \right] d\phi \quad (3. 3)$$

From Equation (2. 15)

$$Q_{mn}(t) = \frac{2LaC_4}{n\pi} \int_0^{2\pi} P(\phi, t) \cos m\phi d\phi \quad (n = 1, 3, 5, \dots) \quad (3. 4)$$

Taking into consideration the loading symmetry and using cylinder surface increments of  $\phi = 22.5^\circ$ , Equation (3. 4) becomes

$$\begin{aligned} Q_{mn}(t) = \frac{4LaC_4}{n\pi} & \left[ \int_0^{11.25} P_0(t) \cos m\phi d\phi + \sum_{\phi_1}^{\phi_1 + 22.5} \int_{\phi_1}^{\phi_1 + 22.5} P_{\phi_1 + 11.25}(t) \cos m\phi d\phi \right. \\ & \left. + \int_{168.75}^{180} P_{180}(t) \cos m\phi d\phi \right] \quad (3. 5) \end{aligned}$$

The values of  $P_\phi(t)$  for time increments of 0.1 msec were obtained from load profiles similar to those shown in Figure I. 10, Appendix I. The time variation of  $Q_{mn}(t)$ , as acquired from Equation (3.5) for  $P_I = 33$  psi and  $t_+ = 1$  msec, is shown in Figure 3.1.

From Equation (2.15) [and Eqs. (2.11)], the expression for the generalized mass [see Eq. (I.27), Appendix I] becomes

$$M_{mn} = \frac{Lh\rho\pi a C_4^2}{2} \left[ 1 + \left( \frac{K_2}{K_1} \right)^2 + \left( \frac{K_3 n \pi}{K_1 L} \right)^2 \right] \quad (3.6)$$

The frequencies and the corresponding values of the terms within the brackets of Equation (3.6) are given in Table 3.1.

In each of the computations, only the lowest of three, real frequencies obtained from Equation (I.13) was used. This frequency was associated with the response where the radial displacement ( $w$ ) was predominant. An indication of the contributions made by the longitudinal ( $u$ ) and tangential ( $v$ ) displacements may be found in Table 3.1 where sample values of  $K_2/K_1$  (reflecting the tangential displacements) and  $K_3 n \pi / K_1 L$  (reflecting the longitudinal displacements) are given. Here, it is seen that, although these values are greater than unity, they are at the same time associated with much higher frequencies. Since the value of the generalized mass is increased [Eq. (3.6)] and the larger frequencies dictate smaller values of  $\Delta t$  in Equation (I.28), the net result is a drastic decrease in the values of  $q_{mn}(t)$ . This clearly shows that the contribution of the longitudinal and tangential displacements is quite negligible when compared with that of the radial displacement.

The ratio of the generalized force to the generalized mass appearing in Equations (I.27) and (I.28) is, in accordance with Equations (3.5) and (3.6)

$$\frac{Q_{mn}(t)}{M_{mn}} = \frac{4}{nh\rho\pi^2 C_4} \frac{\sum_{\phi_1} \int_{\phi_1} P_\phi(t) \cos m\phi d\phi}{1 + \left( \frac{K_2}{K_1} \right)^2 + \left( \frac{K_3 n \pi}{K_1 L} \right)^2} \quad \begin{matrix} (m = 2, 3, \dots) \\ (n = 1, 3, 5, \dots) \end{matrix} \quad (3.7)$$

where, for the particular shell properties previously listed

$$\frac{4}{nh\rho\pi^2} = \frac{1.53 \times 10^6}{n}$$

From Equation (I.28), the variations of  $q_{mn}(t)$  with time are obtained for particular values of  $P_I$  and  $t_+$ . These are shown in Figures 3.2 through 3.13. As a final step, Equation (3.2) is utilized to obtain the value of the radial displacement for each point on the cylinder's surface as defined by  $x$  and  $\phi$ . In Figures 3.2 through 3.13 are shown the variation of  $w(x, \phi, t)$  with time for the point at  $x = L/2$  and  $\phi = 0^\circ$ . (See also Table 3.2)

### 3.2 Fixed End-Closures

For cylinders with fixed boundary conditions, the expression for the generalized force [see Eqs. (2.13) and (3.3)] for a load uniformly distributed along the length of the shell is

$$Q_{mn}(t) = \frac{LaC}{\Gamma_1'' \kappa} \beta(\kappa) \int_0^{2\pi} P(\phi, t) \cos m\phi d\phi \quad (3.8)$$

where

$$\beta(\kappa) = \Gamma_2(\cosh \kappa + \cos \kappa - 2) + \Gamma_3(\sin \kappa - \sinh \kappa)$$

$$\Gamma_1'' = \sinh \kappa - \cosh \kappa + \sin \kappa + \cos \kappa$$

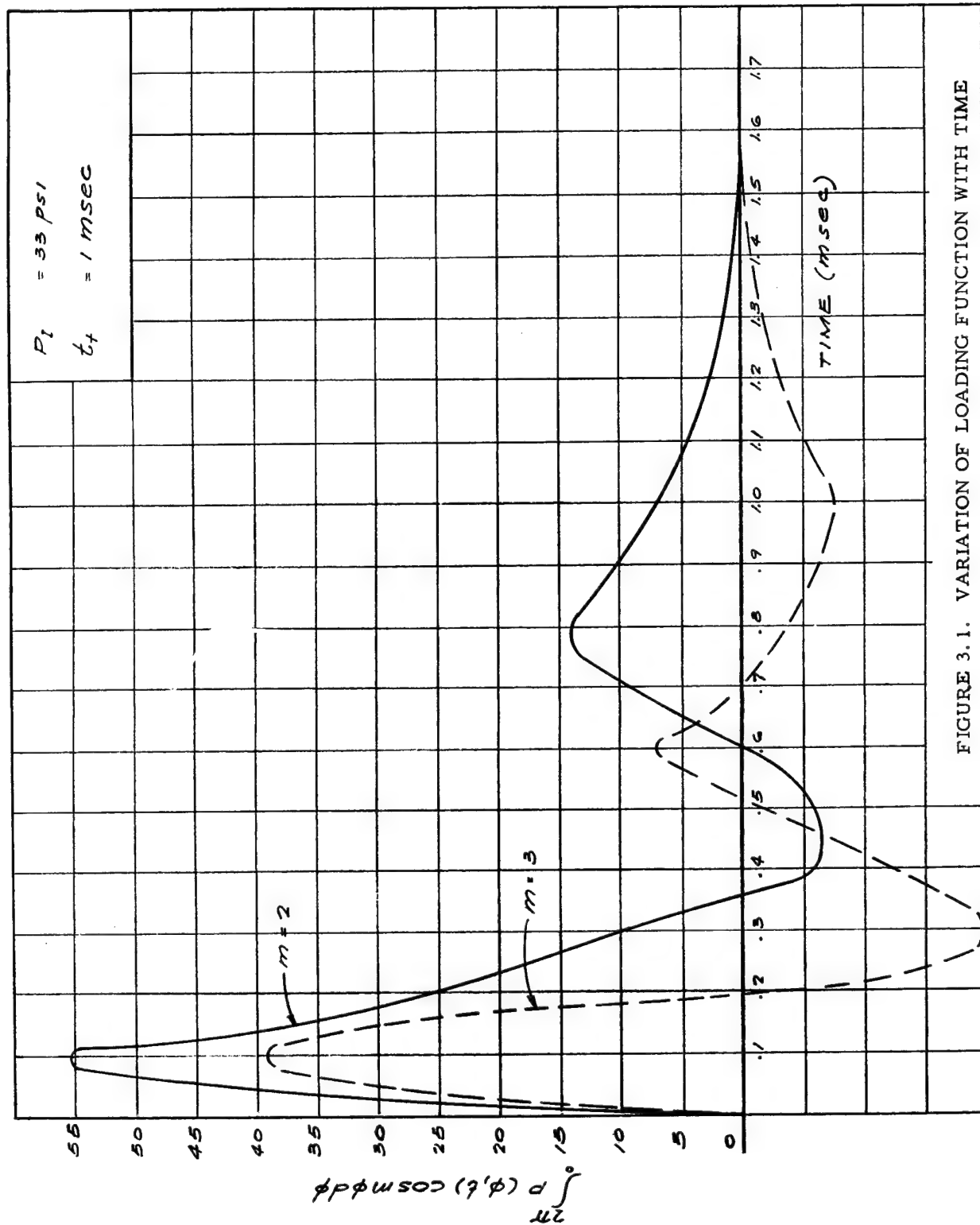


FIGURE 3.1. VARIATION OF LOADING FUNCTION WITH TIME

TABLE 3.1. FREQUENCIES AND RELATED QUANTITIES FOR CYLINDRICAL SHELLS WITH SIMPLY SUPPORTED END-CLOSURES

$\underline{m}$	$\underline{n}$	$\underline{\omega_{mn}}$ (rad/sec)	$\underline{f_{mn}}$ (cycles/sec)	$\underline{\frac{K_2^{(1)}}{K_1}}$	$\underline{\frac{K_{3n\pi}^{(1)}}{K_1 L}}$	$\underline{1 + \left(\frac{K_2}{K_1}\right)^2 + \left(\frac{K_{3n\pi}}{K_1 L}\right)^2}^{(2)}$	$\underline{2 - \omega_{mn}^2 (\Delta t)^2}^{(3)}$
2	1	78,430	12,480	2.00	.43	5.17	-
2	1	2,020	320	.50	.13	1.27	1.96
2	1	40,430	6,430	.75	78.7	620.2	-
3	1	110,900	17,650	2.0	.48	5.22	-
3	1	1,110	180	.33	.06	1.11	1.99
3	1	60,730	9,700	.33	292.7	85,680	-
2	3	23,450	3,730	.57	.74	1.87	-
3	3	8,700	380	.33	.18	1.14	1.81
4	3	5,050	800	.25	.10	1.07	1.64

(1) See Eq. I.12, Appendix I

(2) See Eq. 3.6

(3) See Eq. I.28, Appendix I ( $\Delta t = .0001$  sec or  $5 \times 10^{-5}$  sec)

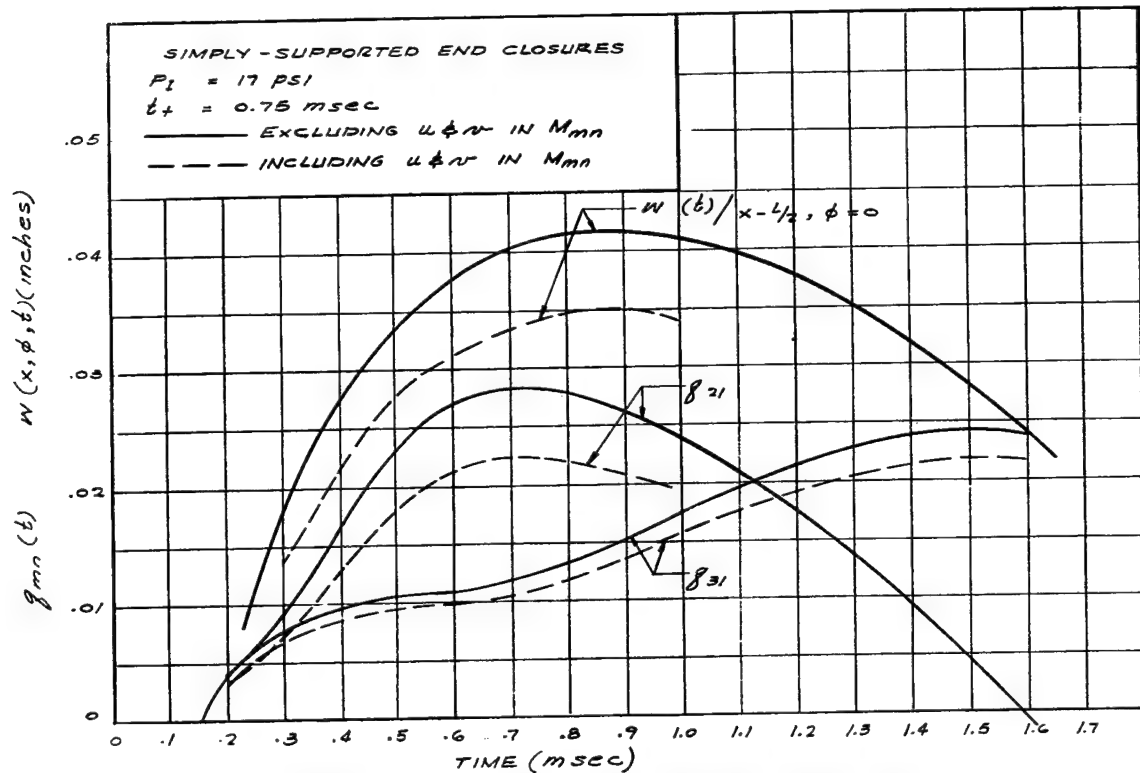


FIGURE 3.2. VARIATION OF  $g_{mn}(t)$  AND RADIAL DISPLACEMENT  $w(t)$  AT  $x = L/2, \phi = 0^\circ$  FOR CYLINDRICAL SHELL

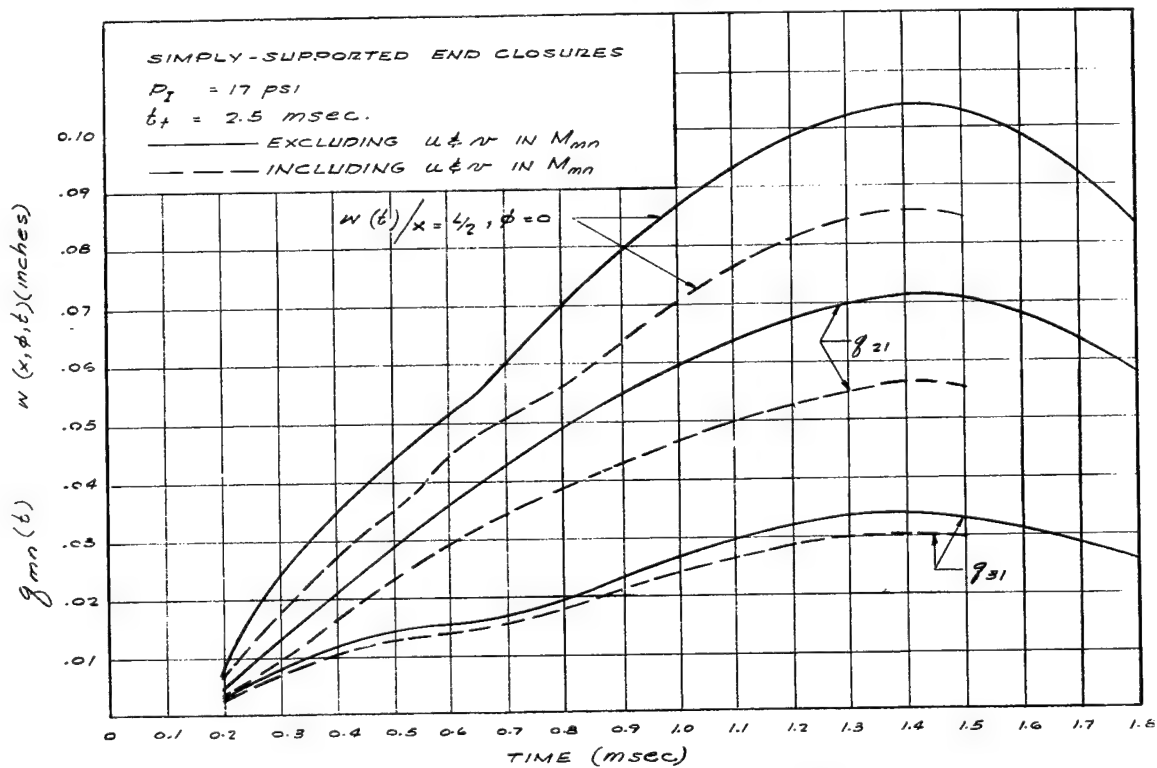


FIGURE 3.3. VARIATION OF  $g_{mn}(t)$  AND RADIAL DISPLACEMENT  $w(t)$  AT  $x = L/2, \phi = 0^\circ$  FOR CYLINDRICAL SHELL

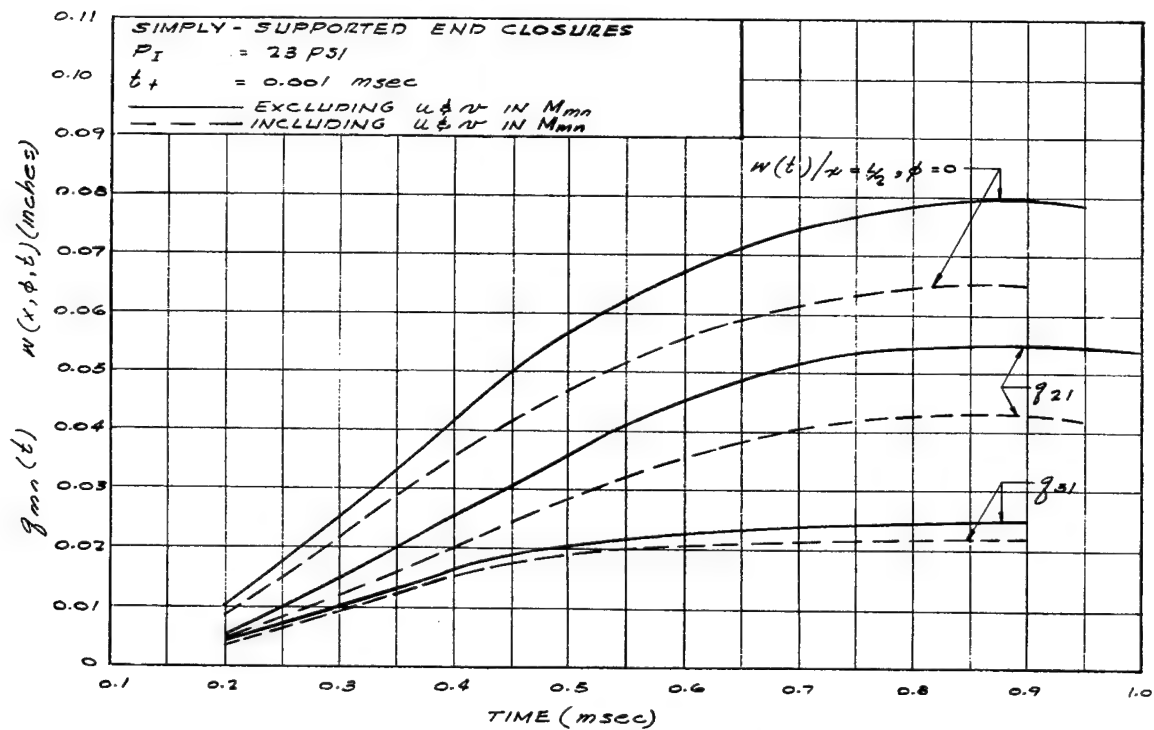


FIGURE 3.4. VARIATION OF  $q_{mn}(t)$  AND RADIAL DISPLACEMENT  $w(t)$   
 AT  $x = L/2, \phi = 0^\circ$  FOR CYLINDRICAL SHELL

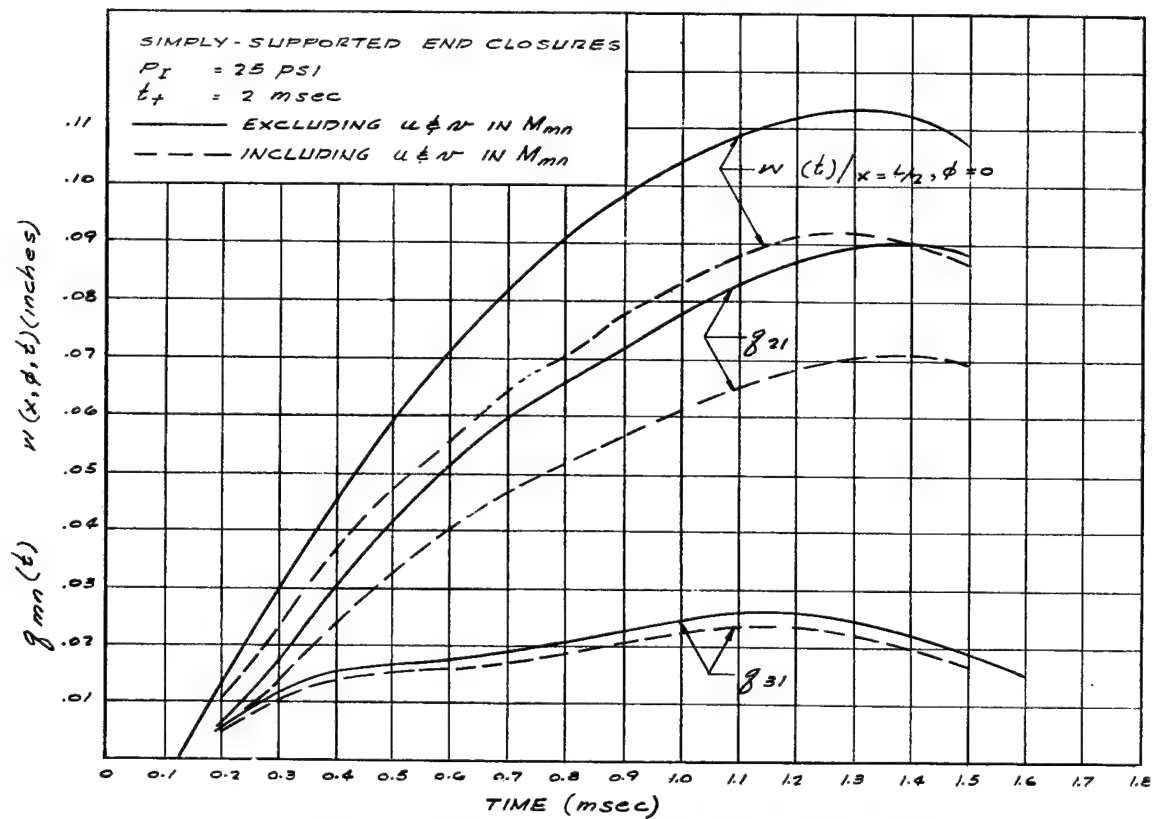


FIGURE 3.5. VARIATION OF  $q_{mn}(t)$  AND RADIAL DISPLACEMENT  $w(t)$   
 AT  $x = L/2, \phi = 0^\circ$  FOR CYLINDRICAL SHELL

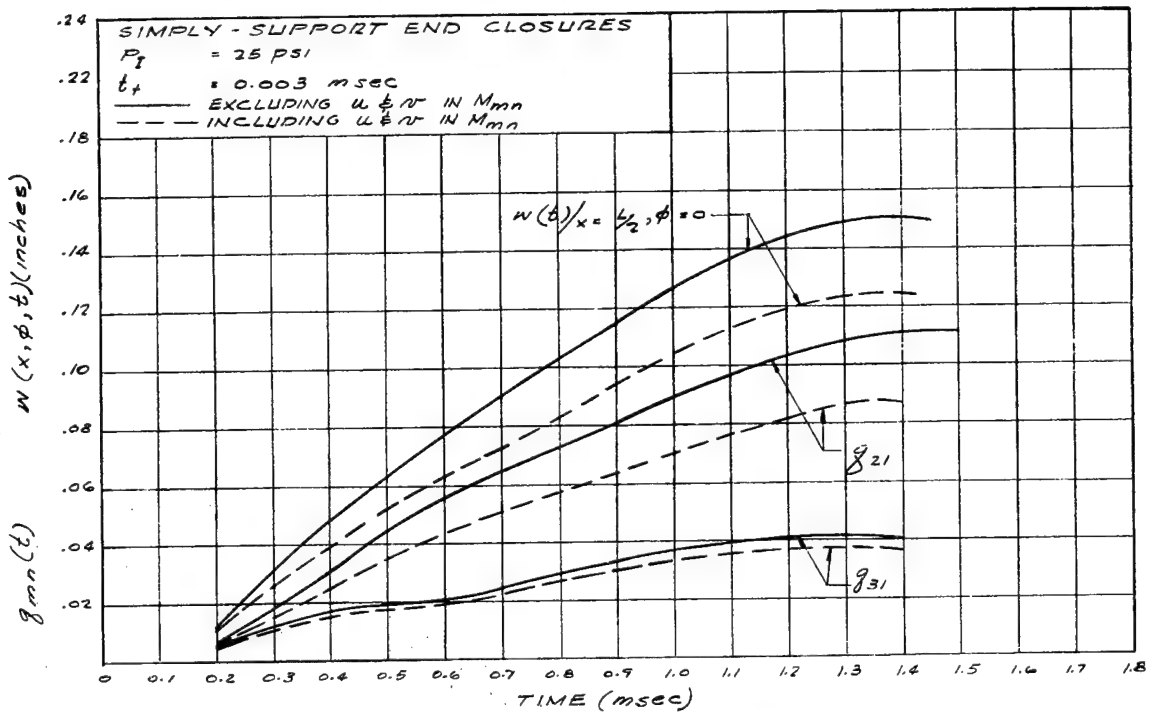


FIGURE 3.6. VARIATION OF  $q_{mn}(t)$  AND RADIAL DISPLACEMENT  $w(t)$  AT  $x = L/2, \phi = 0^\circ$  FOR CYLINDRICAL SHELL.

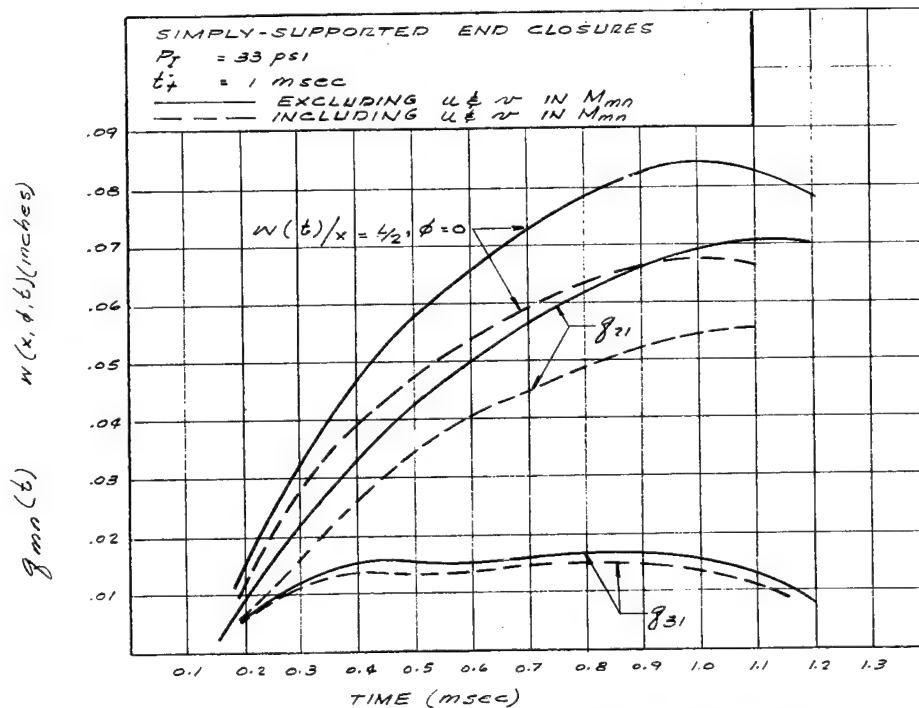


FIGURE 3.7. VARIATION OF  $q_{mn}(t)$  AND RADIAL DISPLACEMENT  $w(t)$  AT  $x = L/2, \phi = 0^\circ$  FOR CYLINDRICAL SHELL.

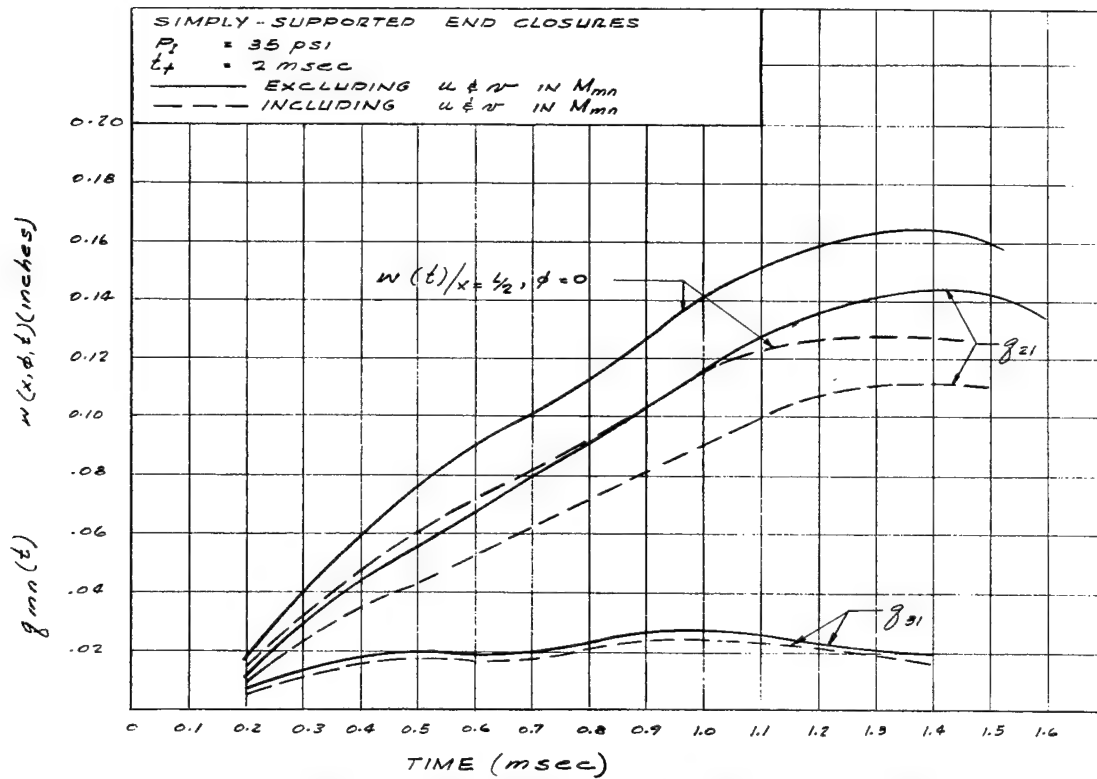


FIGURE 3.8 VARIATION OF  $q_{mn}(t)$  AND RADIAL DISPLACEMENT  $w(t)$   
 AT  $x = L/2, \phi = 0^\circ$  FOR CYLINDRICAL SHELL.

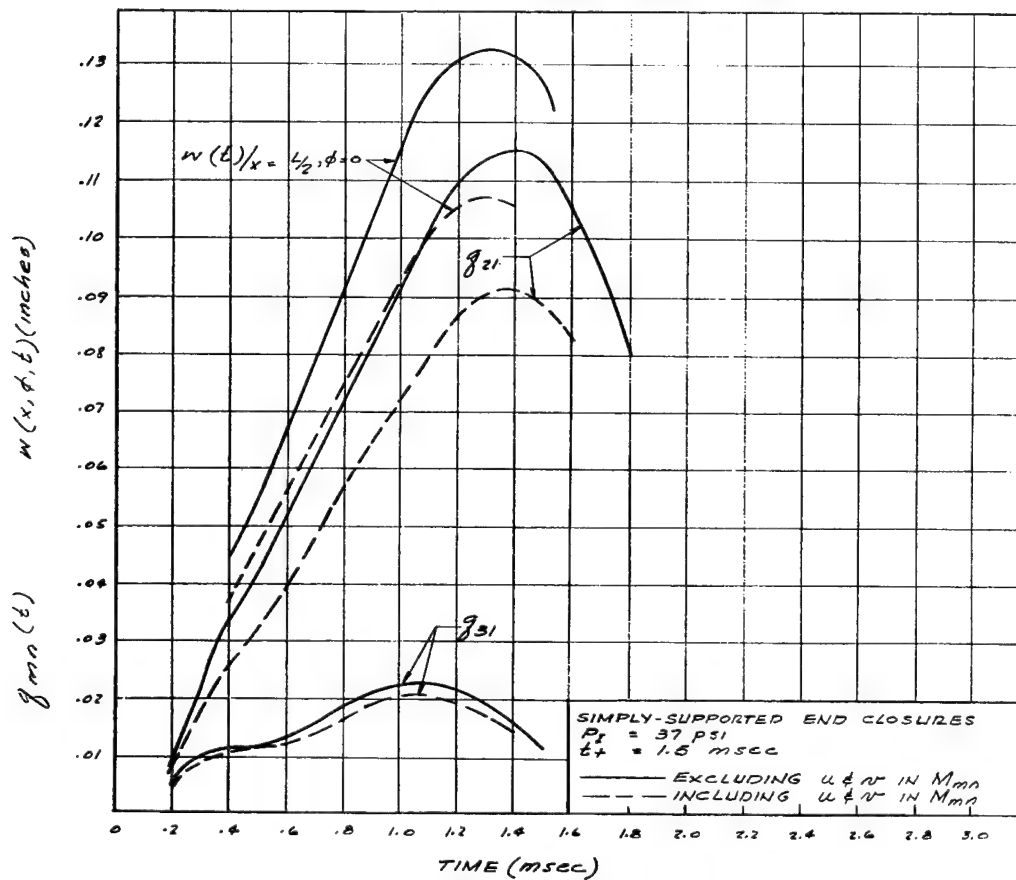


FIGURE 3.9 VARIATION OF  $q_{mn}(t)$  AND RADIAL DISPLACEMENT  $w(t)$   
 AT  $x = L/2, \phi = 0^\circ$  FOR CYLINDRICAL SHELL

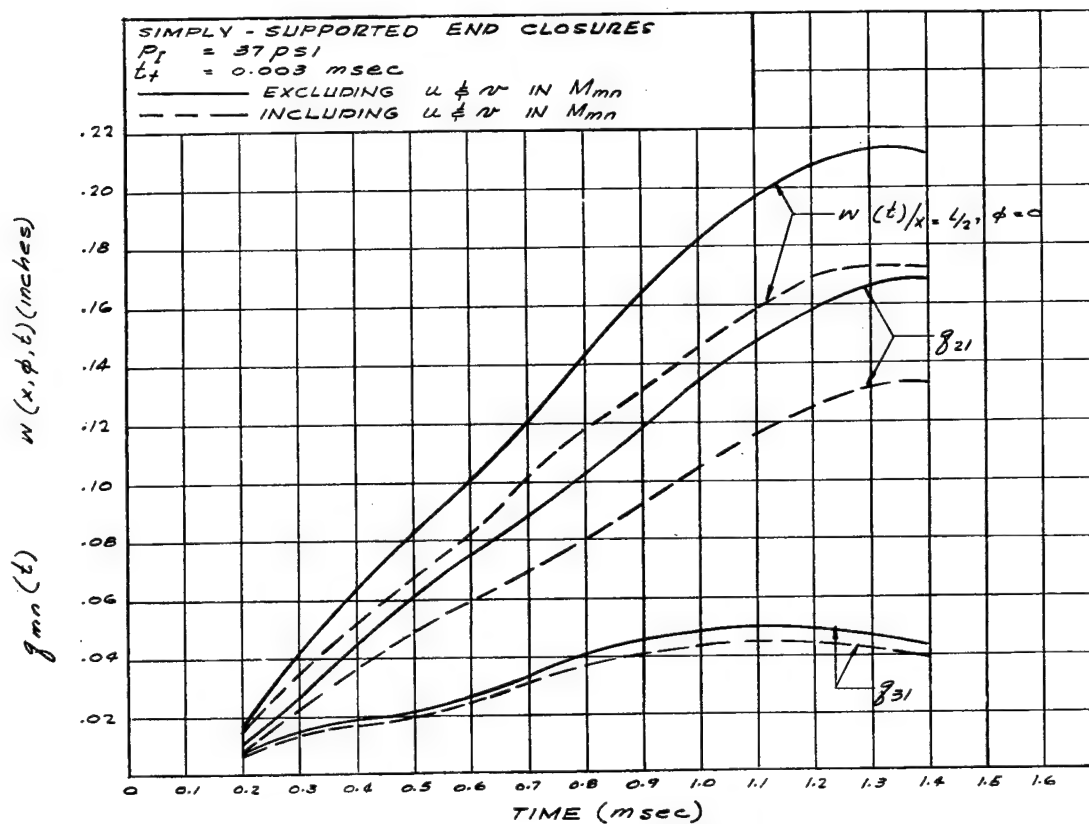


FIGURE 3. 10: VARIATION OF  $q_{mn}(t)$  AND RADIAL DISPLACEMENT  $w(t)$   
 AT  $x = L/2$ ,  $\phi = 0^\circ$  FOR CYLINDRICAL SHELL

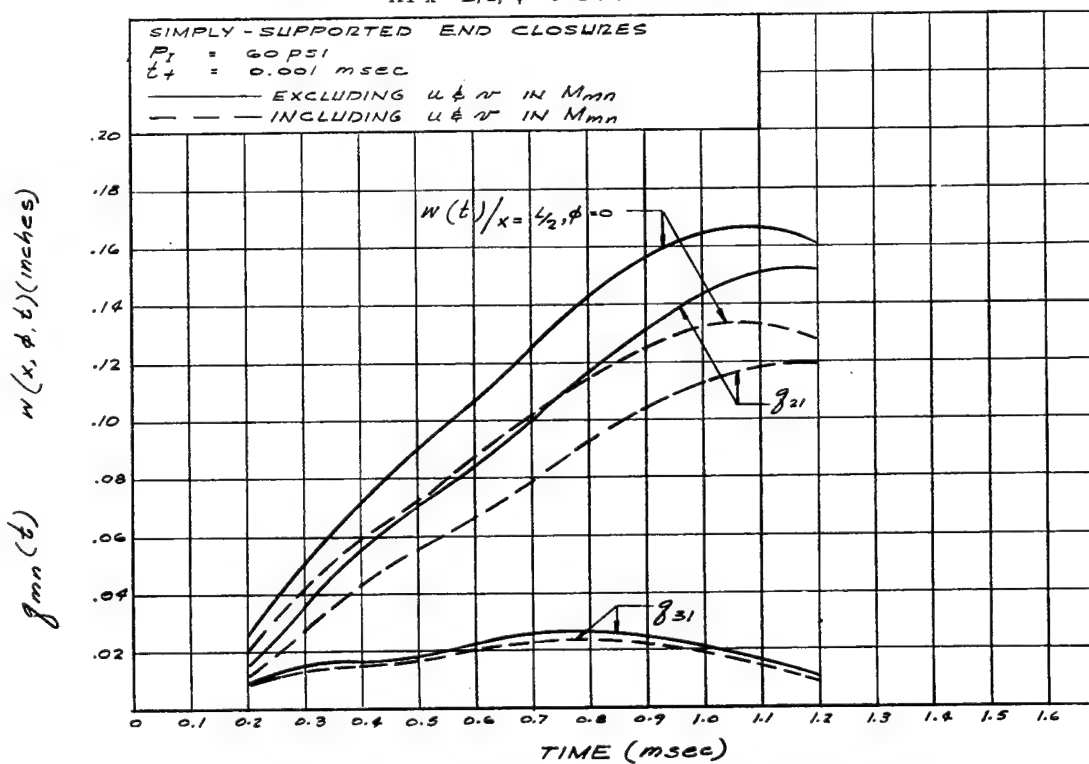


FIGURE 3. 11. VARIATION OF  $q_{mn}(t)$  AND RADIAL DISPLACEMENT  $w(t)$   
 AT  $x = L/2$ ,  $\phi = 0^\circ$  FOR CYLINDRICAL SHELL

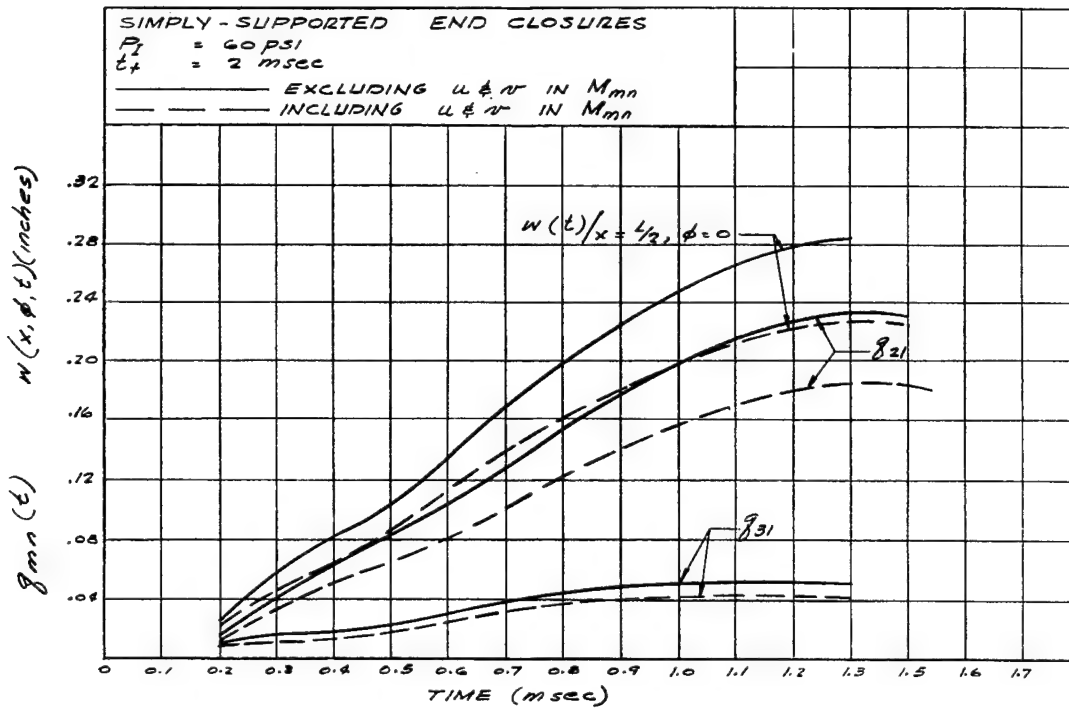


FIGURE 3.12. VARIATION OF  $q_{mn}(t)$  AND RADIAL DISPLACEMENT  $w(t)$   
 AT  $x = L/2$ ,  $\phi = 0^\circ$  FOR CYLINDRICAL SHELL

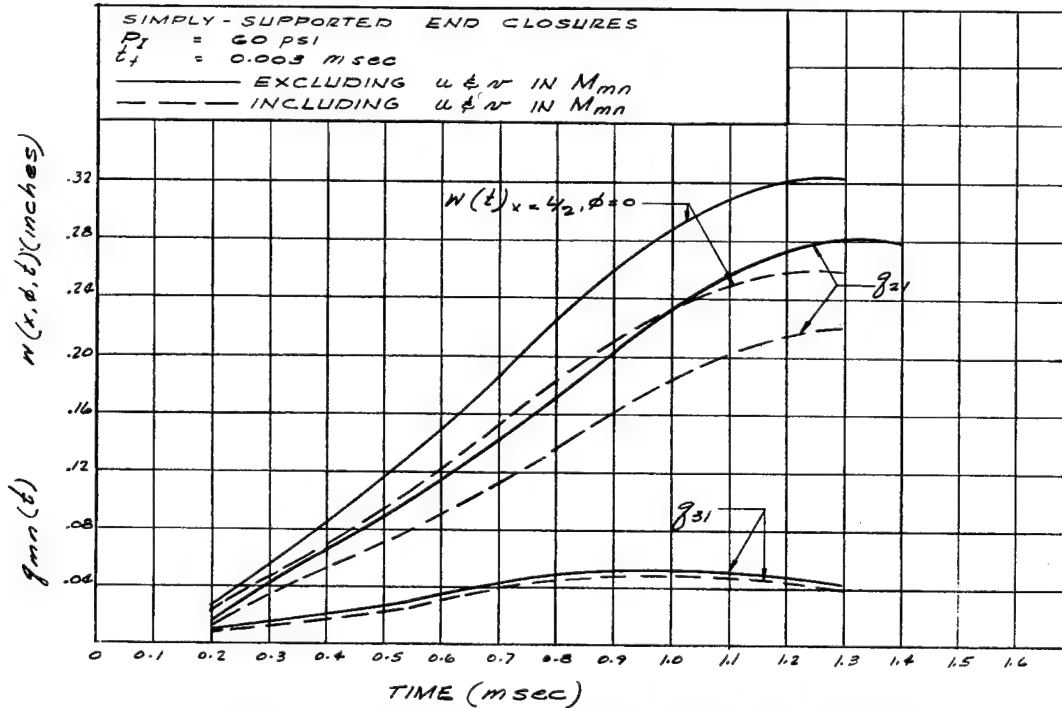


FIGURE 3.13. VARIATION OF  $q_{mn}(t)$  AND RADIAL DISPLACEMENT  $w(t)$   
 AT  $x = L/2$ ,  $\phi = 0^\circ$  FOR CYLINDRICAL SHELL

TABLE 3.2. COMPUTED MAXIMUM RADIAL DISPLACEMENTS (COLUMNS A) AND  
CORRESPONDING TIME OF OCCURENCE (COLUMNS B) AT  $x = L/2$ ,  $\phi = 0^\circ$   
FOR CYLINDERS WITH SIMPLY-SUPPORTED END-CLOSURES

$P_I$ (psi)	$t_+$ (msec)	Columns A		Columns B		$I$ lb-in <sup>2</sup> -msec (3)
		(1) (inches)	(2) (inches)	(1) (msec)	(2) (msec)	
17	0.75	.042	.035	0.9	0.85	6.3
17	2.5	.150	.085	1.4	1.4	21.2
23	1.0	.078	.065	0.9	0.9	11.5
25	2.0	.114	.092	1.3	1.3	25
25	3.0	.152	.124	1.4	1.4	37.5
33	1.0	.084	.067	1.0	1.0	16.5
35	2.0	.164	.128	1.4	1.3	35.0
37	1.5	.132	.107	1.3	1.3	27.7
37	3.0	.212	.174	1.3	1.3	55.5
60	1.0	.167	.133	1.0	1.0	30
60	2.0	.284	.184	1.4	1.4	60
60	3.0	.325	.26	1.3	1.2	90

(1) Neglecting contributions of  $u$  &  $v$  in  $M_{mn}$

(2) Including contributions of  $u$  &  $v$  in  $M_{mn}$

(3)  $P_I \times t_+ / 2$

$$\Gamma_2 = \sin \kappa + \sinh \kappa$$

$$\Gamma_3 = \cosh \kappa - \cos \kappa$$

$$\kappa = n'\pi$$

$$n' = 1/2(2n + 1) \quad (n = 1, 2, 3, \dots)$$

It is of interest to note that the integral term in Equation (3.8) is identical to that appearing in Equation (3.4). Thus, the values of the generalized force for the simple and fixed support conditions are proportional. The values of the terms in Equation (3.8) are given in Table 3.3.

For the generalized mass, in a first order approximation, the longitudinal and tangential components of the displacement were neglected [see Eq. (I.27), Appendix I], so that

$$M_{mn} = \rho a h \int_0^L \int_0^{2\pi} [w_{mn}(x, \phi)]^2 dx d\phi$$

or

$$M_{mn} = \frac{L h \rho a \pi C^2}{(\Gamma_1'')^2 \kappa} a_1(\kappa) \quad (3.9)$$

where

$$\begin{aligned} a_1(\kappa) = & \Gamma_3^2 \left( \frac{1}{2} \sinh \kappa \cosh \kappa + \kappa - \cosh \kappa \sin \kappa \right) \\ & - \Gamma_2 \Gamma_3 \left( \frac{1}{2} \cosh 2\kappa - 2 \sinh \kappa \sin \kappa - \frac{1}{2} \cos 2\kappa \right) \\ & + \Gamma_2^2 \left( \frac{1}{2} \sinh \kappa \cosh \kappa - \cosh \kappa \sin \kappa \right) \end{aligned}$$

The appropriate values of  $a_1(\kappa)$  are also given in Table 3.3

From Equations (3.8) and (3.9), we acquire the ratio necessary for the solution of Equation (I.28)

$$\frac{Q_{mn}(t)}{M_{mn}} = \frac{\Gamma_1''}{\rho h \pi C} \frac{\beta(\kappa)}{a_1(\kappa)} \sum \int_{\phi} P_{\phi}(t) \cos m\phi d\phi \quad \begin{matrix} (m = 2, 3, \dots) \\ (n = 1, 3, 5, \dots) \end{matrix} \quad (3.10)$$

where the summation is identical to the terms within the brackets in Equation (3.5). The variation of  $q_{mn}(t)$  with time, obtained by utilizing Equation (3.10) in Equation (I.28) are shown in Figures 3.14 through 3.19. The variation of the radial displacement with time (also shown in Figs. 3.14 through 3.19) are obtained from Equation (3.2), or, for the fixed boundary conditions

$$w(x, \phi, t) = \frac{C}{\Gamma_1''} \sum \left[ \Gamma_3 \left( \cos \frac{\kappa x}{L} - \cosh \frac{\kappa x}{L} \right) + \Gamma_2 \left( \sinh \frac{\kappa x}{L} - \sin \frac{\kappa x}{L} \right) \right] \cos m\phi q(t) \quad (3.12)$$

Table 3.4 contains the maximum radial displacement and corresponding times.

In order to determine the contributions of the longitudinal (u) and tangential (v) components of displacements, we use the expression for generalized mass appearing in Equation (I.27) and from Equations (2.11) and (2.12) obtain

TABLE 3.3. FREQUENCIES AND RELATED QUANTITIES FOR  
CYLINDRICAL SHELLS WITH FIXED END-CLOSURES

$m$	$n$	$n'$	$\omega_{mn}$ (rad/sec)	$f_{mn}$ cycle/sec	$\beta(\kappa)^{(1)}$	$a_1(\kappa)^{(2)}$	$a_2(\kappa)^{(4)}$	$\frac{K_2^{(4)}}{K_1}$	$\frac{K_3\kappa^{(4)}}{K_1 L}$	(5)
1	1	1.5	50,000	7,960	220	25,600	11,170	-.9684	.4525	51895
1	2	2.5 <sup>(3)</sup>			1.0	$25 \times 10^6$	0	-.8266	.6167	
1	3	3.5	56,310	8,960	120,000	$9.7 \times 10^{11}$	$264.8 \times 10^{11}$	-.6338	.6172	
2	1	1.5	4,640	740	220	25,600	11,170	.5022	.2007	32506
2	2	2.5 <sup>(3)</sup>	13,660	2,180	1.0	$25 \times 10^6$	0			
2	3	3.5	79,730	12,700	120,000	$9.7 \times 10^{11}$	$264.8 \times 10^{11}$			
3	1	1.5	2,040	325	220	25,600	11,170	.3335	.0874	28530
3	2	2.5 <sup>(3)</sup>	6,010	960	1.0	$25 \times 10^6$	0			
3	3	3.5	12,050	1,920	120,000	$9.7 \times 10^{11}$	$264.8 \times 10^{11}$			

(1) See Eq. 3.8

(2) See Eq. 3.9

(3) Antisymmetrical

(4) See Eq. 3.13

$$(5) a_1(\kappa) \left[ 1 + \left( \frac{K_2}{K_1} \right)^2 \right] + a_2(\kappa) \left( \frac{K_3\kappa}{K_1 L} \right)^2$$

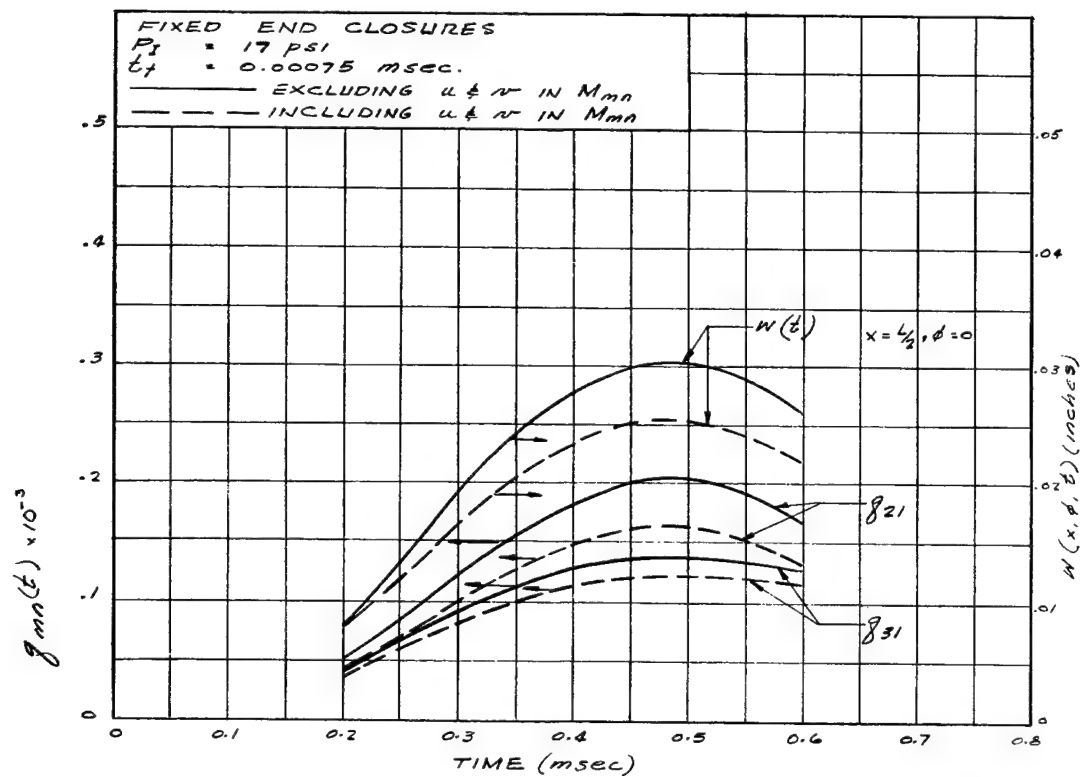


FIGURE 3. 14. VARIATION OF  $q_{mn}(t)$  AND RADIAL DISPLACEMENT  $w(t)$   
 AT  $x = L/2$ ,  $\phi = 0^\circ$  FOR CYLINDRICAL SHELL

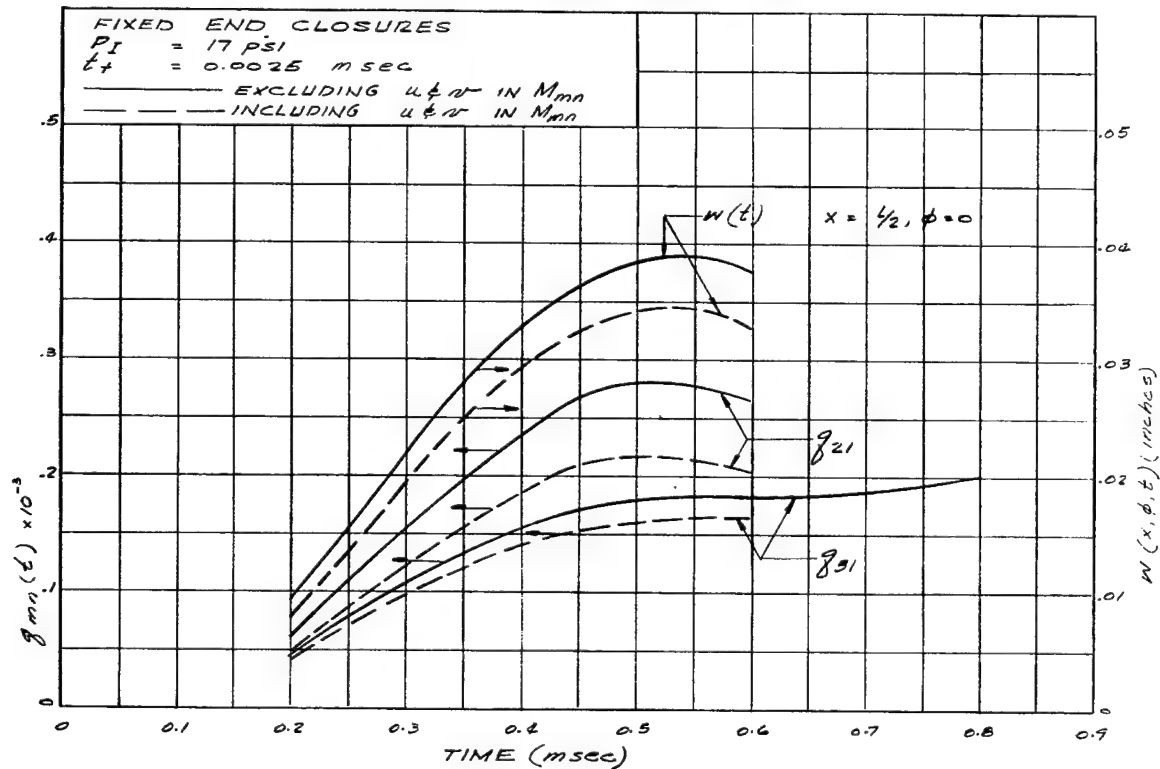


FIGURE 3. 15. VARIATION OF  $q_{mn}(t)$  AND RADIAL DISPLACEMENT  $w(t)$   
 AT  $x = L/2$ ,  $\phi = 0^\circ$  FOR CYLINDRICAL SHELL

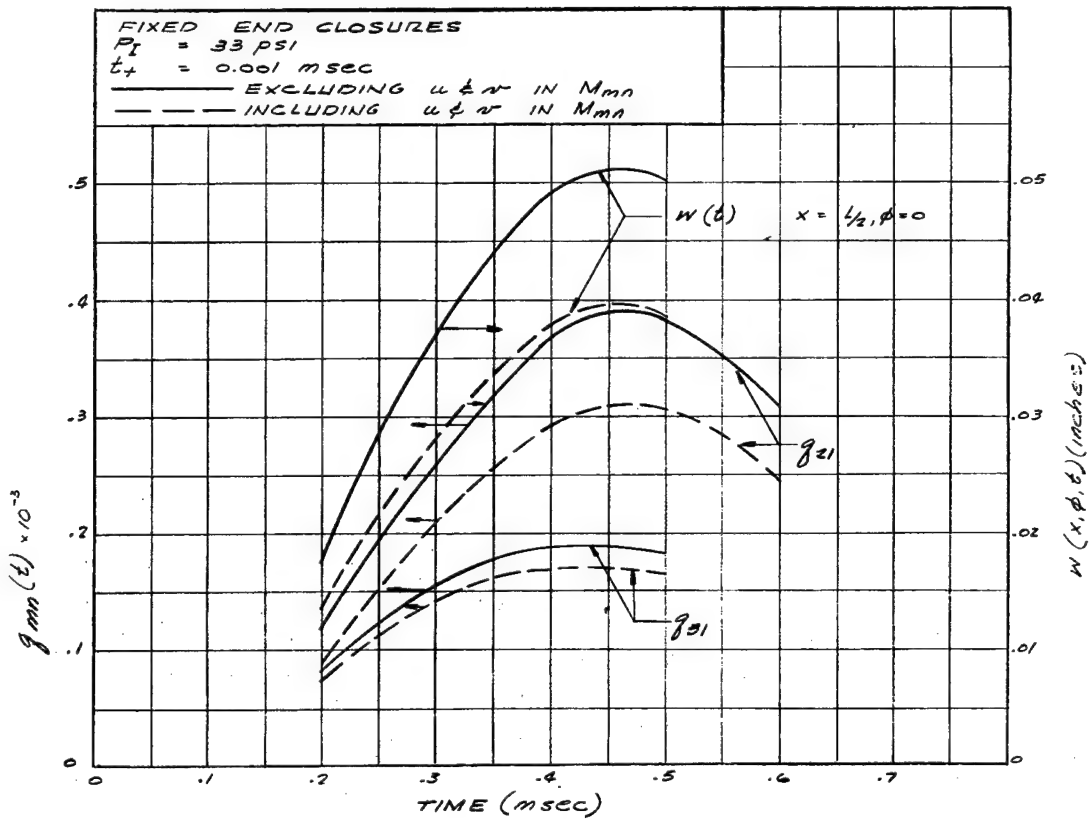


FIGURE 3. 16. VARIATION OF  $q_{mn}(t)$  AND RADIAL DISPLACEMENT  $w(t)$   
 AT  $x = L/2, \phi = 0^\circ$  FOR CYLINDRICAL SHELL

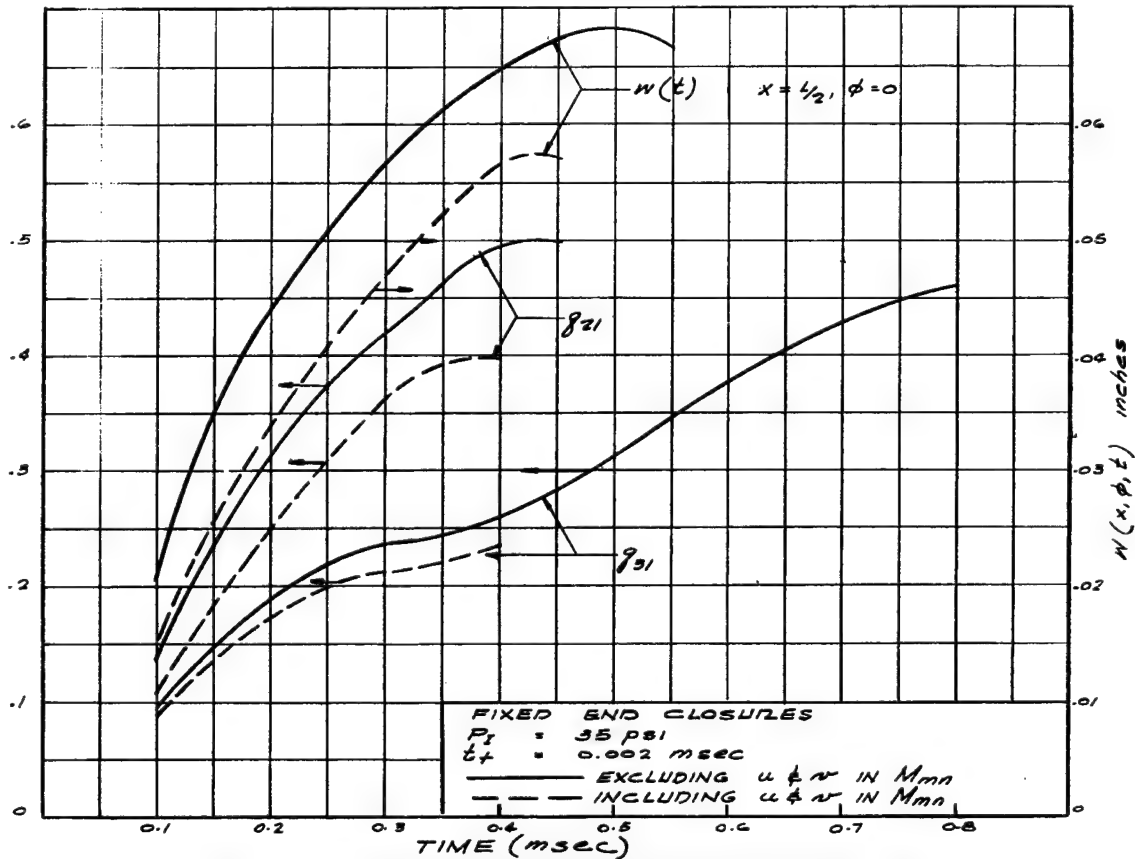


FIGURE 3. 17. VARIATION OF  $q_{mn}(t)$  AND RADIAL DISPLACEMENT  $w(t)$   
 AT  $x = L/2, \phi = 0^\circ$  FOR CYLINDRICAL SHELL

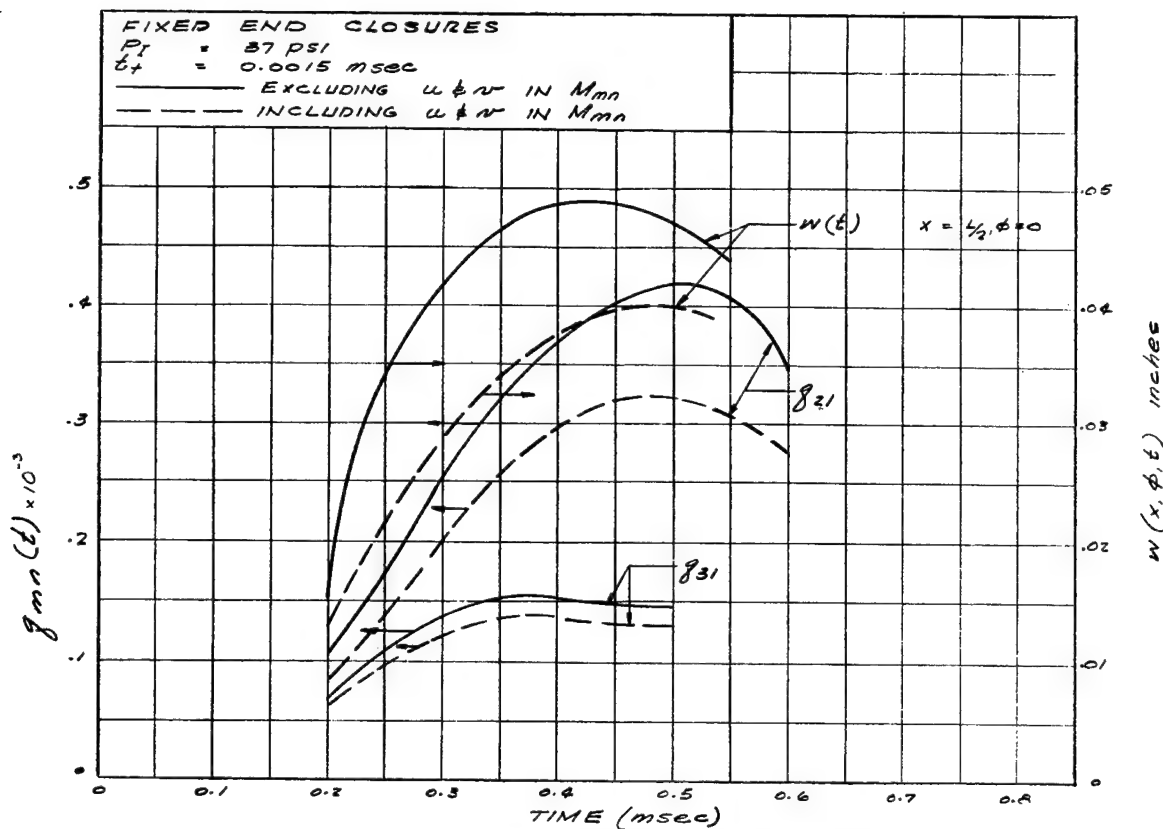


FIGURE 3. 18. VARIATION OF  $q_{mn}(t)$  AND RADIAL DISPLACEMENT  $w(t)$  AT  $x = L/2, \phi = 0^\circ$  FOR CYLINDRICAL SHELL

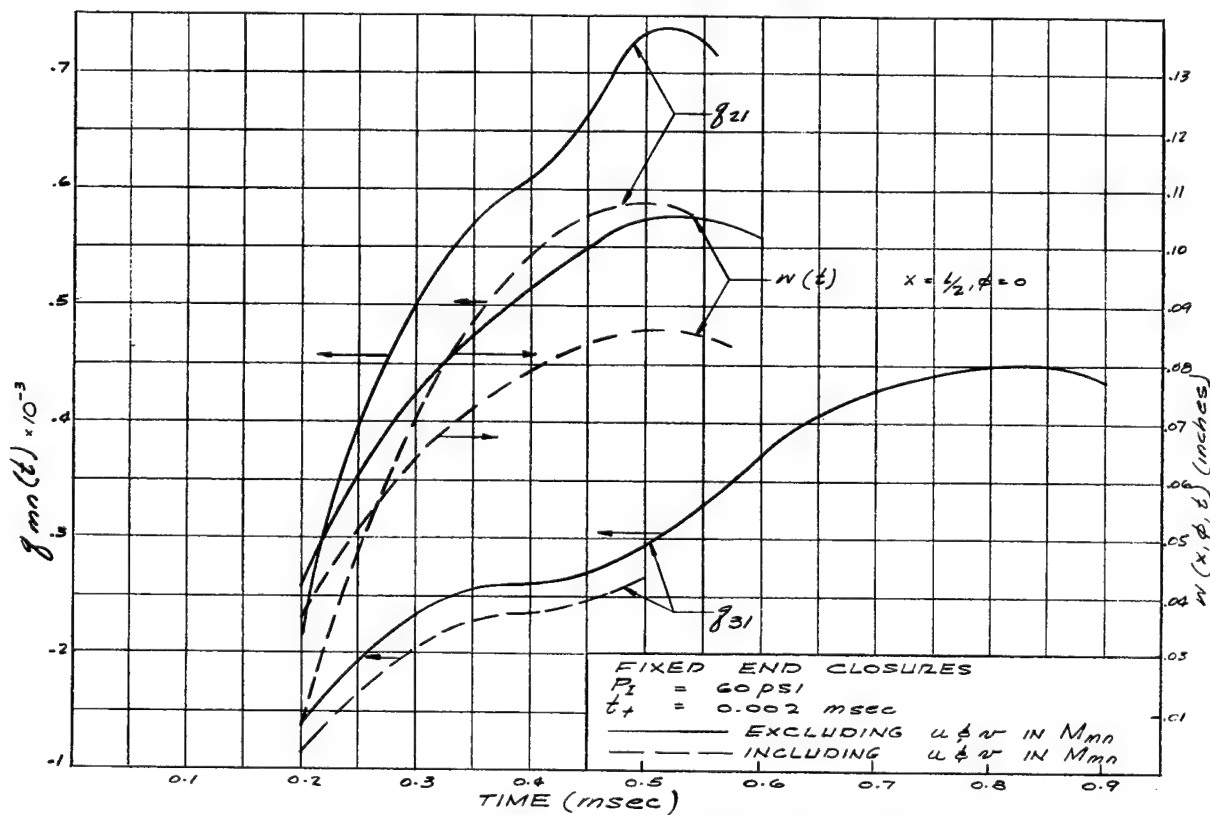


FIGURE 3. 19. VARIATION OF  $q_{mn}(t)$  AND RADIAL DISPLACEMENT  $w(t)$  AT  $x = L/2, \phi = 0^\circ$  FOR CYLINDRICAL SHELL

TABLE 3.4. COMPUTED MAXIMUM RADIAL DISPLACEMENTS (COLUMNS A) AND  
CORRESPONDING TIME OF OCCURENCE (COLUMNS B) AT  $x = L/2$ ,  $\phi = 0^\circ$   
FOR CYLINDERS WITH FIXED END-CLOSURES

$P_I$ (psi)	$t_+$ (msec)	Columns A		Columns B		I (3) (lb-in <sup>2</sup> -msec)
		(1) (inches)	(2) (inches)	(1) (msec)	(2) (msec)	
17	0.75	.030	.025	0.49	0.47	6.3
17	2.5	.039	.035	0.54	0.54	21.2
33	1.0	.051	.040	0.46	0.46	16.5
35	2.0	.068	.057	0.60	0.53	17.5
37	1.5	.049	.040	0.43	0.48	27.7
60	2.0	.093	.076	0.53	0.53	60

(1) Neglecting contributions of  $u$  and  $v$  in  $M_{mn}$

(2) Including contributions of  $u$  and  $v$  in  $M_{mn}$

(3)  $\frac{(P_I)(t_+)}{2}$

$$M_{mn} = \frac{L h \rho a \pi C^2}{(\Gamma_1'')^2 \kappa} \left\{ a_1(\kappa) \left[ 1 + \left( \frac{K_2}{K_1} \right)^2 \right] + a_2(\kappa) \left( \frac{K_3 \kappa}{K_1 L} \right)^2 \right\} \quad (3.13)$$

where

$$a_2(\kappa) = \Gamma_3^2 \left( \frac{1}{2} \sinh \kappa \cosh \kappa + \cosh \kappa \sin \kappa \right) - \frac{1}{2} \Gamma_2 \Gamma_3 (\cosh 2\kappa + \cos 2\kappa) \\ + \Gamma_2^2 \left( \frac{1}{2} \sinh \kappa \cosh \kappa + \kappa - \cosh \kappa \sin \kappa \right)$$

Accordingly, Equation (3.10) is replaced by

$$\frac{Q_{mn}(t)}{M_{mn}} = \frac{\Gamma_1''}{\rho h \pi C} \frac{\beta(\kappa) \sum_{\phi} \int P_{\phi}(t) \cos m\phi d\phi}{a_1(\kappa) \left[ 1 + \left( \frac{K_2}{K_1} \right)^2 \right] + a_2(\kappa) \left( \frac{K_3 \kappa}{K_1 L} \right)^2} \quad (3.14)$$

The corresponding values for  $q_{mn}(t)$  obtained from Equation (I.28) and  $w(t)$  at  $x = L/2$  and  $\phi = 0^\circ$  are given in Figures 3.14 through 3.19.

### 3.3 Elastic End-Closures

For cylinders with flexible, flat-plate, end-closures, we take as a first order approximation the following relation for the moment

$$\frac{\bar{M}}{\bar{D}} = \frac{d\phi}{d\bar{r}} + \bar{\nu} \frac{\phi}{\bar{r}} \quad (3.15)$$

where the bar denotes properties associated with the plate. The solution of Equation (3.15) for  $\phi$  is

$$\phi = \frac{\bar{M}}{\bar{D}} \frac{\bar{r}}{\bar{\nu} + 1}$$

Setting the value of  $\phi$  at  $\bar{r} = \bar{a}$  equal to one radian, the value of stiffness  $S$  is found by

$$S = \frac{\bar{D}(1 + \bar{\nu})}{\bar{a}} \quad (\text{for } \phi \Big|_{\bar{a}} = 1 \text{ radian})$$

If the flat plate has the same thickness as the cylinder wall and is made of the same material as the shell, then using the specific dimensional and materials values previously listed, we have for this particular case

$$S = 28.2$$

and thus

$$R = \frac{SL}{D} \cong 8$$

For a load uniformly distributed along the length of the shell, the expression for the generalized mass is

$$Q_{mn}(t) = \frac{LaC}{\Gamma_1' \kappa} \beta(\kappa, R) \int_0^{2\pi} P(\phi, t) \cos m\phi d\phi \quad (3.16)$$

where

$$\beta(\kappa, R) = 2 \left\{ \kappa^2 [\sin \kappa (\cosh \kappa - 1) + \sinh \kappa (1 - \cos \kappa) + R\kappa (\cosh \kappa \cos \kappa - 1) + R^2 [\sin \kappa (\cosh \kappa - 1) - \sinh \kappa (1 - \cos \kappa)]] \right\}$$

$$\begin{aligned} \Gamma_1' &= 2\kappa^2 \sin \kappa + R(\kappa + R)(\sinh \kappa - \cosh \kappa + \sin \kappa + \cos \kappa) \\ &= 2\kappa^2 \sin \kappa + R(\kappa + R) \Gamma_1'' \quad [\text{See Eq. (3.8)}] \end{aligned}$$

$$\Gamma_2 = \sin \kappa + \sinh \kappa$$

$$\Gamma_3 = \cosh \kappa - \cos \kappa$$

and  $\kappa$  are the values commensurate with the value of  $R$  obtained from Figure 2.1. These values of  $\kappa$  and the circular frequencies obtained from Figure 3.20 are given in Table 3.5.

For the generalized mass, neglecting the contributions of the longitudinal and transverse components of displacements, we have

$$M_{mn} = \frac{Lh\rho\pi C^2}{(\Gamma_1')^2 \kappa} a_1(\kappa, R) \quad (3.17)$$

where

$$\begin{aligned} a_1(\kappa, R) &= 2\kappa^5 \Gamma_2 (\sinh \kappa - \sin \kappa) + 2\kappa^4 [3 \sinh \kappa \sin \kappa (\cosh \kappa \sin \kappa - \sinh \kappa \cos \kappa) \\ &\quad - R\Gamma_3 (\sinh \kappa - \sin \kappa)] + \kappa^3 R [4 \sinh \kappa \sin \kappa (\cosh \kappa \cos \kappa - 1) - R\Gamma_2^2] \\ &\quad + \kappa^2 R^2 [(\cosh \kappa \cos \kappa - 1)(\sinh \kappa \cos \kappa - \cosh \kappa \sin \kappa) + 8 \sinh \kappa \sin \kappa (\sinh \kappa \cos \kappa \\ &\quad + \cosh \kappa \sin \kappa) + 2\Gamma_2 \Gamma_3] + \kappa R^3 [R\Gamma_3^2 + 4 (\cosh \kappa \cos \kappa - 1)^2] \\ &\quad + 3R^4 (\cosh \kappa \cos \kappa - 1)(\cosh \kappa \sin \kappa + \sinh \kappa \cos \kappa) \end{aligned}$$

From Equations (3.16) and (3.17), the necessary ratio for the solution of Equation (I.28) is as follows

$$\frac{Q_{mn}(t)}{M_{mn}} = \frac{\Gamma_1'}{\rho h \pi C} \frac{\beta(\kappa, R)}{a_1(\kappa, R)} \sum_{\phi} \int P_{\phi}(t) \cos m\phi d\phi \quad (3.18)$$

where the summation is identical to the terms within the brackets in Equation (3.5). The variation of  $w(x, \phi, t)$  at  $x = L/2$ , and  $\phi = 0^\circ$  with time is shown in Figures 3.21 through 3.23.

TABLE 3.5. FREQUENCIES AND RELATED QUANTITIES FOR  
CYLINDERS WITH ELASTIC END-CLOSURES

<u>m</u>	<u>n</u>	<u><math>\kappa</math></u>	<u><math>\omega_{mn}</math></u> (rad/sec)	<u><math>\beta(\kappa, R)^{(1)}</math></u>	<u><math>\alpha_1(\kappa, R)^{(2)}</math></u>
2	1	$1.41\pi$	4,000	12,200	$56.49 \times 10^6$
3	1	$1.41\pi$	2,100	12,200	$56.49 \times 10^6$

(1) See Equation (3.16) (for  $R = 8$ )

(2) See Equation (3.17) (for  $R = 8$ )

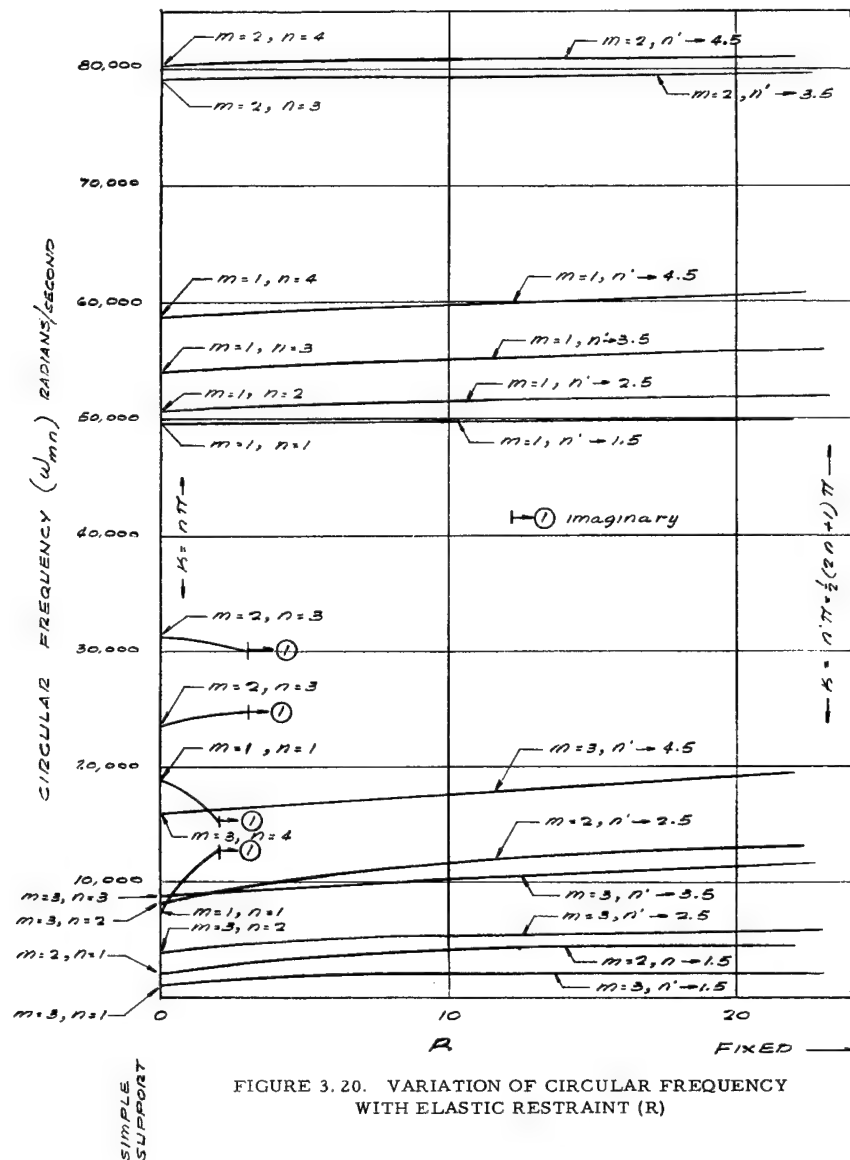


FIGURE 3.20. VARIATION OF CIRCULAR FREQUENCY WITH ELASTIC RESTRAINT (R)

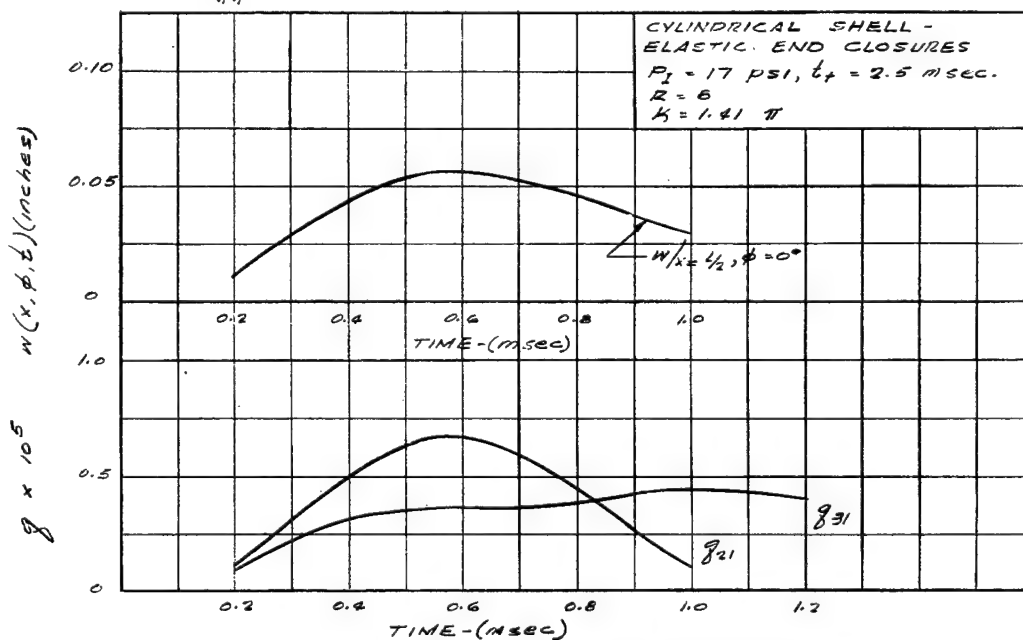


FIGURE 3.21. VARIATION OF  $q_{mn}(t)$  AND RADIAL DISPLACEMENT  $w(t)$  AT  $x = L/2$ ,  $\phi = 0^\circ$  FOR CYLINDRICAL SHELL

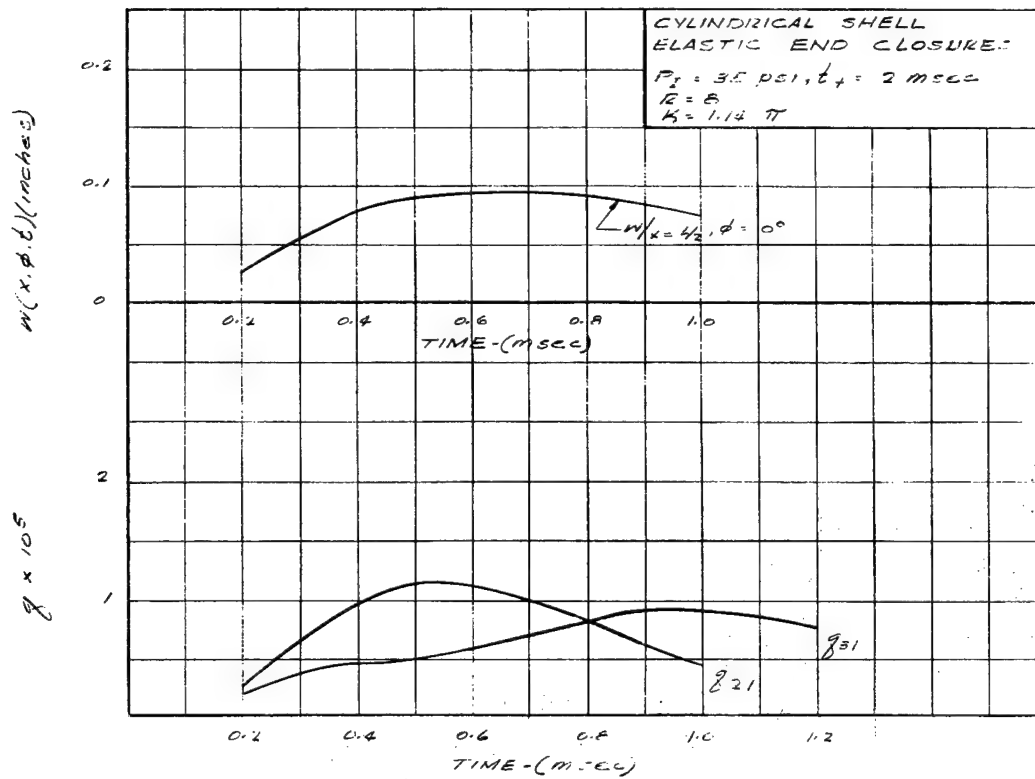


FIGURE 3.22. VARIATION OF  $q_{mn}(t)$  AND RADIAL DISPLACEMENT  $w(t)$   
AT  $x = L/2, \phi = 0^\circ$  FOR CYLINDRICAL SHELL

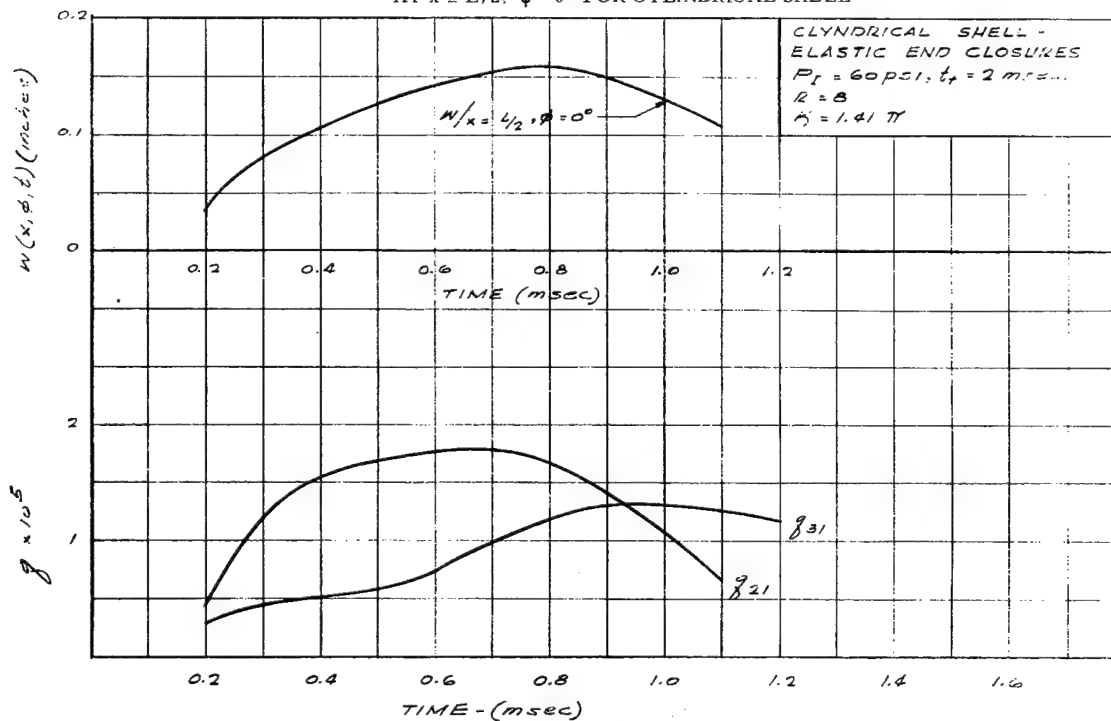


FIGURE 3.23. VARIATION OF  $q_{mn}(t)$  AND RADIAL DISPLACEMENT  $w(t)$   
AT  $x = L/2, \phi = 0^\circ$  FOR CYLINDRICAL SHELL

#### 4. DISCUSSION

The utility of an analytical procedure is best measured in terms of its ability to yield meaningful and correlative quantities for a wide range of variables with a minimum of computational effort. The adequacy of these computed quantities can be ascertained only in a direct comparison with reliable, equivalent experimental evidence. If the results obtained by a comparatively simple analytical method agree favorably with the available experimental data and if the results cover the range of interest for the problem at hand, there then appears to be little reason (at least from a practical viewpoint) for employing another more rigorous and therefore more computationally complex solution.

The linear-elastic method for cylindrical shells developed in Section 2.1.1 and used in the numerical analysis in Section 3 appears to yield significant results (over a wide range of peak overpressures and positive phase durations) that agree favorably with the experimental data. There is, at present, no apparent or justifiable reason for suggesting the use of other available but nevertheless more complex analytical procedures (such as that developed in Section 2.1.2).

One method of compactly presenting the numerical results obtained in the preceding section is to chart the variation of the maximum radial displacement (in this case, at  $x = L/2$ , and  $\phi = 0^\circ$ ) with the two characteristics which distinguish each particular blast loading, namely, the peak incident overpressure ( $P_I$ ) and the companion positive phase duration ( $t_+$ ). In Figure 4.1, we have taken the impulse (defined as  $P_I \times t_+ \div 2$ ) for the ordinate axis and the maximum radial deflection for the abscissa. On one hand, the bands for each type of cylinder end-closure arise from taking the generalized mass as a function of only the radial component of displacement and on the other including all three displacement components ( $u, v$  and  $w$ ) in computing  $M_{mn}$ . In Table 4.1 are comparisons of high-speed camera data obtained for specific models with the computational results as represented in Tables 3.2 and 3.4 or Figure 4.1.

The close agreement between the experimental and analytical results is indeed encouraging particularly in view of some of the expected deviations in the peak incident overpressure and positive phase duration that arise from minor differences in charge size and shape, differences in atmospheric conditions and local changes at ground zero resulting from repeated shots. Moreover, there are the assumptions used in developing the load spectrums and the purely analytical approximations (see Appendix I) and some of the normal uncertainties associated with the high speed photography data (see Appendix III) and the models' dimensional and materials properties. All these factors undoubtedly contribute to the development of a range of displacement values rather than a precise and specific value for each given set of conditions. The encouraging aspect is that the numerical procedure used in the preceding section, which is comparatively simple and straightforward, does give values that are compatible with the experimental evidence and, therefore, of direct practical importance.

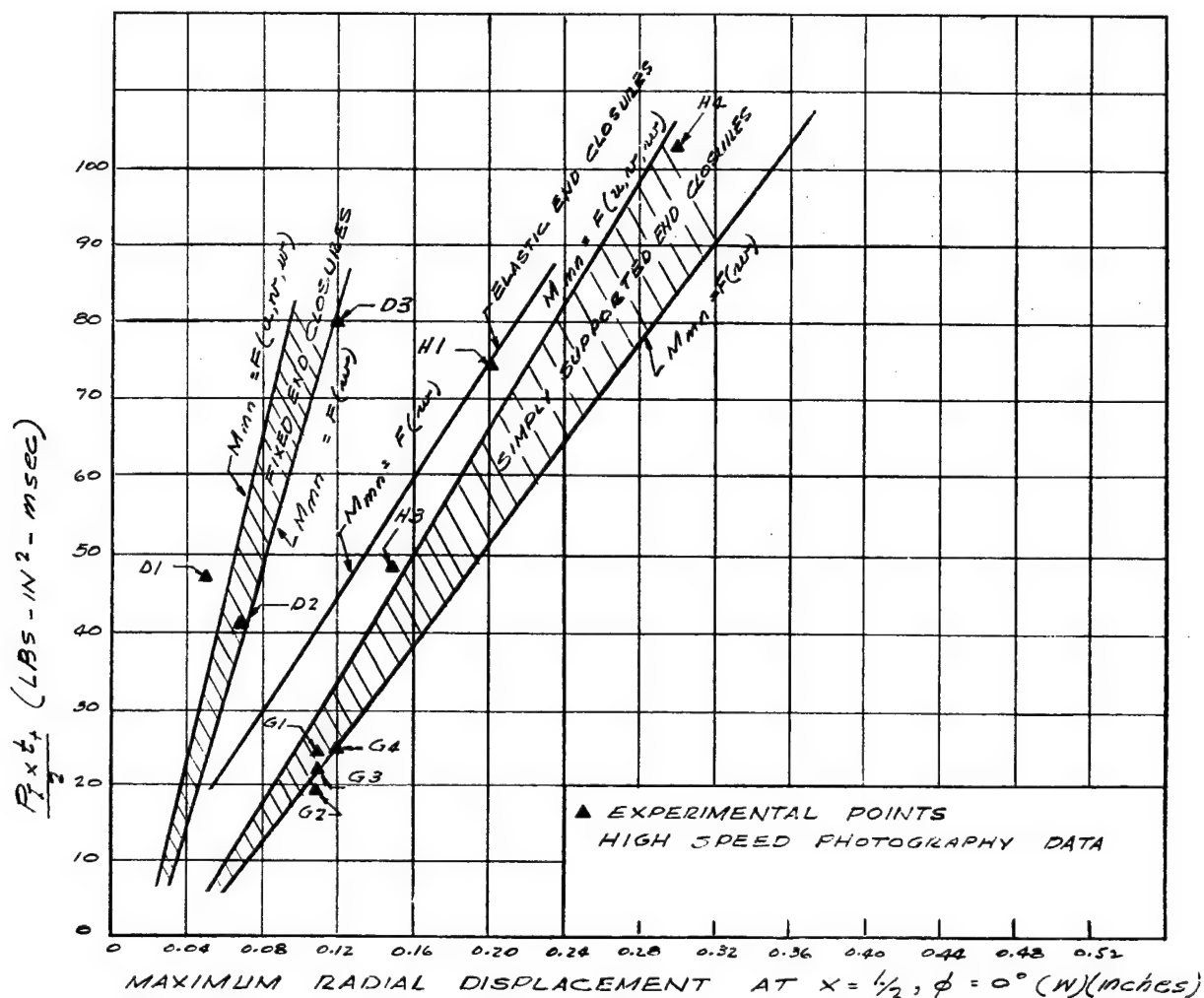


FIGURE 4.1. VARIATION OF MAXIMUM RADIAL DISPLACEMENT WITH ONE HALF OF PRODUCT OF PEAK INCIDENT OVERPRESSURE AND POSITIVE PHASE DURATION .

TABLE 4.1. COMPARISON OF EXPERIMENTAL (HIGH-SPEED PHOTOGRAPHY)  
AND COMPUTED (LINEAR-ELASTIC, SMALL DEFLECTION THEORY)  
RADIAL DISPLACEMENTS FOR CYLINDRICAL SHELLS

Model No.	Shot No.	Boundary Restraint	$P_I$ (psi)	$t_+$ (msec)	$(P_I \times t_+)/2$ (lb - in <sup>2</sup> - msec)	Computed		Experimental <sup>(9)</sup>	
						(5) (inches)	(6) (msec)	(5) (inches)	(6) (msec)
CA3	D1	Fixed	15 (2)	6.3 (4)	47	.064 - .078 (7)	-	.04	0.7
CA3	D2	"	19 (2)	5.5 (4)	41	.060 - .072 (7)	-	.07	1.5
CA3	D3	"	42 (2)	3.8 (4)	80	.098 - .118 (7)	-	.12	0.8
CB2	G1	s. s.	20 (1)	2.4 (3)	24	.084 - .116 (7)	1.4 (10)	.12	1.3
CB2	G2	"	16 (1)	2.3 (3)	19	.072 - .095 (7)	1.4 (10)	.11	1.5
CB2	G3	"	17 (1)	2.5 (3)	21.5	.085 - .105 (8)	1.4 (8)	.11	1.4
CB2	G4	"	17 (2)	2.9 (3)	24.5	.088 - .118 (7)	1.4 (10)	.13	1.3
CB2	H1	"	25 (2)	5.1 (3)	64	.194 - .248 (7)	-	.20	2.0
CB3	H3	"	23 (1)	4.5 (3)	52	.164 - .216 (7)	-	.15	1.5
CB3	H4	"	53 (1)	3.9 (3)	100	.284 - .366 (8)	1.4 (8)	.30	2.0

- 
- (1) From Table III. 1, Appendix III  
(2) From Figure III. 3, Appendix III  
(3) From Table III. 2, Appendix III  
(4) Computed  
(5) Maximum (inward) radial displacement at  $x = L/2$ ,  $\phi = 0^\circ$   
(6) Time of occurrence of displacement  
(7) From Figure 4. 1  
(8) From Table 3. 2 or computed  
(9) From Figures III. 4 through III. 13, Appendix III  
(10) Estimates

# APPENDIX I

## METHODS OF ANALYSIS (LINEAR-ELASTIC, SMALL DEFLECTION THEORY)

### LIST OF SYMBOLS

A, B, C		Constant coefficients (maximum amplitudes of component vibrations)
D	=	$\frac{Eh^3}{12(1 - \nu^2)}$
E		Elastic modulus
F	=	$\frac{\rho a^2(1 - \nu^2)}{E}$
K	=	$\frac{Eh}{1 - \nu^2}$
L		Cylinder length
M		Bending moment of section
$M_{mn}$		Generalized mass
N		Stress resultant
$Q_{mn}$		Generalized force
T		Kinetic energy
V		Potential (strain) energy
a		Mean cylinder radius
h		Cylinder wall thickness
i	=	$\sqrt{-1}$
j		Subscript
k	=	$\frac{h^2}{12a^2}$
m		Number of circumferential waves
q		Generalized coordinate
s	=	$a\phi$
t		Time
u, v, w		Longitudinal, tangential and radial components of displacements
x, $\phi$ , z		Axial, tangential, and radial coordinates

# LIST OF SYMBOLS (Cont'd)

$\alpha$	=	$\lambda/L$
$\gamma$		Shear strain
$\epsilon$		Axial strain
$\nu$		Poisson's ratio
$\rho$		Density $\left( \frac{\text{lb-sec}^2}{\text{in}^4} \right)$
$\psi$	=	$\frac{1 - \nu^2}{E} \rho \omega^2 a^2$
$\omega$		Circular frequency

## 1.1 FREQUENCY AND DISPLACEMENT EQUATIONS

The development of the necessary free-vibration equations follows the format established by Yu. (I. 1) The solution begins with the following equations of motion (I. 2) based on the assumption that  $N_{\phi r} = N_{xr} \approx 0$ . (See Figs. I. 1 and I. 2 for notation.)

$$\left. \begin{aligned} a \frac{\partial N_{xx}}{\partial x} + \frac{\partial N_{\phi x}}{\partial \phi} - \rho a h \ddot{u} &= 0 \\ a \frac{\partial N_{x\phi}}{\partial x} + \frac{\partial N_{\phi\phi}}{\partial \phi} + \rho a h \ddot{v} &= 0 \\ a \frac{\partial^2 M_{x\phi}}{\partial x^2} + \frac{\partial^2 M_{\phi\phi}}{\partial x \partial \phi} + \frac{\partial^2 M_{xx}}{\partial x \partial \phi} + \frac{1}{a} \frac{\partial^2 M_{\phi x}}{\partial \phi^2} + N_{\phi\phi} - \rho a h \ddot{w} &= 0 \end{aligned} \right\} \quad (I. 1)$$

Based on the condition that  $a \gg z$  (so that  $a + z \approx a$ ) and the following equations for strains as functions of displacements

$$\left. \begin{aligned} \epsilon_x &= \frac{\partial u}{\partial x} - z \frac{\partial^2 w}{\partial x^2} \\ \epsilon_\phi &= \frac{1}{a} \frac{\partial v}{\partial \phi} + \frac{w}{a} - \frac{z}{a^2} \frac{\partial^2 w}{\partial \phi^2} \\ \gamma_{x\phi} &= \frac{\partial v}{\partial x} + \frac{1}{a} \frac{\partial v}{\partial \phi} - 2 \frac{z}{a} \frac{\partial^2 w}{\partial x \partial \phi} \end{aligned} \right\} \quad (I. 2)$$

we obtain the following differential equations for the displacements

$$\nabla^4 u + \frac{1}{a} \frac{\partial^3 w}{\partial x \partial y^2} - \frac{\nu}{a} \frac{\partial^3 w}{\partial x^3} - \frac{F}{a^2} \frac{\partial^2}{\partial t^2} \left[ \frac{3-\nu}{1-\nu} \nabla^2 u - \frac{2\nu}{a(1-\nu)} \frac{\partial w}{\partial x} - \frac{2F}{a^2(1-\nu)} \frac{\partial^2 u}{\partial t^2} \right] = 0 \quad (I. 3)$$

$$\nabla^4 v - \frac{2+\nu}{a} \frac{\partial^3 w}{\partial x^2 \partial y} - \frac{1}{a} \frac{\partial^3 w}{\partial y^3} - \frac{F}{a^2} \frac{\partial^2}{\partial t^2} \left[ \frac{3-\nu}{1-\nu} \nabla^2 v - \frac{2}{a(1-\nu)} \frac{\partial w}{\partial y} - \frac{2F}{a^2(1-\nu)} \frac{\partial^2 v}{\partial t^2} \right] = 0 \quad (I. 4)$$

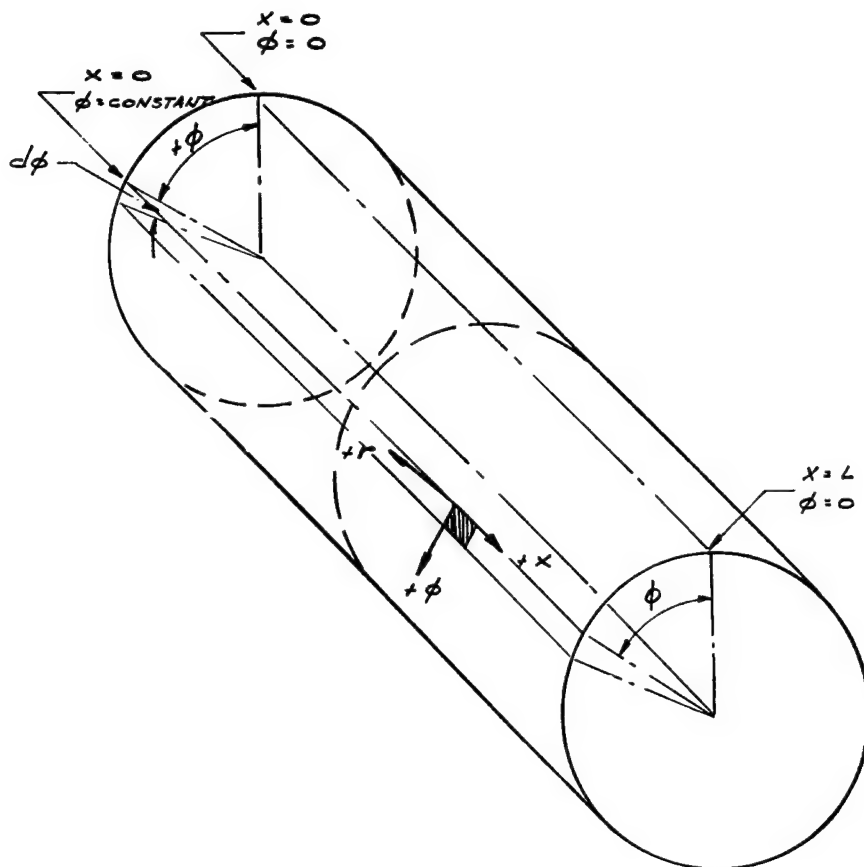


FIGURE I. 1. NOTATION FOR CYLINDRICAL SHELL

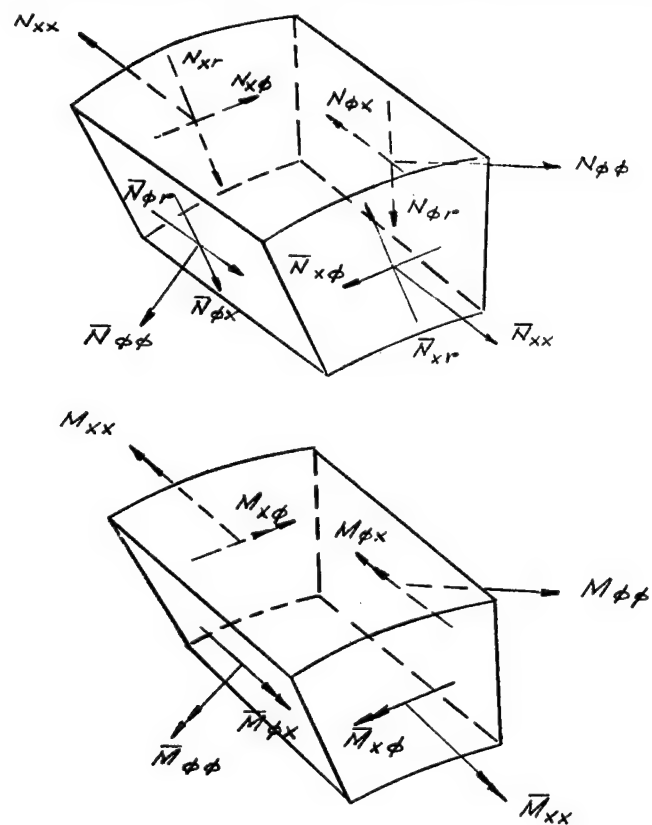


FIGURE I. 2. CYLINDRICAL SHELL STRESS RESULTANT NOTATION

$$\begin{aligned} \frac{D}{K} \nabla^8 w + \frac{1-\nu^2}{a^2} \frac{\partial^4 w}{\partial x^4} - \frac{F}{a^2} \frac{\partial^2}{\partial t^2} \left[ \left( \frac{3-\nu}{1-\nu} \nabla^2 - \frac{2F}{a^2(1-\nu)} \frac{\partial^2}{\partial t^2} \right) \left( \frac{F}{a^2} \frac{\partial^2 w}{\partial t^2} \right. \right. \\ \left. \left. + \frac{w}{a^2} + \frac{D}{K} \nabla^4 w \right) - \nabla^4 w - \frac{2}{a^2(1-\nu)} \left( \nu^2 \frac{\partial^2 w}{\partial x^2} + \frac{\partial^2 w}{\partial y^2} \right) \right] = 0 \end{aligned} \quad (I.5)$$

where

$$y = a\phi$$

$$F = \frac{\rho a^2 (1-\nu^2)}{E}$$

$$D = \frac{Eh^3}{12(1-\nu^2)}$$

$$K = \frac{Eh}{1-\nu^2}$$

The space and time dependent forms of the displacement equations are taken to be

$$u_{mn}(x, \phi, t) = \sum_j A_j e^{x a_j} \cos m\phi \sin \omega_{mn} t \quad (I.6)$$

$$v_{mn}(x, \phi, t) = \sum_j B_j e^{x a_j} \sin m\phi \sin \omega_{mn} t \quad (I.7)$$

$$w_{mn}(x, \phi, t) = \sum_j C_j e^{x a_j} \cos m\phi \sin \omega_{mn} t \quad (I.8)$$

where

$$a_j = \frac{\lambda_j}{L}$$

$m$  = number of circumferential waves  
( $2m$  = number of circumferential nodes)

Substituting Equations (I.6), (I.7), and (I.8) into Equations (I.3), (I.4), and (I.5), we have

$$\begin{aligned} \sum_j B_j e^{x a_j} \left\{ \frac{2\psi_{mn}^2}{1-\nu} \frac{3-\nu}{1-\nu} \psi_{mn} m^2 \left[ 1 - \left( \frac{a_j a}{m} \right)^2 \right] + m^4 \left[ 1 - \left( \frac{a_j a}{m} \right)^2 \right] \right\} \\ + m \sum_j C_j e^{x a_j} \left\{ \frac{2\psi_{mn}}{1-\nu} - m^2 \left[ 1 - (2+\nu) \left( \frac{a_j a}{m} \right)^2 \right] \right\} = 0 \end{aligned} \quad (I.9)$$

$$\sum_j A_j e^{x a_j} \left\{ \frac{2\psi_{mn}^2}{1-\nu} + \frac{3-\nu}{1-\nu} \psi_{mn} m^2 \left[ 1 - \left( \frac{a_j}{m} \right)^2 \right] + m^4 \left[ 1 - \left( \frac{a_j}{m} \right)^2 \right] \right\} \\ - a \sum_j a_j C_j e^{x a_j} \left\{ m^2 \left[ 1 + \nu \left( \frac{a_j}{m} \right)^2 \right] - \frac{2\psi_{mn}\nu}{1-\nu} \right\} = 0 \quad (I. 10)$$

$$\sum_j C_j e^{x a_j} \left[ 2\psi_{mn}^3 - \psi_{mn}^2 \left\{ 2 + (3-\nu)m^2 \left[ 1 - \left( \frac{a_j}{m} \right)^2 \right] \right\} \right. \\ \left. + \psi_{mn} \left\{ (1-\nu)m^2 \left[ 1 - \left( \frac{a_j}{m} \right)^2 \right] + (1-\nu)m^4 \left[ 1 - \left( \frac{a_j}{m} \right)^2 \right]^2 \right. \right. \\ \left. \left. + (3-\nu)km^6 \left[ 1 - \left( \frac{a_j}{m} \right)^2 \right]^3 \right\} - (1-\nu)km^3 \left[ 1 - \left( \frac{a_j}{m} \right)^2 \right] \right. \\ \left. - (1-\nu)(1-\nu^2)(a_j)^4 \right] = 0 \quad (I. 11)$$

where

$$\psi_{mn} = \frac{1-\nu^2}{E} \rho \omega_{mn}^2 a^2 \\ k = \frac{h^2}{12a^2}$$

Equations (I. 9), (I. 10), and (I. 11) are simplified by assuming that the shell wall thickness (a) and length (L) are such that

$$\left( \frac{a_j}{m} \right)^2 = \left( \frac{a \lambda_j}{mL} \right)^2 \ll 1.0$$

This simplification permits Equations (I. 6), (I. 7), and (I. 8) to be rewritten as follows

$$\left. \begin{aligned} u_{mn}(x, \phi, t) &= \frac{K_3}{K_1} \cos m\phi \sin \omega_{mn} t \sum_j a_j C_j e^{x a_j} \\ v_{mn}(x, \phi, t) &= \frac{K_2}{K_1} \sin m\phi \sin \omega_{mn} t \sum_j C_j e^{x a_j} \\ w_{mn}(x, \phi, t) &= \cos m\phi \sin \omega_{mn} t \sum_j C_j e^{x a_j} \end{aligned} \right\} (j = 1, 2, 3, 4) \quad (I. 12)$$

where

$$\begin{aligned} K_1 &= 2\psi_{mn}^2 - (3 - \nu) \psi_{mn} m^2 + (1 - \nu) m^4 \\ K_2 &= m[ m^2(1 - \nu) - 2\psi_{mn} ] \\ K_3 &= a[ 2\psi_{mn} \nu + (1 - \nu) m^2 ] \end{aligned}$$

From Equation (I.11), we also obtain the following frequency equation

$$\begin{aligned} 2\psi_{mn}^3 - \psi_{mn}^2[ 2 + (3 - \nu)m^2 + 2km^4 ] + \psi_{mn}[(1 - \nu)m^2 + (1 - \nu)m^4 \\ + (3 - \nu)km^6] - (1 - \nu)km^8 - (1 - \nu)(1 - \nu^2)(a\alpha_j)^4 = 0 \quad (j = 1, 2, 3, 4) \end{aligned} \quad (I.13)$$

The solution of Equation (I.13) for  $\psi_{mn}$  (and therefore the frequency  $\omega_{mn}$ ) depends on obtaining the appropriate values of  $\alpha_j$  ( $j = 1, 2, 3, 4$ ), which reflect the shell's end-closure boundary condition. For the fourth degree equation, the expected values of  $\alpha_j$  would be of the form

$$\alpha_1 = \frac{\kappa}{L}, \quad \alpha_2 = -\frac{\kappa}{L}, \quad \alpha_3 = \frac{i\kappa}{L} \text{ and } \alpha_4 = -\frac{i\kappa}{L}$$

where  $i = \sqrt{-1}$  and  $\kappa$  is a real number containing a term reflecting the axial mode shape.

## I.2 Lagrangian Equations of Motion

The development of the Lagrangian equations of motion necessary in the numerical analyses for the response of cylindrical shells to impulsive loading begins with the general displacement equations

$$\left. \begin{aligned} u(x, \phi, t) &= \sum u_{mn}(x, \phi, t) \\ v(x, \phi, t) &= \sum v_{mn}(x, \phi, t) \\ w(x, \phi, t) &= \sum w_{mn}(x, \phi, t) \end{aligned} \right\} \quad (I.14)$$

Utilizing Equations (I.12), these may be rewritten in terms of generalized coordinates

$$\left. \begin{aligned} u(x, \phi, t) &= \sum u_{mn}(x, \phi) q_{mn}(t) \\ v(x, \phi, t) &= \sum v_{mn}(x, \phi) q_{mn}(t) \\ w(x, \phi, t) &= \sum w_{mn}(x, \phi) q_{mn}(t) \end{aligned} \right\} \quad (I.15)$$

The expression for the kinetic energy is

$$T = \frac{\rho}{2} \int_0^L \int_0^{2\pi} \int_{-h/2}^{h/2} [\dot{u}(x, \phi, t)]^2 + [\dot{v}(x, \phi, t)]^2 + [\dot{w}(x, \phi, t)]^2 \} dx d\phi dz \quad (I. 16)$$

Since  $\dot{u}(x, \phi, t) = \sum u_{mn}(x, \phi) \dot{q}_{mn}(t)$  (and similarly for  $v$  and  $w$ ), Equation (I. 16) may be rewritten as

$$T = \frac{\rho ah}{2} \sum \int_0^L \int_0^{2\pi} \left\{ [u_{mn}(x, \phi) \dot{q}_{mn}(t)]^2 + [v_{mn}(x, \phi) \dot{q}_{mn}(t)]^2 + [w_{mn}(x, \phi) \dot{q}_{mn}(t)]^2 + u_{mn}(x, \phi) u_{ij}(x, \phi) \dot{q}_{mn}(t) \dot{q}_{ij}(t) + v_{mn}(x, \phi) v_{ij}(x, \phi) \dot{q}_{mn}(t) \dot{q}_{ij}(t) + w_{mn}(x, \phi) w_{ij}(x, \phi) \dot{q}_{mn}(t) \dot{q}_{ij}(t) \right\} dx d\phi \quad (I. 17)$$

where  $mn \neq ij$

Since the generalized coordinates are the principal or normal coordinates, the corresponding vibrations are the principal modes of vibration, and the products of the velocities in Equation (I. 17) vanish. That is, from Equations (I. 12), any one of the last three terms in Equations (I. 17) would be of the form

$$\dot{q}_{mn} \dot{q}_{ij} \int_{x=0}^x F_m(x) F_i(x) \left[ \int_{\phi=0}^{\phi=2\pi} G_n(\phi) G_j(\phi) d\phi \right] dx$$

where  $G_n(\phi) = \sin n\phi$  or  $\cos n\phi$ , and  $G_j(\phi) = \sin j\phi$  or  $\cos j\phi$ .

Thus

$$\int_{\phi=0}^{\phi=2\pi} G_n(\phi) G_j(\phi) d\phi = 0 \quad (\text{for } n \neq j)$$

and Equation (I. 17) becomes

$$T = \frac{\rho ah}{2} \sum [\dot{q}_{mn}(t)]^2 [\dot{u}_{mn}^* + \dot{v}_{mn}^* + \dot{w}_{mn}^*] \quad (I. 18)$$

where

$$\dot{u}_{mn}^* = \int_0^L \int_0^{2\pi} [u_{mn}(x, \phi)]^2 dx d\phi \quad (I. 19)$$

and similarly for  $\dot{v}_{mn}^*$  and  $\dot{w}_{mn}^*$ .

The expression for the potential (strain) energy in terms of the derivative of the displacement components and the generalized coordinates may be obtained by utilizing Equations (I. 2) and (I. 15) in the following

$$V = \frac{Ea}{2(1-\nu^2)} \int_{-h/2}^{+h/2} \int_0^L \int_0^{2\pi} \left[ \epsilon_x^2 + \epsilon_\phi^2 + 2\nu\epsilon_x\epsilon_\phi + \frac{1-\nu}{2} \gamma_{\phi x}^2 \right] dx d\phi dz \quad (I. 20)$$

Since terms containing products of the generalized coordinates vanish, Equation (I. 20) may be rewritten as follows

$$V = \frac{Ea}{2(1-\nu^2)} \sum [q_{mn}(t)]^2 \left[ h \int_0^L \int_0^{2\pi} F(u, v, w) dx d\phi \right] + \frac{h^3}{4} \int_0^L \int_0^{2\pi} G(u, v, w) dx d\phi \quad (I. 21)$$

where  $F(u, v, w)$  and  $G(u, v, w)$  denote a collection of terms involving the partial derivatives of  $u_{mn}(x, \phi)$ ,  $v_{mn}(x, \phi)$ , and  $w_{mn}(x, \phi)$  with respect to  $x$  and  $\phi$ .

From Equation (I. 21), we have

$$\frac{\partial V}{\partial q_{mn}(t)} = H(u, v, w) q_{mn}(t) \quad (I. 22)$$

where  $H(u, v, w)$  are merely the combined constant and integral terms.

For Lagrange's equations, we have

$$\frac{d}{dt} \left[ \frac{\partial T}{\partial \dot{q}_{mn}(t)} \right] - \frac{\partial T}{\partial q_{mn}(t)} + \frac{\partial V}{\partial q_{mn}(t)} = Q_{mn}(t) \quad (I. 23)$$

From Equation (I. 20)

$$\frac{\partial T}{\partial q_{mn}(t)} = 0 \quad (I. 24)$$

$$\frac{d}{dt} \left[ \frac{\partial T}{\partial \dot{q}_{mn}(t)} \right] = \rho a h \ddot{q}_{mn}(t) [\dot{u}_{mn}^* + \dot{v}_{mn}^* + \dot{w}_{mn}^*] \quad (I. 25)$$

Introducing Equations (I. 22), (I. 24), and (I. 25) into Equation (I. 23)

$$\rho a h [\dot{u}_{mn}^* + \dot{v}_{mn}^* + \dot{w}_{mn}^*] \ddot{q}_{mn}(t) + H(u, v, w) q_{mn}(t) = Q_{mn}(t) \quad (I. 26)$$

Expressing Equation (I. 26) in a more convenient form, we have

$$\ddot{q}_{mn}(t) + \omega_{mn}^2 q_{mn}(t) = \frac{Q_{mn}(t)}{M_{mn}} \quad (\text{I. 27})$$

where

$$M_{mn} = \rho a h [\dot{u}_{mn}^* + \dot{v}_{mn}^* + \dot{w}_{mn}^*] \quad (\text{generalized mass})$$

$$\omega_{mn}^2 = \frac{H(u, v, w)}{M_{mn}}$$

$$Q_{mn}(t) = \text{Generalized force}$$

$$= \int_0^L \int_0^{2\pi} P(x, \phi, t) w_{mn}(x, \phi) \, dx d\phi$$

For the numerical solution of Equation (I. 27), the method of finite differences was used, and, taking the second central differences, we have

$$\ddot{q}_{mn}(t_i) = \frac{q_{mn}(t_r) - 2q_{mn}(t_i) + q_{mn}(t_l)}{(\Delta t)^2}$$

or

$$q_{mn}(t_r) = \frac{Q_{mn}(t_i)}{M_{mn}} (\Delta t)^2 + [2 - \omega_{mn}^2 (\Delta t)^2] q_{mn}(t_i) - q_{mn}(t_l) \quad (\text{I. 28})$$

where

$$t_r = t_i + \Delta t$$

$$t_l = t_i - \Delta t$$

### I. 3 Development of Load Spectrums

In obtaining the expression for the generalized force in Equation (I. 27), use was made of the loading information for cylindrical shells contained in References I. 3 and I. 4, as well as other publications. Basically, the time variation of the loading along any one element of the cylinder can be considered of the form shown in Figure I. 3 or I. 4, the former utilizing the information from Reference I. 3, and the latter from Reference I. 4.

In both cases, time is measured from the instant the shock front strikes the leading edge (element at  $\phi = 0^\circ$ ) of the cylinder. Again, both forms include the arrival time ( $t_a$ ) for each particular cylinder element, the duration of the diffraction loading phase ( $t_D$ ) and the positive phase duration ( $t_+$ ). The drag phase (for  $t \geq t_D$ ) is given by

$$P = P_I(t) + C_d(\phi) q(t) \quad (\text{I. 29})$$

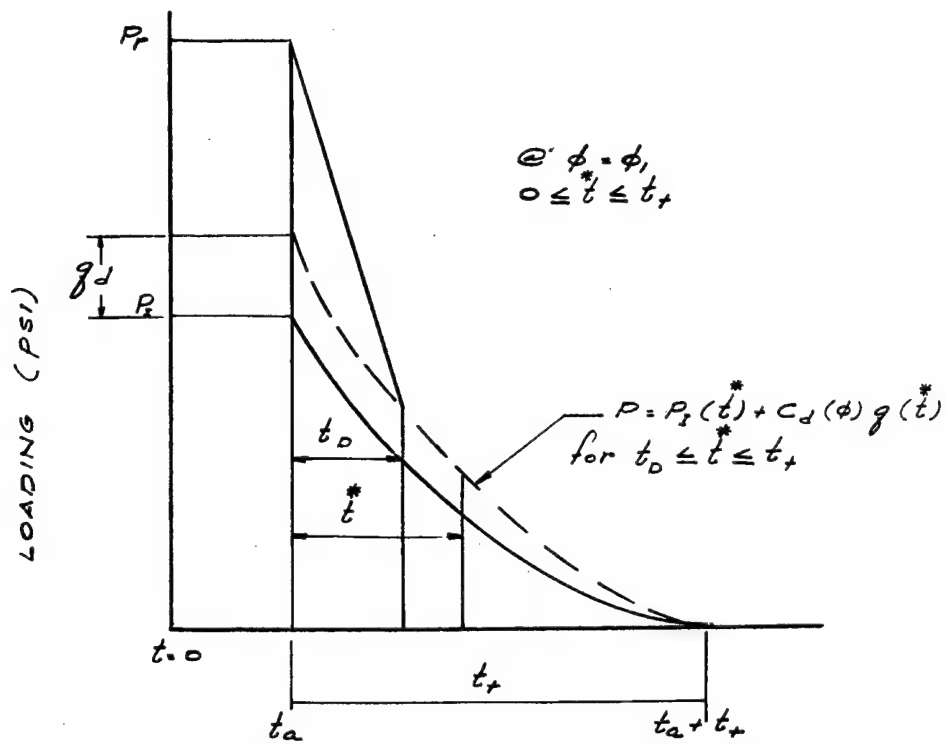


FIGURE I.3. LOADING SPECTRUM AT POINTS ON FRONT HALF OF CYLINDER

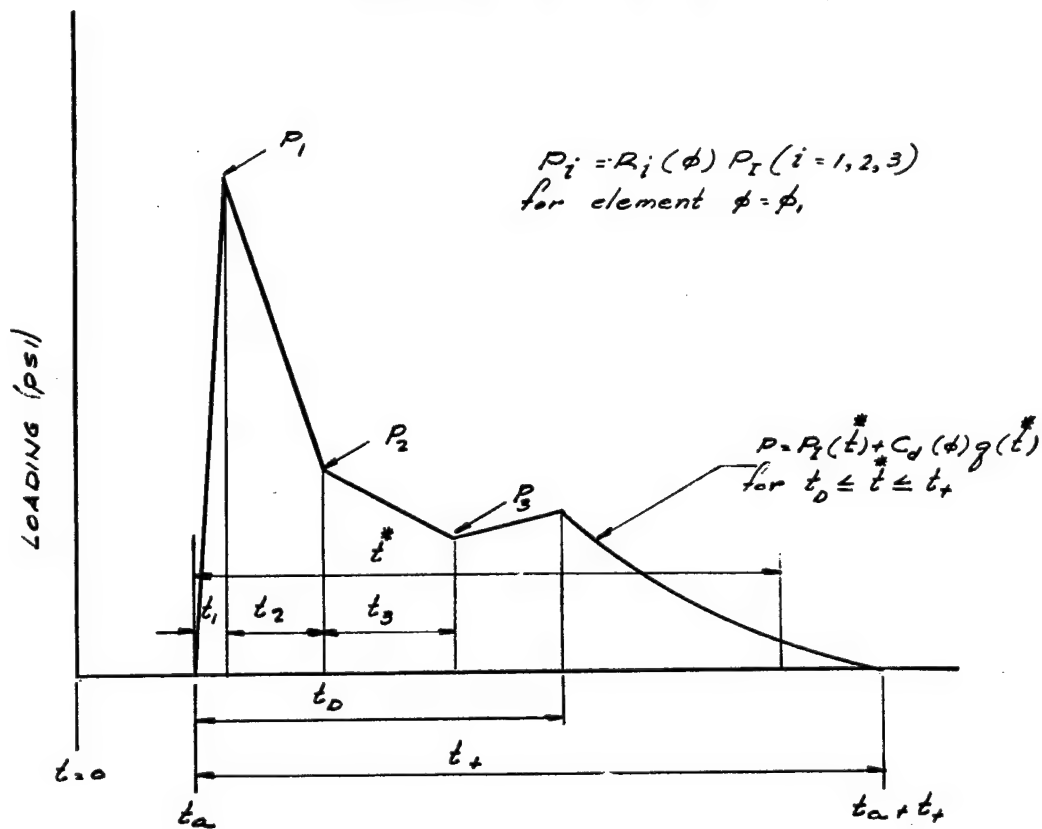


FIGURE I.4. SCHEMATIC OF PRESSURE PROFILE FOR SHELL AT ELEMENT  $\phi = \phi_1$

where, for the time increment  $0 < \bar{t} \leq t_+$  measured chronologically from  $t_a$ , the relationship for  $P_I(\bar{t})$  and  $q(\bar{t})$  is given in Figure I. 5, and  $C_d(\phi)$  is the drag coefficient for the particular cylinder element under consideration. For the loading shown in Figure I. 3, the drag coefficient  $C_d(\phi)$  is obtained from Figure 6.82b, page 272, Reference I. 3; for the loading shown in Figure I. 4,  $C_d(\phi)$  is found from the curve reproduced in Figure I. 6.

The essential difference between the pressure profiles shown in Figures I. 3 and I. 4 lies in the diffraction phase. Since the pressure profile in Figure I. 4 represented a more realistic loading condition, there was reason to tend towards this approach. Taking into account the experimental model's dimensional ratios ( $L/D$ ), the crossover times ( $D/U$ ) and the anticipated (as well as experimentally recorded) durations, there appeared to be adequate aerodynamic similitude to justify using the experimental curves in Reference I. 4 in determining the appropriate values of  $P_I$ ,  $t_i$  and  $t_D$  for this investigation's loadings. Moreover, the maximum deformations were found to occur at times approximately equal to or less than the diffraction phase duration ( $t_D$ ). This meant that the diffraction phase constituted the major (and, in some cases, the entire) deformational loading.

The curves used in determining the significant values of time and loading required to define the load spectrum in Figure I. 4 are given in Figures I. 7 through I. 9. The basic, computational procedure was as follows: the values of the peak incident overpressure ( $P_I$ ) and positive phase duration ( $t_+$ ) were obtained from Tables III. 1 and III. 2. The variation of the incident overpressure and the dynamic pressure (see Fig. I. 5) were found from the following relations

$$P_I(\bar{t}) = P_I \left( 1 - \frac{\bar{t}}{t_+} \right) \exp \left( - \frac{\bar{t}}{t_+} \right) \quad (I. 30)$$

$$q(\bar{t}) = q_d \left[ \left( 1 - \frac{\bar{t}}{t_+} \right) \exp \left( - \frac{\bar{t}}{t_+} \right) \right]^2 \quad (I. 31)$$

where

$$q_d = \frac{2.5 P_I^2}{7 P_o + P_I} \quad (\text{psi})$$

$P_o$  = Ambient pressure

Next, the crossover time ( $D/U$ ) was computed, where

$$U = C_o \left( 1 + \frac{6 P_I}{P_o} \right)^{1/2} \quad (\text{ft per sec}) \quad (I. 32)$$

$C_o$  = Ambient sound velocity (ft per sec)

From Figures I. 7 and I. 8, the appropriate values for  $t_a$ ,  $t_i$  and  $t_D$  were obtained for each element in the cylinder's surface. A numerical analysis to determine the optimum number of elements to be considered showed that for increments of  $\Delta\phi = 10^\circ$ ,  $15^\circ$  or  $22.5^\circ$ , only minor differences existed in the final numerical results. Thus, in all subsequent computations, the elements considered were those at  $\phi = 0^\circ$ ,  $22.5^\circ$ ,  $45^\circ$ , ...,  $180^\circ$ .

The values of  $R_I(\phi)$  for each element were obtained from Figure I. 9. The appropriate value of  $P_I$  corresponding to the time  $t_i$  was determined from Equation (I. 30) (where  $\bar{t} = t_i$ ) or

from  $P_I(t)^*$  curves such as are shown in Figure I. 5. The critical pressures were then found for each element

$$P_i = R_i(\phi) P_I(t_I)$$

Typical values for critical pressures and times are given in Table I. 1; the corresponding load spectrums are shown in Figure I. 10.

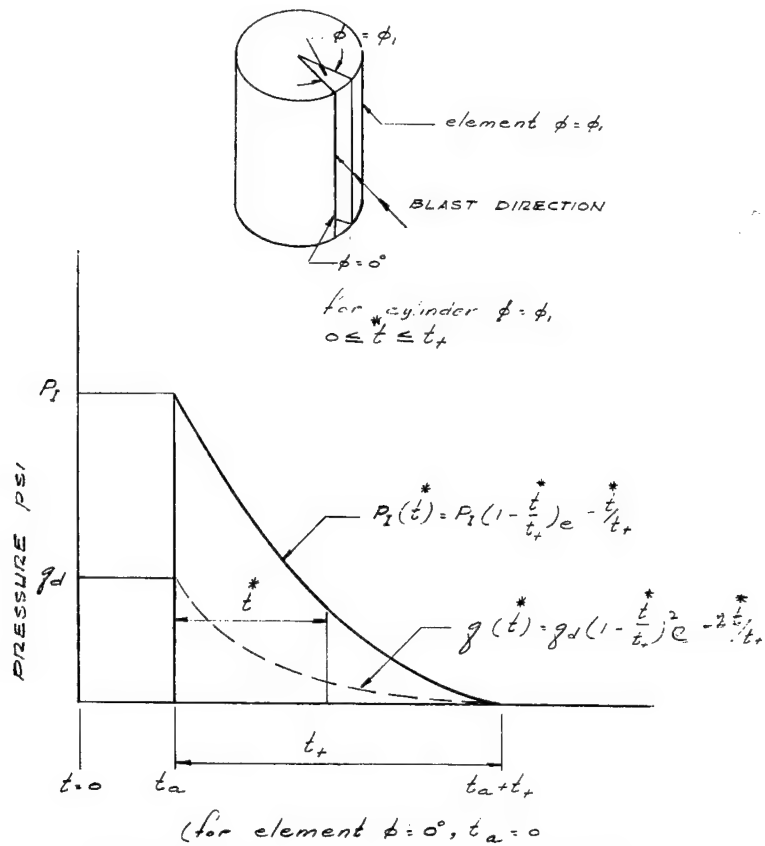


FIGURE I. 5. INCIDENT OVERPRESSURE AND DYNAMIC PRESSURE VERSUS TIME

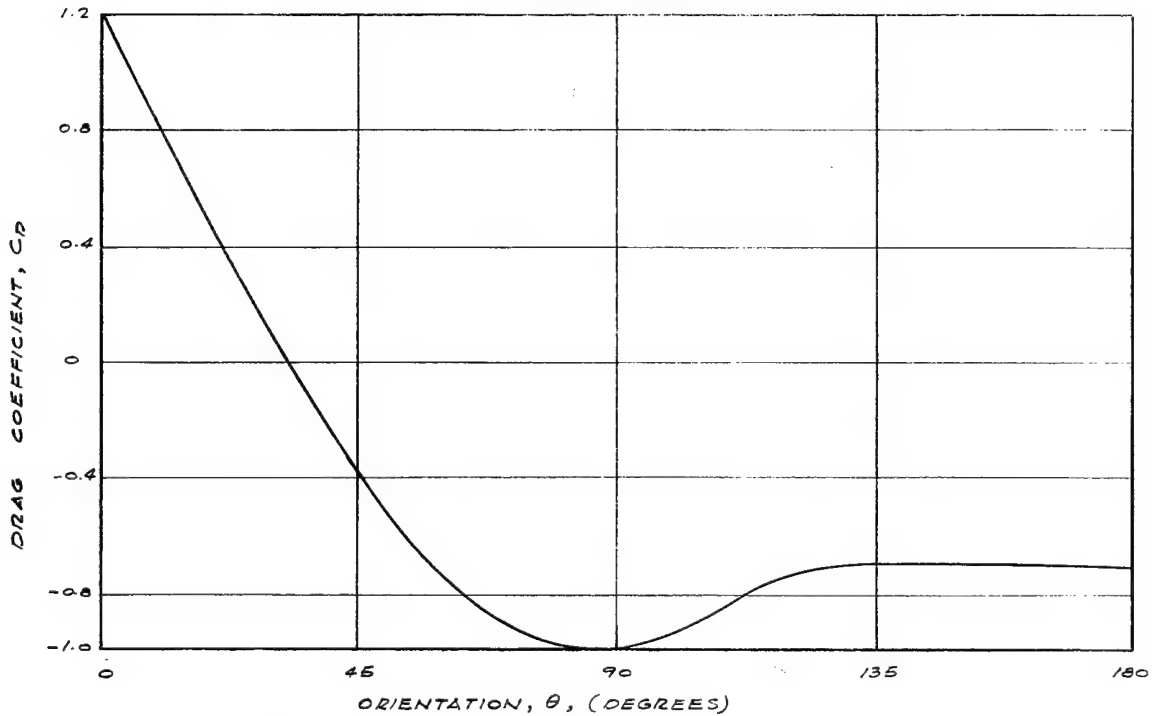


FIGURE I. 6. VARIATION OF DRAG COEFFICIENT WITH CYLINDER ELEMENT

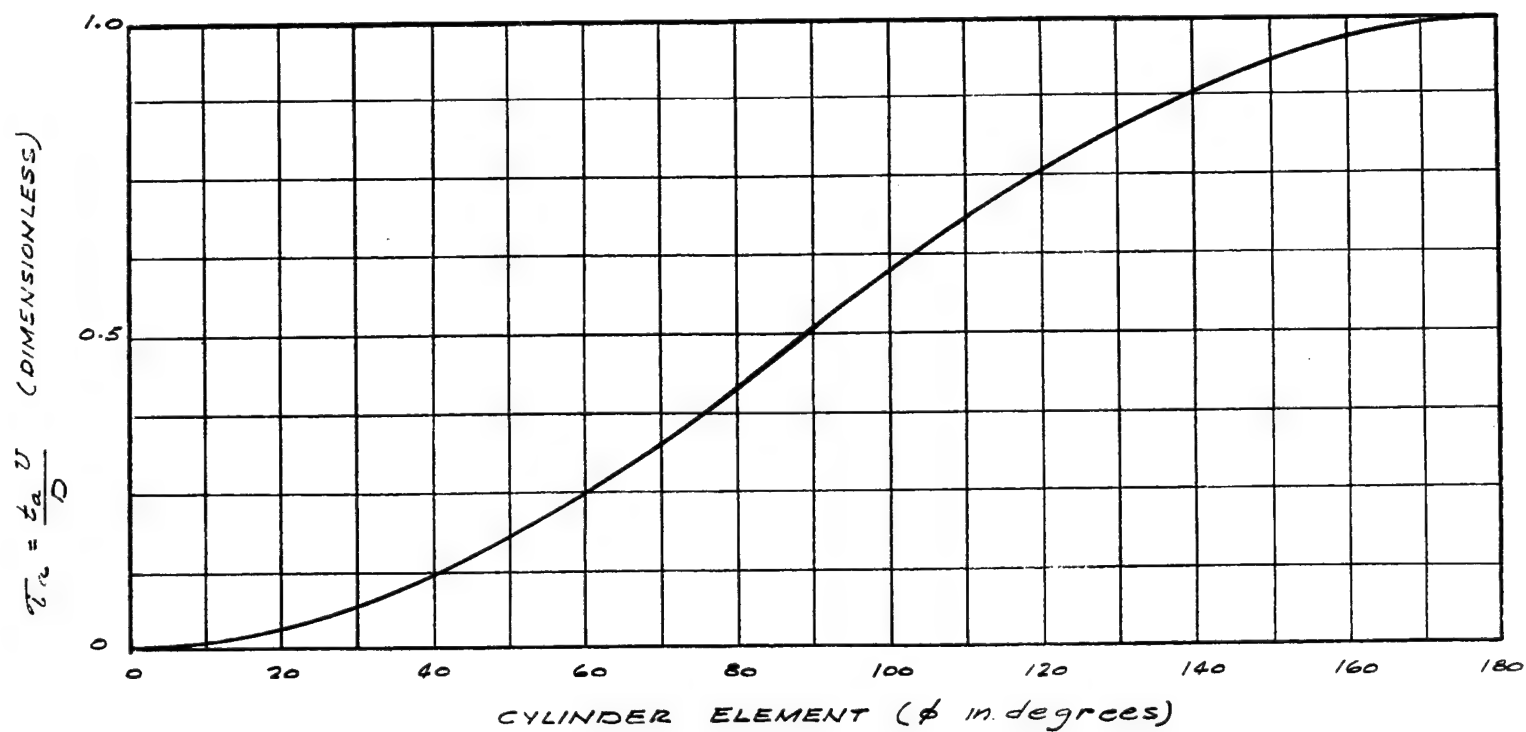


FIGURE I. 7. TIME OF ARRIVAL OF SHOCK FRONT ON CYLINDER SURFACE

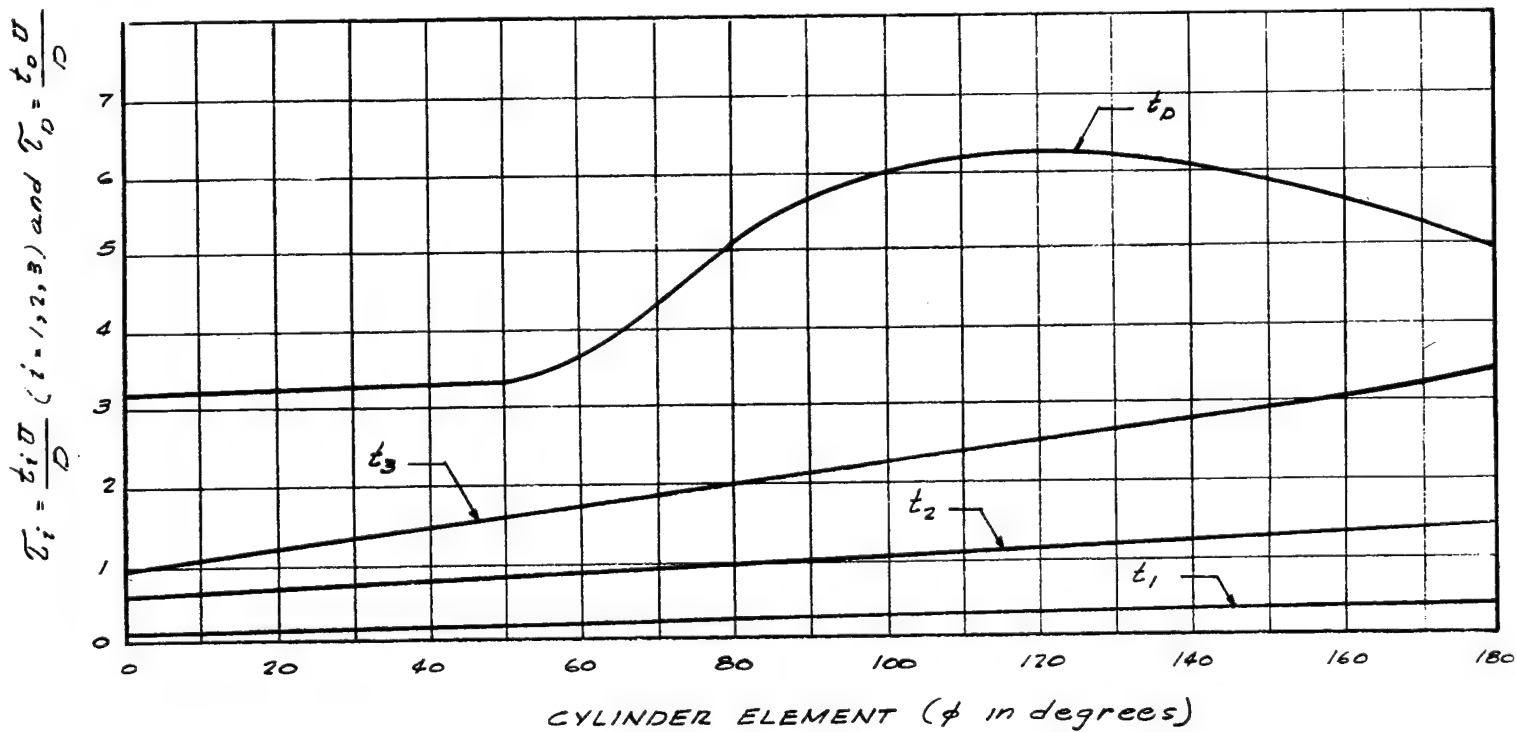


FIGURE I. 8. VARIATION OF CRITICAL TIMES (\$t\_i\$) AND DIFFRACTION PHASE DURATION (\$t\_D\$) WITH CYLINDER ELEMENT

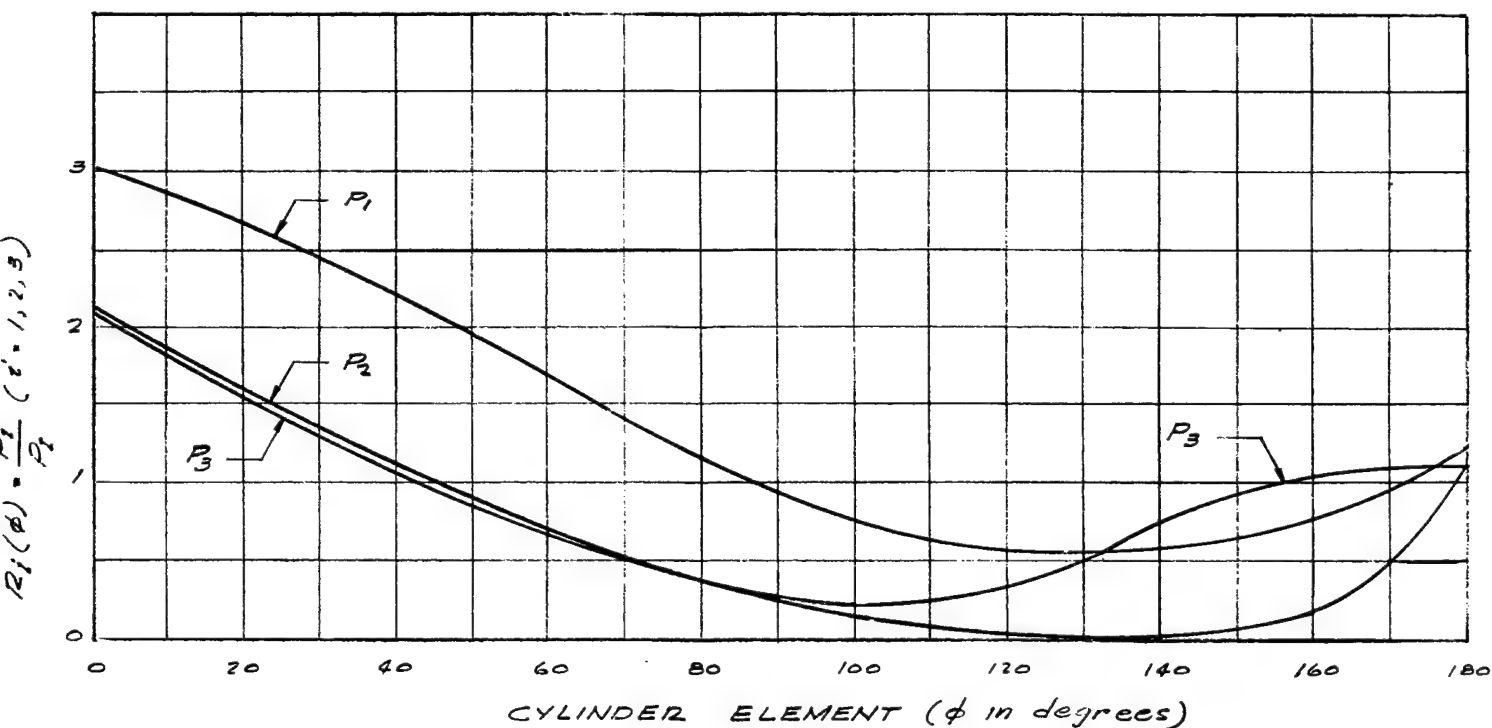


FIGURE I. 9. VARIATION OF CRITICAL PRESSURE ( $P_i$ ) TO PEAK INCIDENT OVERPRESSURE ( $P_I$ ) RATIOS WITH CYLINDER ELEMENT

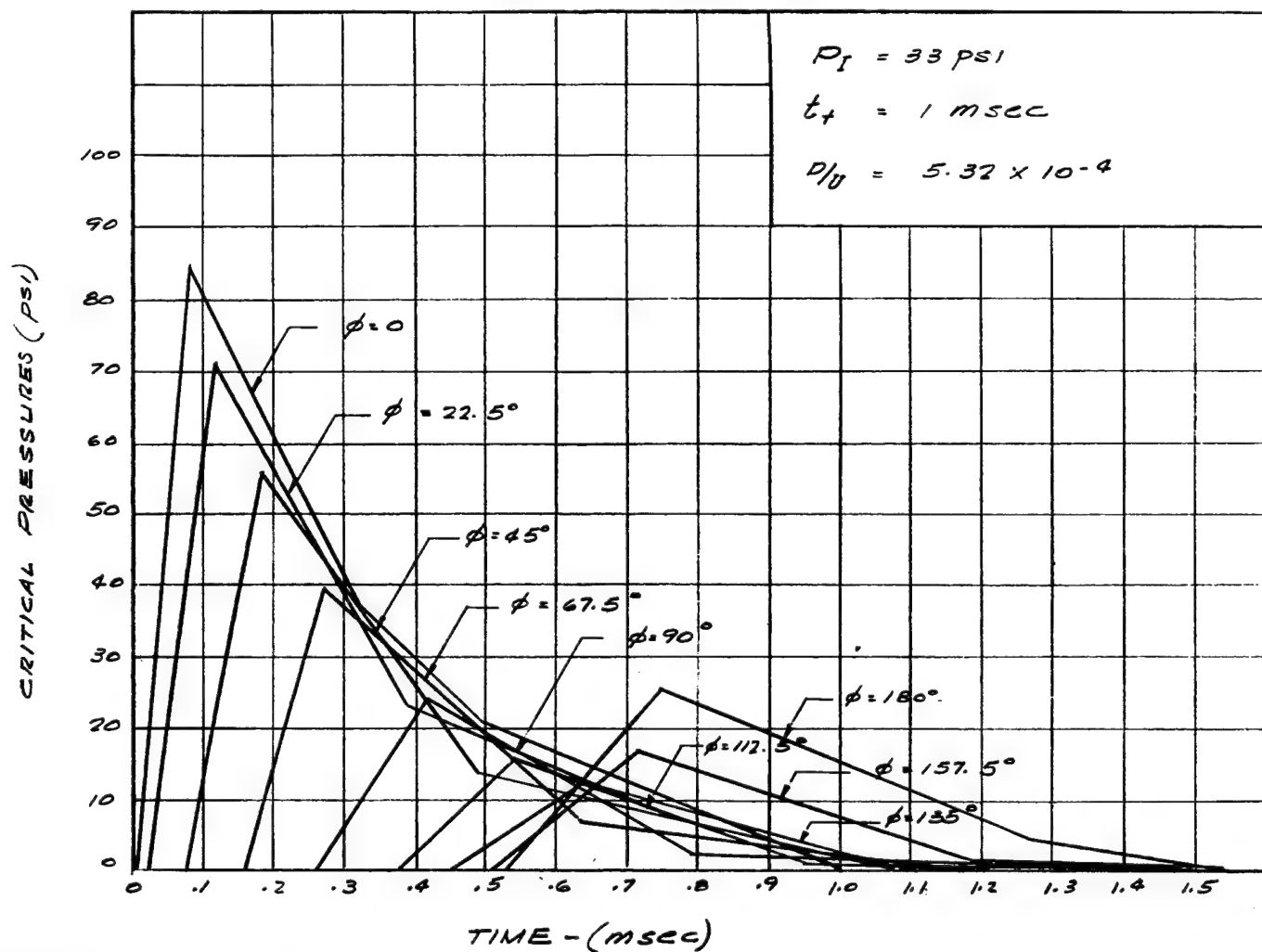


FIGURE I. 10. PRESSURE PROFILES ALONG VARIOUS ELEMENTS OF CYLINDRICAL SURFACE

TABLE I. 1. CRITICAL TIMES AND PRESSURES ( $P_I = 33$  psi,  
 $t_t = 1$  msec)  $D/U = 0.53$  msec

<u><math>\phi</math></u>	<u><math>t_a</math></u> msec	<u><math>t_1</math></u> msec	<u><math>P_1</math></u> psi	<u><math>t_2</math></u> msec	<u><math>P_2</math></u> psi	<u><math>t_3</math></u> msec	<u><math>P_3</math></u> psi	<u><math>t_D</math></u> msec
0	0	.08	85	.32	18	.51	21	1.7
22.5	.02	.10	70	.37	14	.65	9	1.7
45.0	.07	.11	55	.41	13	.77	3	1.8
67.5	.16	.12	39	.48	11	.97	0	2.2
90.0	.27	.15	24	.52	10	1.1	0	3.0
112.5	.37	.16	15	.58	8	1.3	0	3.3
135.0	.45	.19	12	.62	7	1.5	0	3.3
157.5	.51	.20	16	.68	5	1.6	0	3.0
180.0	.53	.21	25	.74	4	1.8	0	2.7

## REFERENCES - APPENDIX I

- I. 1 Yu, Yi-Yuan, "Free Vibrations of Thin Cylindrical Shells," Jour. Appl. Mech., December 1955.
- I. 2 Flügge, W., "Stalid und Dynamid der Schalen," Julius Springer, Berlin, 1934.
- I. 3 "The Effects of Nuclear Weapons," United States Atomic Energy Commission, June 1957.
- I. 4 "Blast Effects on Tank Structures," Final Test Report No. 16, Armour Research Foundation.

Reported from doc 87b  
Nov 15, 1955

## APPENDIX II

### EXPERIMENTAL PROGRAM

#### II.1. OBJECTIVES

It was deemed advisable to undertake a limited experimental program which would provide data to test the adequacy of the analytical procedures. Knowing that the analytical results would be in the form of predicted displacements, an experimental technique was evolved for obtaining records of the response of cylindrical shells or flat plates to known blast loadings.

#### II.2. MODEL DESIGN

##### II.2.1 Cylindrical Shells

All the cylindrical shell models had the same overall nominal dimensions: diameter - 12", length - 36", shell wall thickness - 0.036". The three basic configurations differed with respect to the end-closures and the related shell boundary condition. For the Type CA specimen (Figure II.2), the shell was welded to a 1/2" thick end plate so as to closely approximate a shell with fixed-end conditions. The end-closures for the Type CB specimen simulated a shell with a simply-supported boundary condition (Figure II.3). Type CC shell models use end plates of the same nominal thickness as the shell (0.036"). These plates were welded to the shell as is shown in Figure II.1. The Type CC models provided an elastic boundary and were used to demonstrate the effect of end restraints of flat plate end-closures.

Within each CB type model, a scribe plate was mounted at mid-length on the three support rods (see Figure II.3). Four, spring-loaded styli, supported on the scribe plate and bearing against the shell wall, were used to record the deflection at mid-plane points on the 0°, 90°, 180°, and 270° elements of cylinder (0° denoting the blast side of the cylinder). A black longitudinal and circumferential grid on one-inch spacing was painted on the yellow surfaces of the models used in series D, A, G and H.

##### II.2.2. Circular Flat Plates

The test fixture used to support the circular flat plates is shown in Figure II.4. As shown in the drawing, the plate is simply supported at the boundary; for the fixed boundary condition, an oversized plate was used and clamped between the inner pipe and the outer ring. In order to evaluate the effects of membrane and beam action, 0.0312" and 0.0598" thick plates were tested. White radial lines at 45° were painted on blue plate surfaces.

#### II.3. INSTRUMENTATION

Instrumentation consisted of synchronized, high-speed photography to record the cylinders' dynamic response, mechanical styli recordings of maximum deformations, and a quartz transducer system to record overpressures and positive phase durations. Each model was covered by one or two high-speed cameras with film speeds from 3,000 to 5,000 frames per second. A sequence circuit was constructed to synchronize the detonation and camera action so that the initial impact of the shock wave on the model would occur when the cameras had obtained their maximum speed.

Two quartz transducers were flush-mounted in a 18" X 24" steel surface plate. An adaptor, consisting of a double brass fitting separated by a viscous potting material, was constructed to minimize ground acceleration effects in the pickup. The transducers were placed at ground level at radial distances from ground zero equal to those from ground zero to the model. The transducers' outputs were fed through amplifier-calibrators to an oscilloscope and recorded by oscillograph cameras.

#### II.4. TEST PROGRAM

A total of nineteen charges in nine series was detonated. The charges used and the cylindrical shell models and flat plates exposed in each shot are given in Table II.1. Each cylindrical

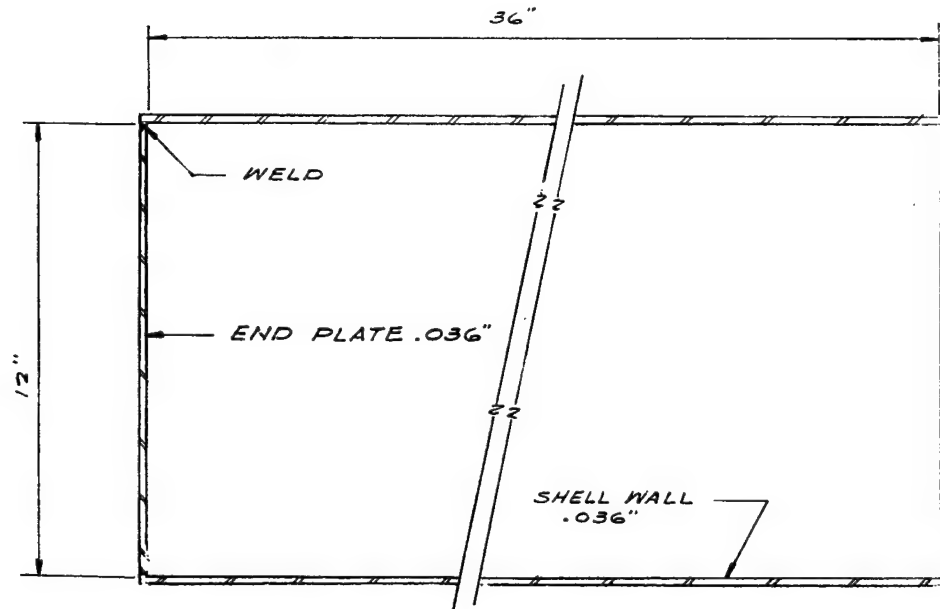


FIGURE II. 1. TYPE CC CYLINDRICAL SHELL MODEL

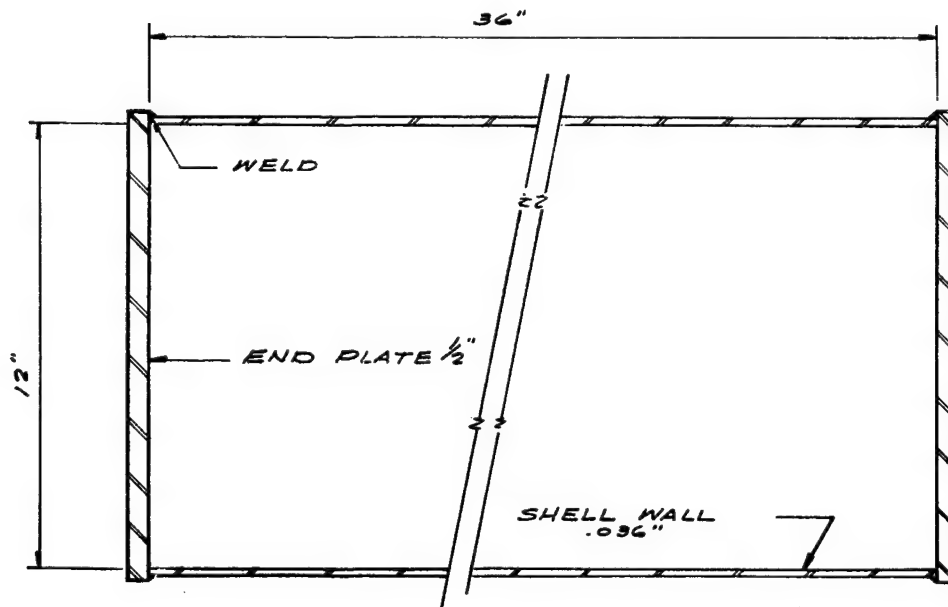


FIGURE II. 2. TYPE CA CYLINDRICAL SHELL MODEL

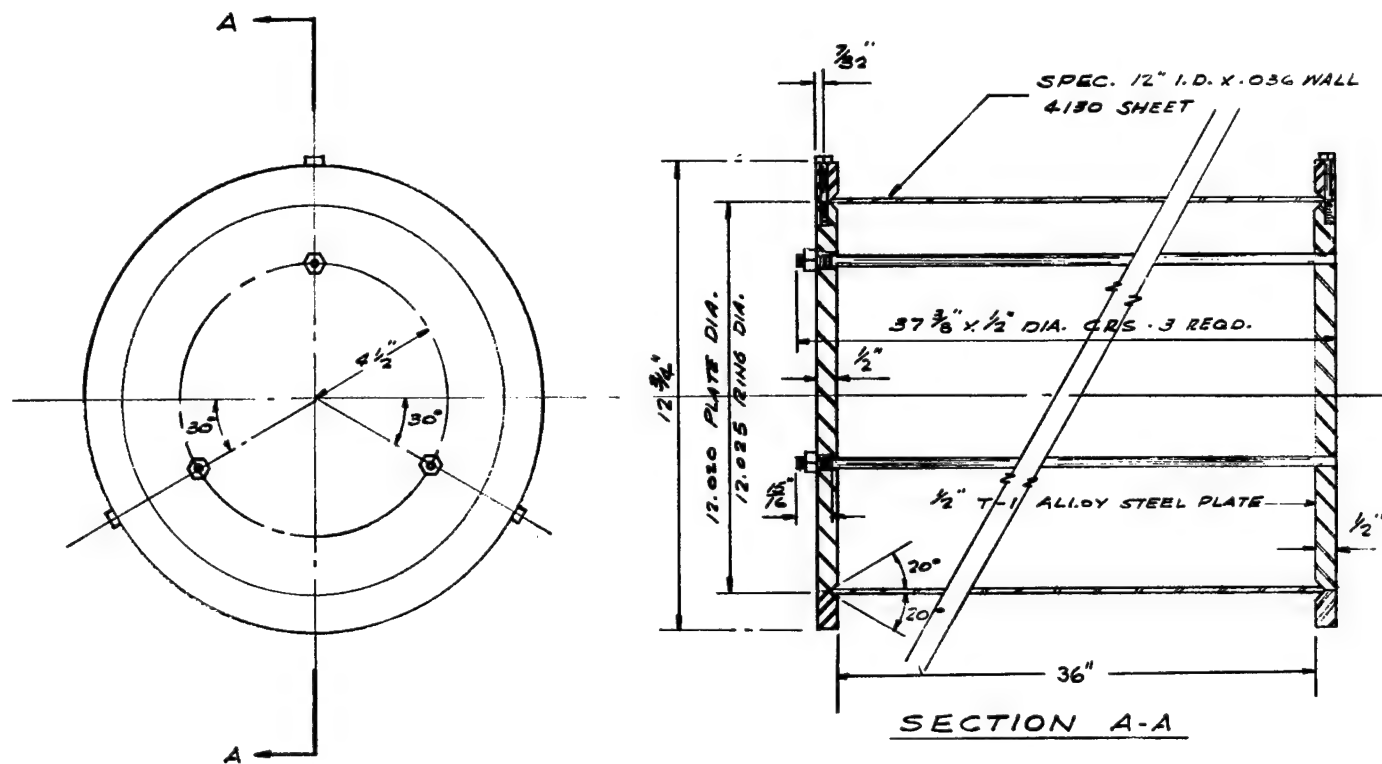


FIGURE II. 3. TYPE CB CYLINDRICAL SHELL MODELS

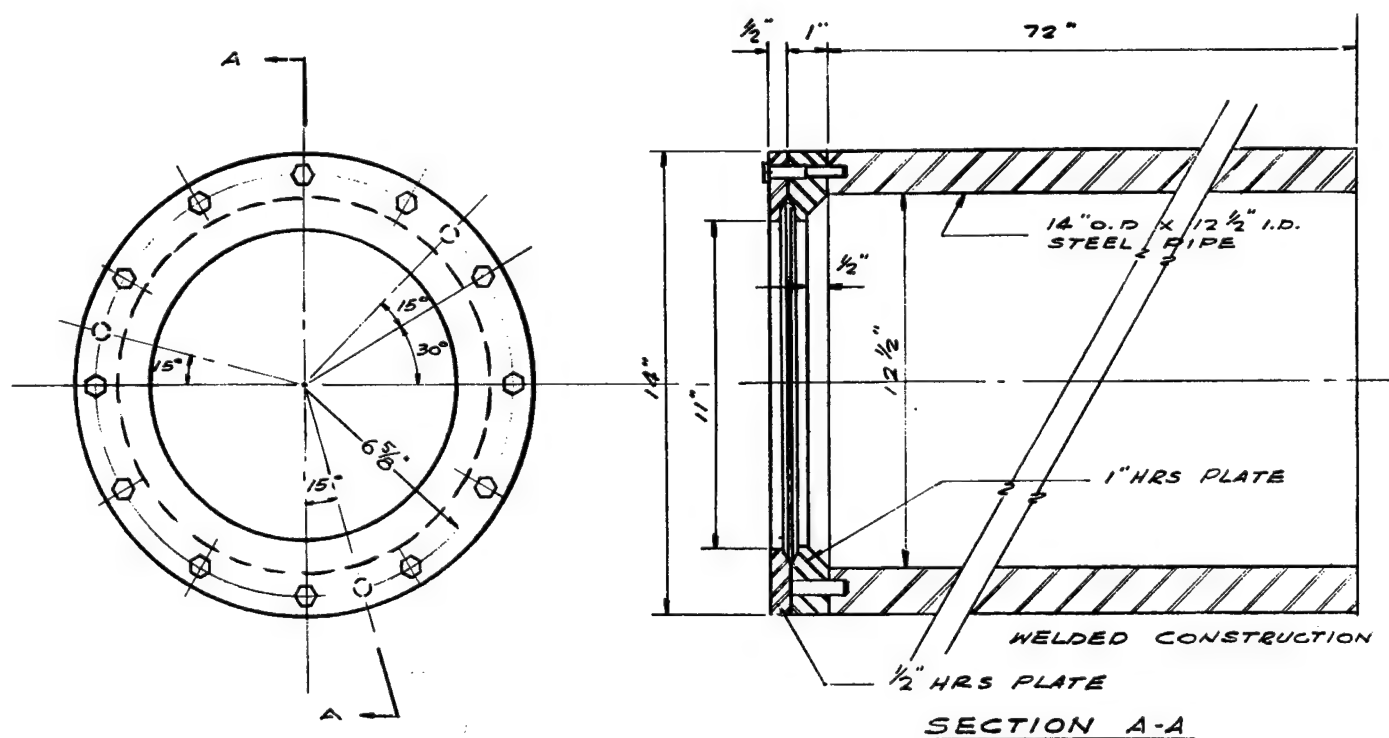


FIGURE II. 4. FIXTURE FOR CIRCULAR, FLAT PLATE MODELS

TABLE II.1. SUMMARY OF EXPERIMENTAL PROGRAM

Shot No.	Charge (1) (lb)	Model (2)	Model Orientation (2)	Range (3) (ft)	HOB (4) (ft)	Instrumentation			Model Failure Status
						(5)	(6)	(7)	
(1) Flaked TNT		(3) Distance to leading edge		(8) No visible damage		(9) No additional damage		(10) Permanent inward deformation	
(2) See Figures II. 5 thru II. 8		(4) Height of burst		(5) High-speed photography		(6) Mechanical styli data		upstream end plate - maximum displacement 1/2"	
E end-on loading									
S side-on loading									
O oblique loading									
A1	15	CC1	E	31.5	2.5	None	None	None	(8)
A1	15	CC2	S	63.5	2.5	None	None	None	(8)
A2	15	CC1	E	25.5	2.5	None	None	None	(8)
A2	15	CC2	S	32.5	2.5	None	None	None	(8)
A3	15	CC1	E	16.5	2.5	None	None	None	See Fig. II. 9
A3	15	CC2	S	19.5	2.5	None	None	None	(8)
B1	15	CC1	S	19.0	2.5	None	None	None	(9)
B1	15	CC2	S	15.5	2.5	None	None	None	See Fig. II. 11
B2	15	CC1	S	17.0	2.5	None	None	None	(9)
B2	15	CC2	S	13.5	2.5	None	None	None	See Fig. II. 12
B3	15	CC1	S	14.5	2.5	None	None	None	See Fig. II. 10
C1	30	CC3	S	18.5	2.5	None	None	None	See Fig. II. 13
C1	30	CC4	E	21.5	2.5	None	None	None	(10)
C1	30	CC5	O (45°)	27.0	2.5	None	None	None	(8)
C1	30	CA1	E	21.5	2.5	None	None	None	(8)
C1	30	CA2	S	18.5	2.5	None	None	None	See Fig. II. 16
C2	30	CC4	E	19.5	2.5	None	None	None	See Fig. II. 14
C2	30	CC5	O (45°)	24.0	2.5	None	None	None	See Fig. II. 15
C2	30	CA1	E	19.5	2.5	None	None	None	(8)
D1	30	CA3	S	26	2.5	Good	Fair	Fair	(8)
D2	30	CA3	S	22	2.5	Good	Good	Fair	(8)
D3	30	CA3	S	16	2.5	Good	Fair	Fair	See Fig. II. 17a
E1	5	None	--	----	0.25	----	----	Good	---
E2	5	None	--	----	0.25	----	----	Good	---
E3	5	None	--	----	0.25	----	----	Good	---
F1	30	CB1	S	20	1.5	Fair	None	Good	(8)
F2	30	CB1	S	16	1.5	Not useable	None	Good	See Fig. II. 17b
G1	5	CB2	S	10	0.25	Good	Good	Fair	(8)
G2	5	CB2	S	10	0.25	Good	Good	Good	(8)
G3	5	CB2	S	10	0.25	Good	Good	Good	(8)
G4	5	CB2	S	10	0.25	Good	Good	Good	(8)
H1	30	CB2	S	20	2.5	Good	Fair	Fair	See Fig. II. 17c
H2	30	None	S	20	2.5	None	None	Good	---
H3	30	CB3	S	20	2.5	Good	Good	Good	(8)
H4	30	CB3	S	15	2.5	Good	Good	Good	See Fig. II. 17d
J1	5	P1	--	10	0.25	Good	None	Good	---
J2	5	P2	--	10	0.25	Good	None	Good	---
J3	5	P2	--	5	0.25	Not useable	None	Good	---

shell model was suspended with nylon cords; the position and orientation of each model relative to ground zero are shown in Figures II. 5 through II. 8; the controlling distances are given in Table II. 1.

Shot series A through C were used to obtain qualitative information on the deformational response of the cylindrical shells as influenced by such factors as the distance and orientation of models with respect to ground zero. In particular, the tests were used to determine the modes of failure (in the form of permanent deformation or fracture) as related to estimated overpressure.

The tests using 5 lb of flaked TNT (Series E and G) were conducted on Southwest Research Institute grounds for the purpose of checking out the equipment and instrumentation. In Series G, the distance between the model and the charge was 10 feet, and, at this distance, it was possible to photograph small (but measurable) elastic deformations and mode shapes. The ground zero-to-model distances for the 30-lb shots at Camp Bullis varied from 26 feet to 15 feet; each series of shots terminated with failure of the model in the form of large, permanent deformations. (See Figures II. 9 through II. 17.)

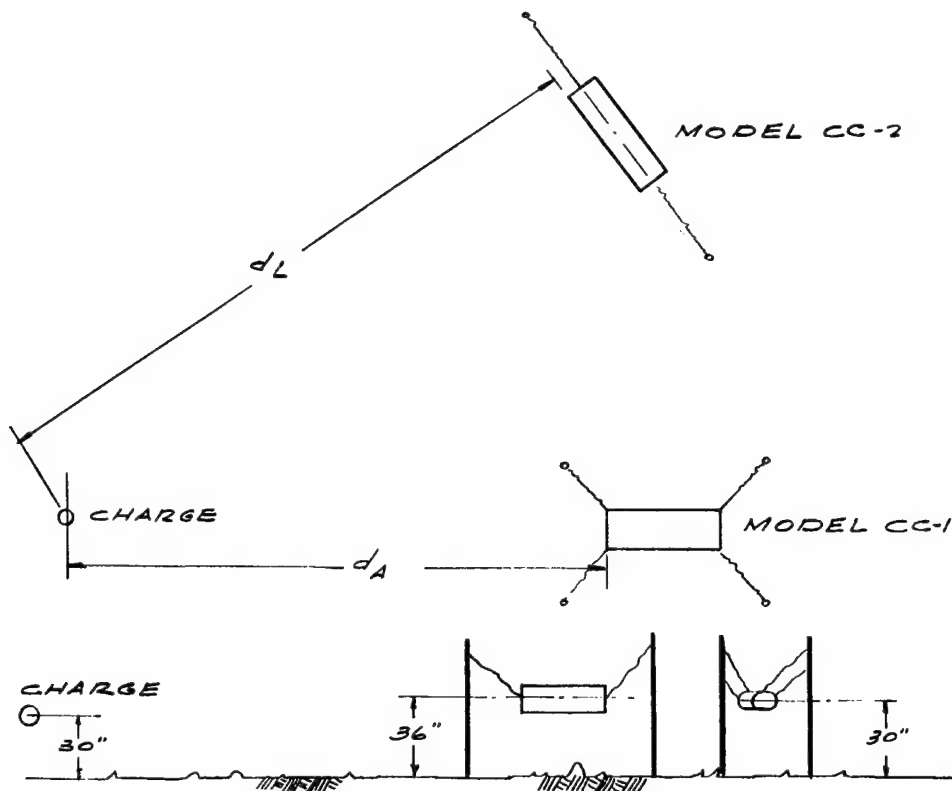


FIGURE II. 5. MODEL POSITIONS FOR SHOTS A1, A2, AND A3

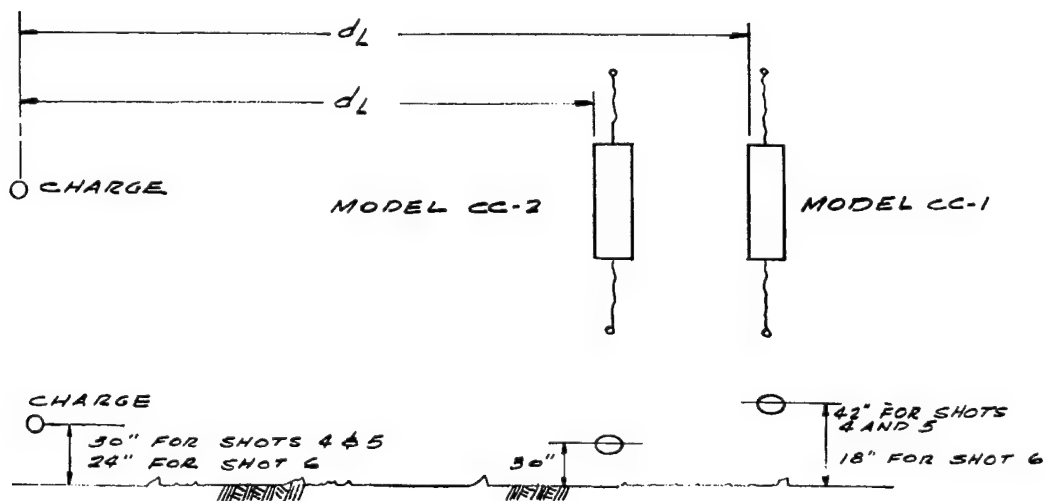


FIGURE II. 6. MODEL POSITIONS FOR SHOTS B1, B2, AND B3

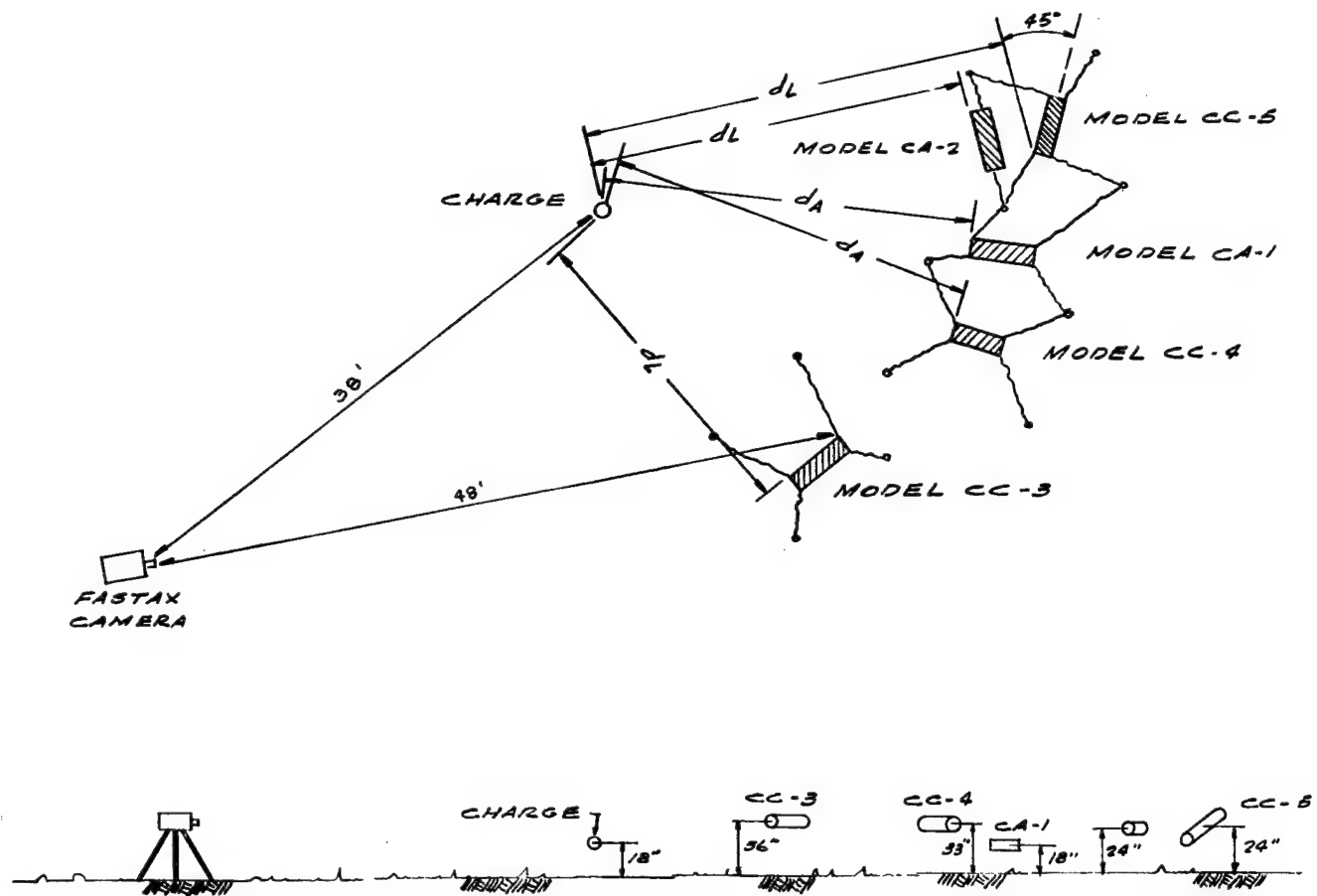


FIGURE II. 7. MODEL POSITIONS FOR SHOTS C1 AND C2

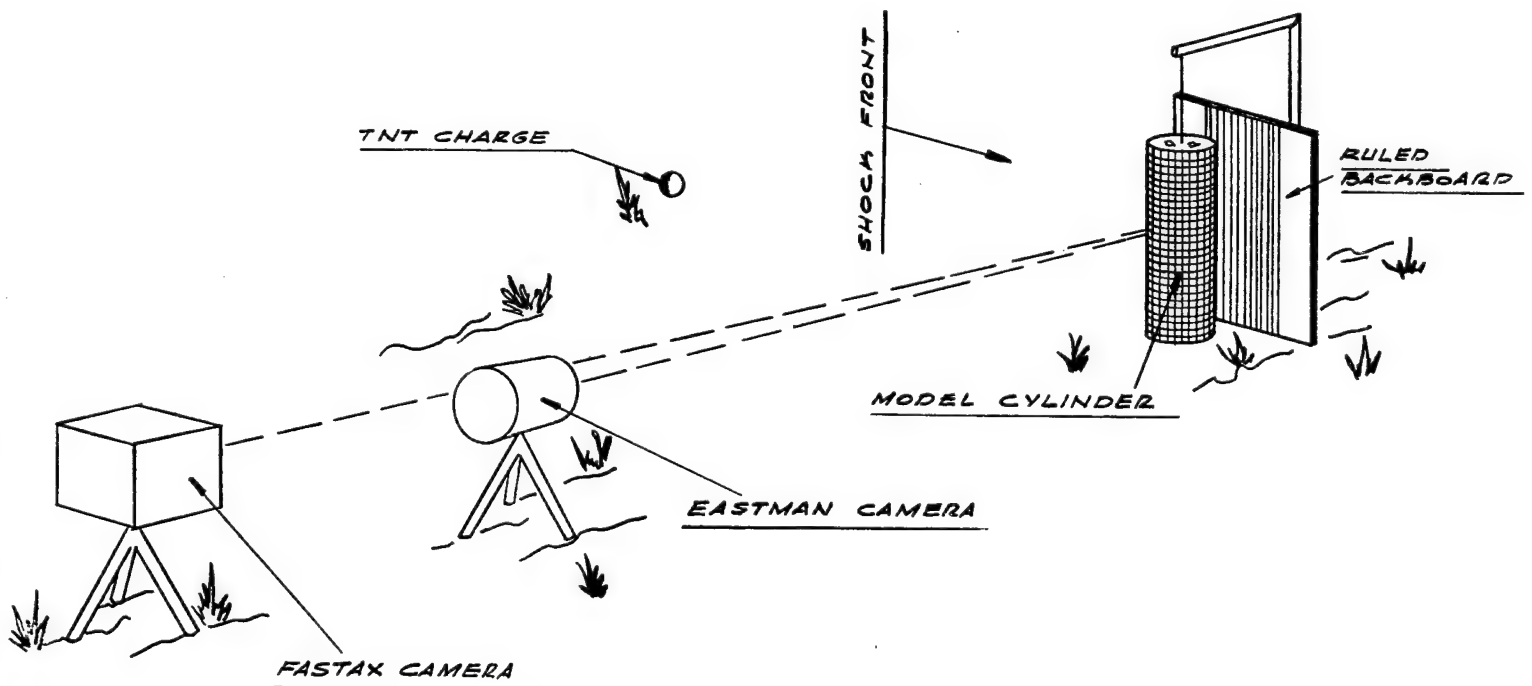


FIGURE II. 8. MODEL POSITIONS FOR SHOTS D, F, G, AND H

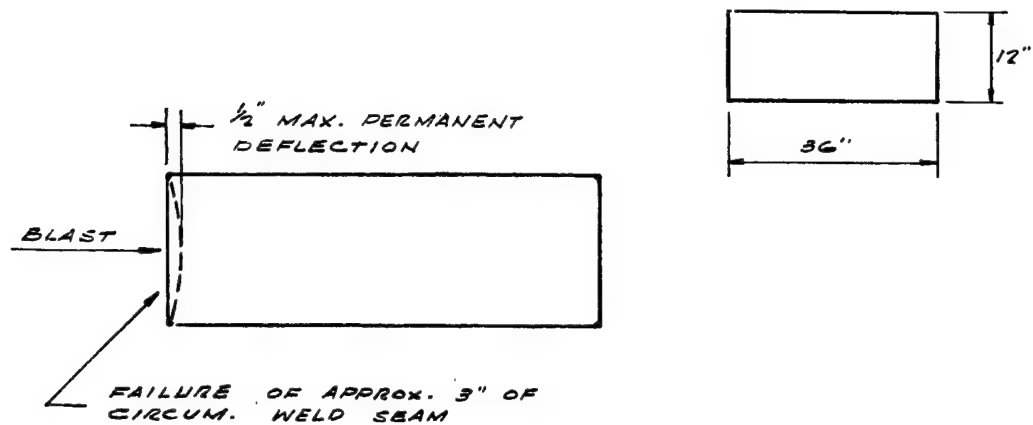


FIGURE II. 9. END PLATE FAILURE IN  
MODEL CC1 AFTER SHOT A3

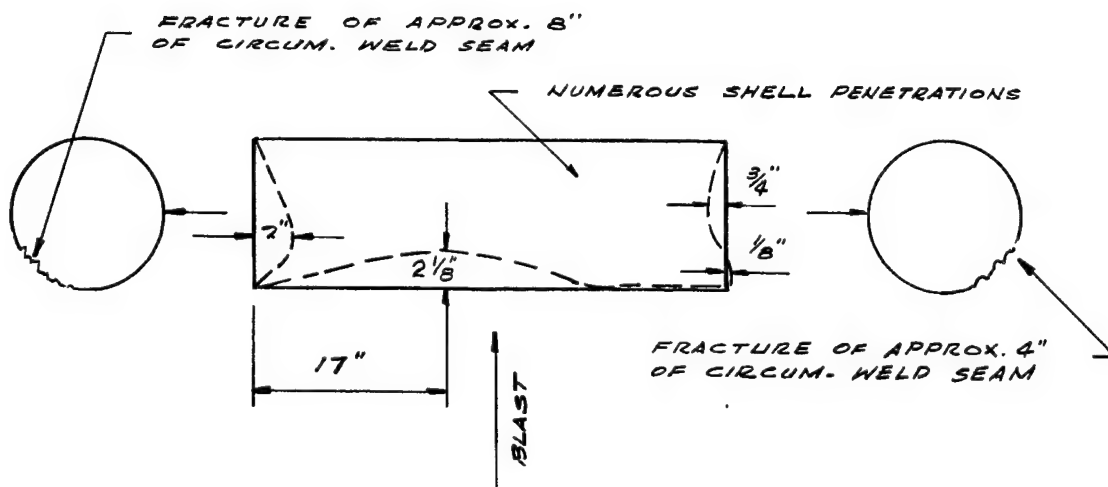


FIGURE II. 10. END PLATE AND SHELL FAILURE  
IN MODEL CC1 AFTER SHOT B3

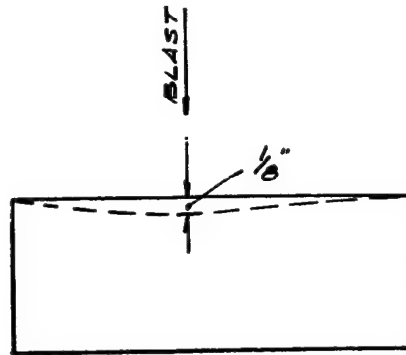


FIGURE II. 11. SLIGHT REDUCTION IN SHELL DIAMETER  
IN MODEL CC2 AFTER SHOT B1

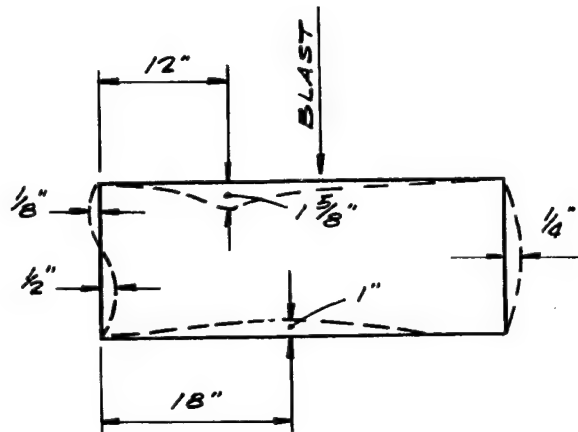


FIGURE II. 12. SHELL AND END PLATES PERMANENT  
DEFORMATIONS IN MODEL CC2 AFTER SHOT B2

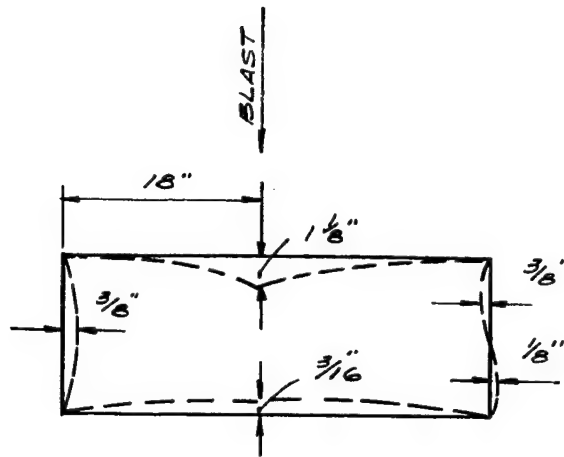


FIGURE II. 13. SHELL AND END PLATE PERMANENT DEFORMATIONS IN MODEL CC3 AFTER SHOT C1

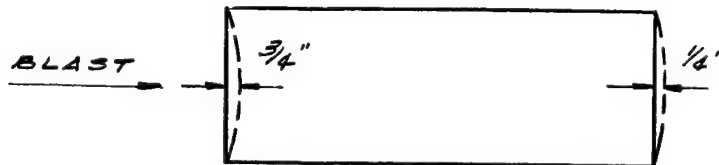


FIGURE II. 14. END PLATE DEFORMATIONS IN MODEL CC4 AFTER SHOT C7

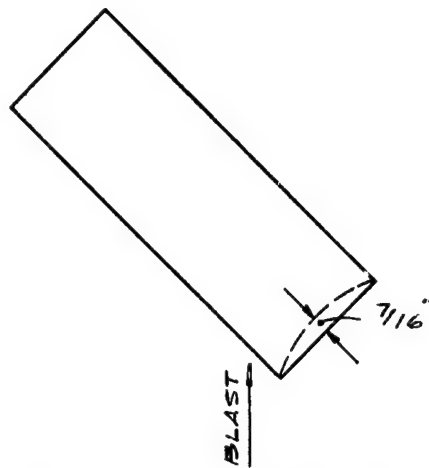


FIGURE II. 15. END PLATE DEFORMATION IN MODEL CC5  
AFTER SHOT 8

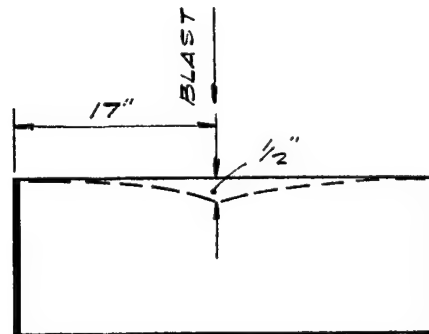
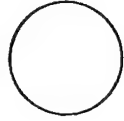
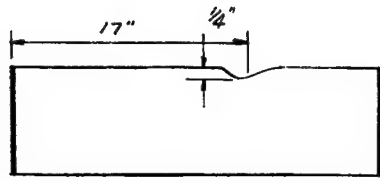
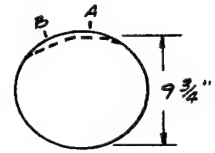
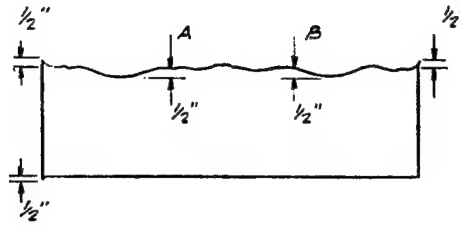


FIGURE II. 16. SHELL DEFORMATION IN MODEL CA2  
AFTER SHOT 7



MODEL CA3  
AFTER SHOT D3

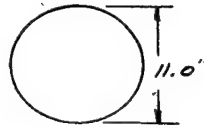
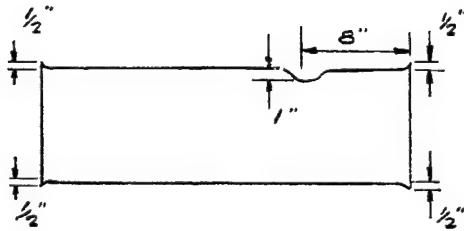
A



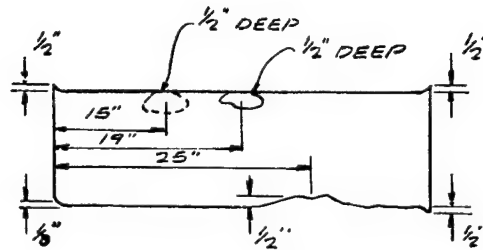
MODEL CB1  
AFTER SHOT F2

SHOCK FRONT  
↓

B



MODEL CB2  
AFTER SHOT H1



MODEL CB3  
AFTER SHOT H4

D

FIGURE II. 17. FAILURE STATE OF MODELS USED IN SHOTS D, F, AND H

## APPENDIX III

### EXPERIMENTAL RESULTS

#### III.1. PRESSURE-TIME MEASUREMENTS

In developing the experimental portion of the program, consideration was given to creating blast phenomena with conventional, chemical high explosives which, when applied in an analysis procedure to scaled models of missile bodies, would provide a discernible equivalence for the nuclear weapon effects on actual missile structures. To this end, full use was made of the information available in Reference III.1, as well as other supporting publications containing information on HE explosions.

The peak shock overpressure, as related to distance, plays a leading role in explosion-damage correlations. Selection of the controlling parameters for the HE blast phenomena, therefore, began with the relation shown in Figure III.1 between the peak overpressure in free air and scaled (radial) range as proposed by the Kirkwood-Brinkley theory<sup>(III.2)</sup> and substantiated by the experimental evidence of Fisher<sup>(III.3)</sup> and Weibull<sup>(III.4)</sup>. In this relation, the scaled range is defined as

$$\lambda = \frac{R}{(W)^{1/3}}$$

where

R is the radius (feet)

W is the weight (yield) (pounds)

Since the HE explosions would take place on or near the ground, other blast phenomena associated with surface or near surface bursts were taken into account. Foremost among these considerations was the ground reflection of the blast wave and the subsequent coalescence of the incident and reflected waves in the development of the Mach stem.

In accordance with one definition, let  $W_R$  be the size of burst exploded over a reflector at a height of burst equal to  $h_R$ . At a slant range of  $R_R > 2 h_R$  (thereby placing the point in question in the far Mach region), the reflected peak overpressure is  $P_R$ . For a free-air burst of  $W_I$ , the incident (or free-air) peak overpressure at a range of  $R_I$  equal to  $R_R$  would be  $P_I$ . Let the yield of  $W_I$  be such that, at a range of  $R_I = R_R$ , the incident and reflected peak overpressures are equal. Since the scaled slant ranges are

$$\lambda_R = \frac{R_R}{(W_R)^{1/3}} \qquad \lambda_I = \frac{R_I}{(W_I)^{1/3}}$$

by definition

$$R_F \text{ (reflection factor)} = \frac{W_I}{W_R} \left( \frac{\lambda_R}{\lambda_I} \right)^3$$

Accordingly, for a given  $W_R$  at height of burst  $h_R$ , one would expect at a range of  $R_R$  a reflected peak overpressure in the Mach reflection region equal to that obtained from a free-air burst with a yield of  $R_F W_I$ .

An indication of the reflection factor to be expected in the Mach reflection was obtained from the information presented in Figure III.2 relating the reflection factor for TNT to the scaled height of burst for a particular (and not necessarily ideal) reflecting surface. This and the additional information for pentolite and the related data for nuclear bursts indicated that scaled heights of bursts could be selected such that the reflection factor in the far Mach region would be between 0.5 and 2.0, approximately. In Figure III.1 are shown the R-W curves for these two extremes relating the reflected peak overpressure with the scaled slant range. The curves in Figure III.3 provide the same information for a nonscaled range.

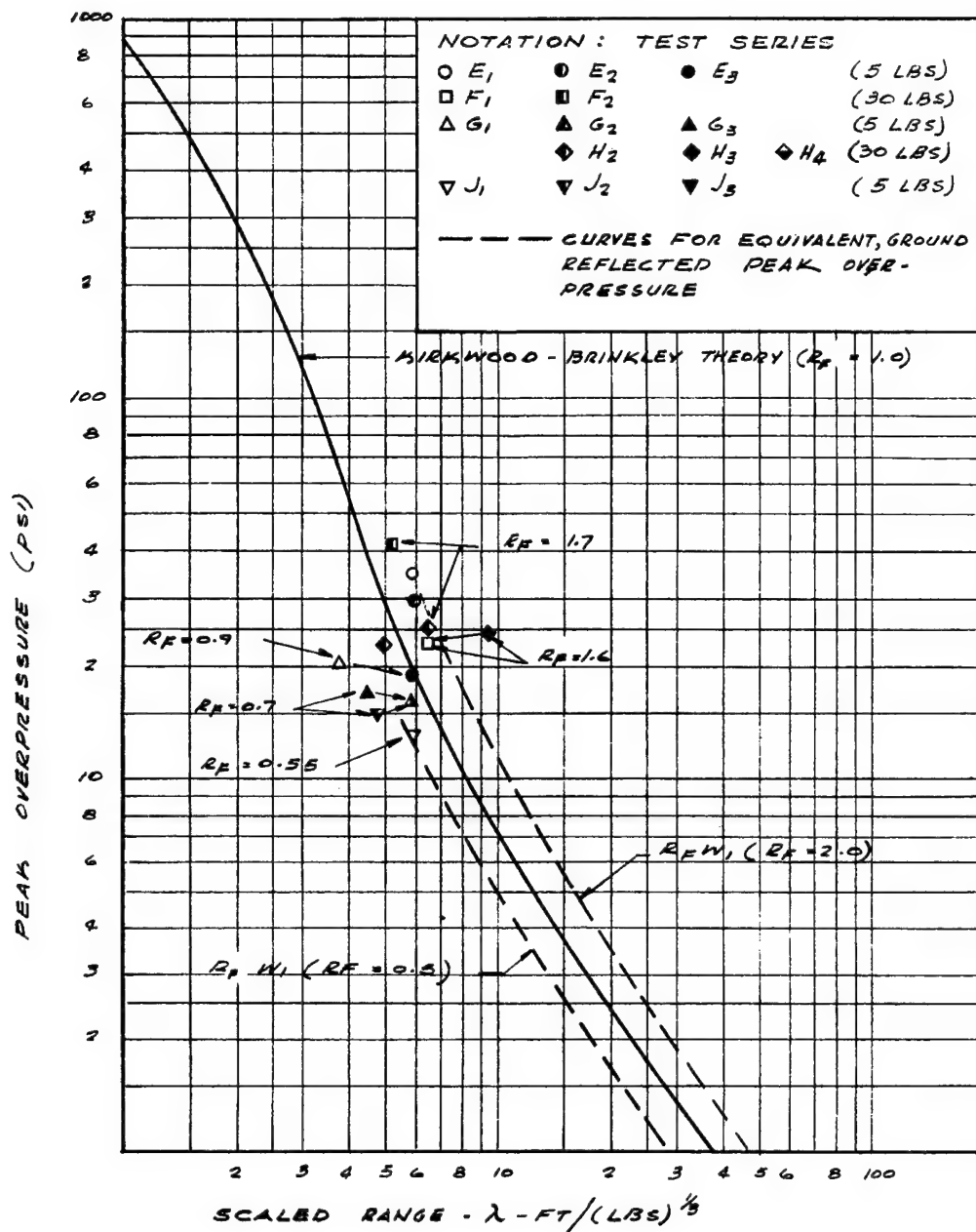


FIGURE III. 1. PEAK OVERPRESSURE VS SCALED DISTANCE FOR SPHERICAL TNT IN FREE-AIR AT SEA LEVEL

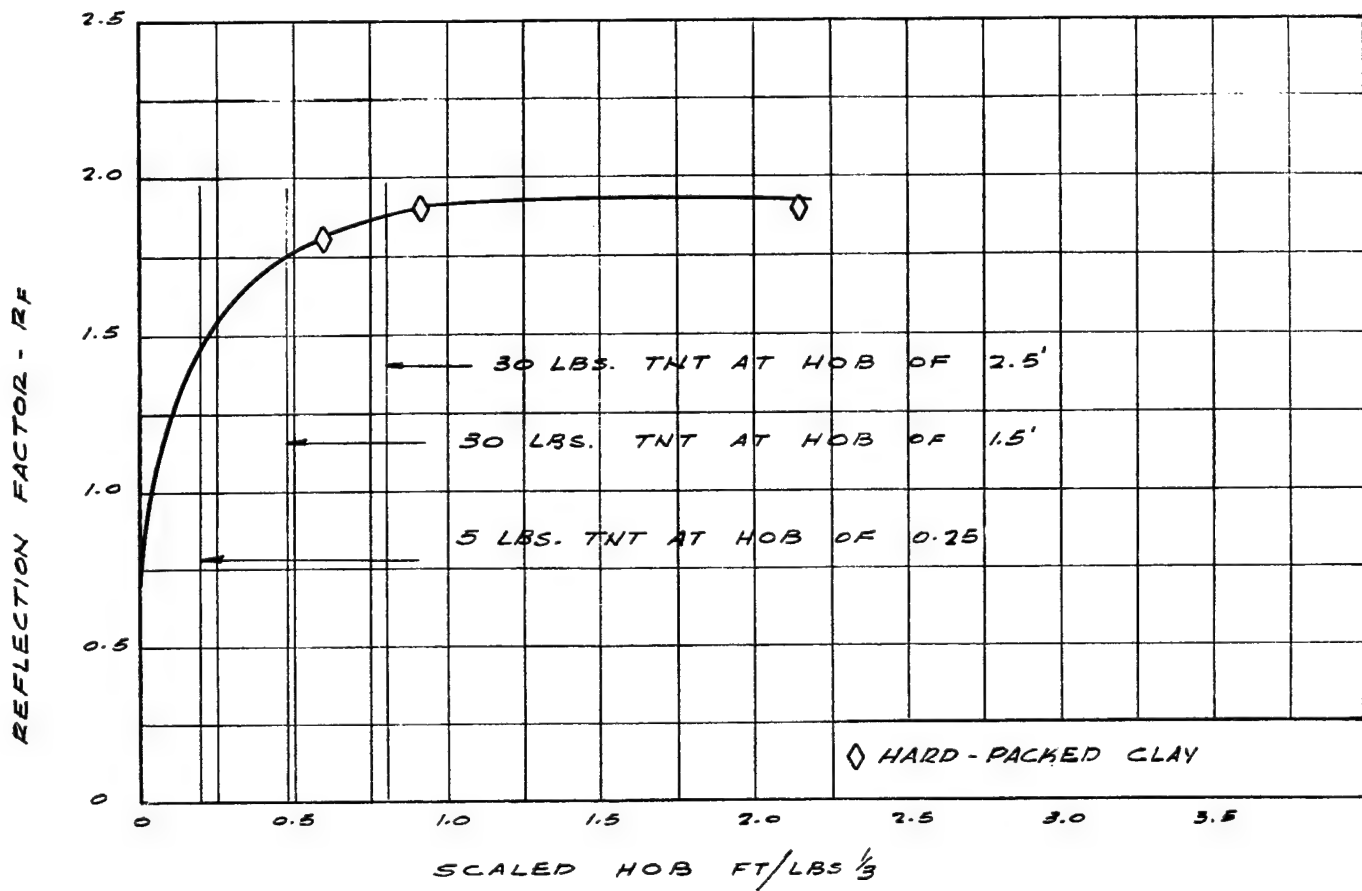


FIGURE III. 2. REFLECTION FACTORS FOR TNT EXPLOSIONS  
AT LOW HOB OVER VARIOUS SURFACES

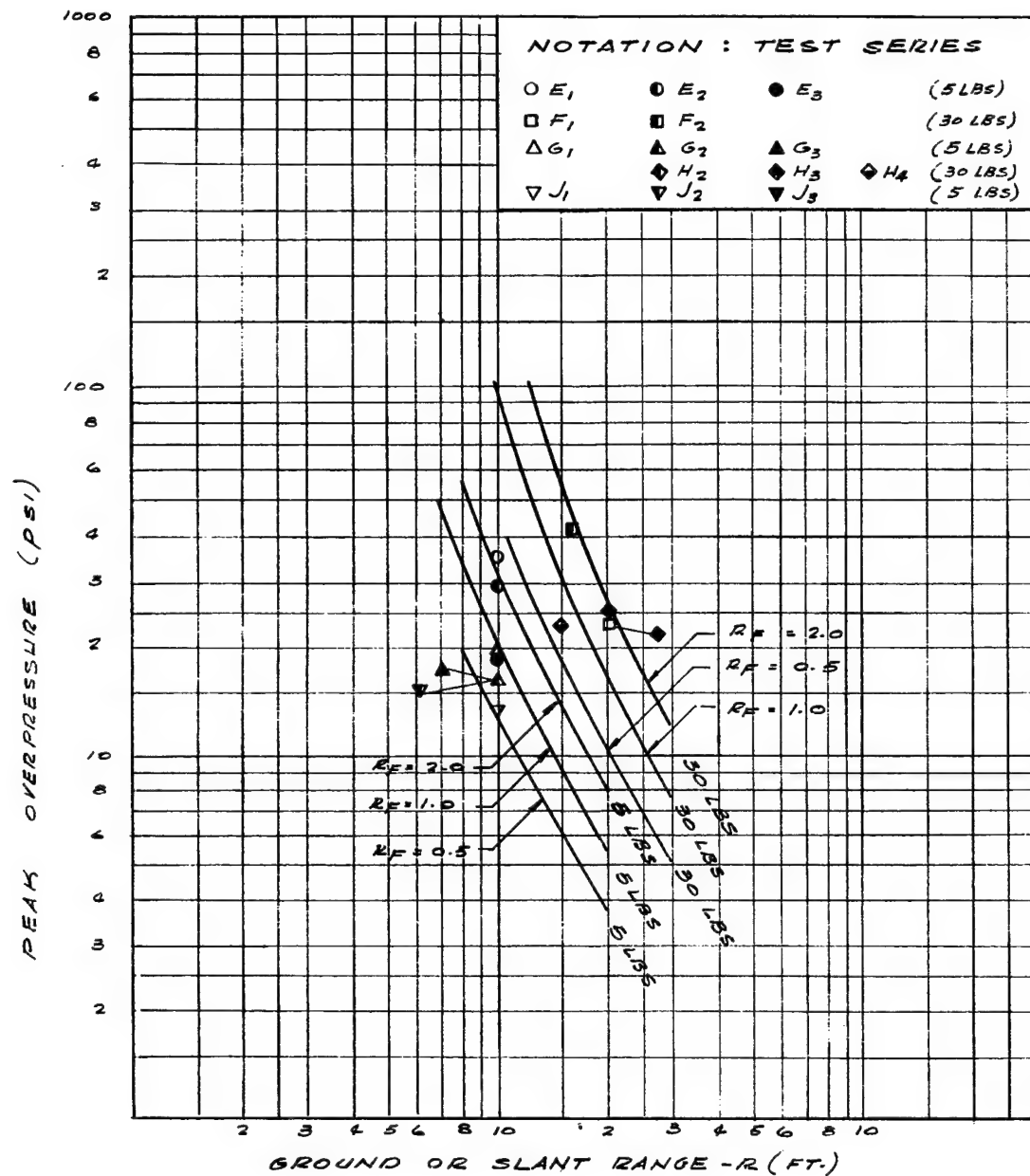


FIGURE III. 3. PEAK OVERPRESSURE VERSUS RANGE FOR TNT

Since the above method of predicting the reflected peak overpressure was limited to the far Mach region and in order to avoid having the missile model experience two pressure peaks in the regular reflection region, the charge size, height of burst and the ground range were selected such that the triple point would be above the uppermost portion of any model, regardless of its orientation.

The information in the literature provided the necessary relation between the Mach stem height and the range for various heights of burst. From prior qualitative tests, it was known that the missile models would sustain damage from a 30-lb charge of TNT at a ground range of 15 to 26 feet, depending on the orientation and construction of the model itself. The model positioned with its longitudinal axis perpendicular to ground represented the most severe, triple-point height requirement. For this arrangement and a ground range of 12 feet, the scaled height of burst would be limited to a scaled HOB of 0.8 or less or, for a charge weight of 30 lb of TNT, a burst elevation above ground of 2-1/2 feet or less. Referring to Figure III.2, this height of burst would provide a reflection factor of approximately 1.8 and therefore ground reflection, peak overpressures at the model of from approximately 15 to 100 psi depending on the ground range.

It was recognized that such factors as the actual ground reflection characteristics at the test site, the type of charge and the charge shape would all somewhat influence the blast phenomena. Accordingly, pressure measuring devices were used to determine, among other things, the extent of the deviation (if any) of the predicted peak overpressure. (See Appendix II.)

The results of these pressure readings (shown as points superimposed on the curves shown in Figures III.1 and III.2) are especially encouraging particularly in view of the uncertainties normally associated with blast phenomena measurements. It is seen that with the exception of the 30-lb, H4 shot and the 5-lb, E1 and E2 shots, a ground reflection factor of between 1.6 and 1.7 for the 30-lb shots and of 0.7 for the 5-lb shots is quite valid. The values for  $R_F$  were used for predicting the peak reflected overpressures in those tests where pressure measurements were not obtained. Table III.1 summarizes the pertinent peak overpressure and reflection factor data.

In addition to the overpressures, the other blast parameters which significantly influence the extent to which the model is damaged are the positive phase duration and the positive impulse. The time of arrival of the blast wave is of importance in the establishment and interpretation of the model's high-speed photography data.

Available free-air curves for arrival time, positive phase duration and positive impulse for TNT provided suitable approximations for adjusting the pressure recording and high-speed photography equipment. Table III.2 offers a comparison between measured and predicted data. A summary of the pressure data is given in Table III.3.

### III.2. HIGH-SPEED PHOTOGRAPHY DATA

The variation of the radial displacement at  $x = L/2$ ,  $\phi = 0^\circ$  with time (where  $t = 0$  denotes the arrival of the blast wave at the cylinder's leading edge) is shown in Figures III.4 through III.13. Each of the curves was fitted to points obtained from either prints or projections of each individual frame.

The curves in Figures III.8 and III.10 need some additional interpretation. The model (CB2) used in shot H1 had been previously subjected to four, 5-lb explosions in shot series G. These smaller (but repeated exposures) resulted in a slight permanent set at the cylinder's top, leading edge adjacent to the grooved (for simple support) end plates. In the subsequent shot H1, this edge of the shell moved out of the groove at approximately 1.7 msec (see Figure III.8) after the arrival of the blast wave. In so doing, the subsequent response of the shell was no longer that of a cylinder with simple supports at each boundary. However, prior to that time, the shell's response followed the theoretically predicted displacement pattern.

The same mode of failure was experienced by Model CB3 (Figure III.10) in shot H4. Here, the shell's leading edge at the top end-plate began to move out of the groove at approximately 1.5 msec. Although the shell did subsequently return to zero displacement at  $x = L/2$ ,  $\phi = 0^\circ$ , the condition of simple support was no longer in effect. For this reason, the simple-support response was limited to that portion of the displacement curve prior to 1.5 msec.

TABLE III. 1. PEAK OVERPRESSURE IN MACH REFLECTION  
REGION (EXPERIMENTAL DATA)

Shot No.	Charge <sup>(1)</sup> (lb)	HOB <sup>(2)</sup> (ft)	Ground <sup>(3)</sup> Range (ft)	(A)		(B)	(C)	(D)	(E)
				R <sub>F</sub> = 0.5	R <sub>F</sub> = 2.0	R <sub>F</sub>			
E1	5	0.33	10	12.8	33.0	1.32	25.1	35.0	2.0
E2	5	0.33	10	12.8	33.0	1.32	25.1	29.3	1.6
E3	5	0.33	10	12.8	33.0	1.32	25.1	18.8	0.9
F1	30	1.5	20	10.5	27.2	1.89	27.0	23.0	1.6
F2	30	1.5	16	16.3	47.0	1.89	46.4	41.0	1.7
G1	5	0.33	10	12.8	33.0	1.32	25.1	19.7	0.9
G2	5	0.33	10	12.8	33.0	1.32	25.1	16.1	0.7
G3	5	0.33	10	12.8	33.0	1.32	25.1	16.5	0.7
G4	5	0.33	10	12.8	33.0	1.32	25.1	N. A.	N. A.
H2	30	2.5	20	10.5	27.2	1.89	27.0	24.6	0.7
H3	30	2.5	20	10.5	27.2	1.89	27.0	23.0	1.6
H4	30	2.5	15	18.5	55.9	1.89	54.0	53.0	1.6
J1	5	0.33	10	12.8	33.0	1.32	25.1	13.1	0.6
J2	5	0.33	10	12.8	33.0	1.32	25.1	16.2	0.7
J3	5	0.33	5	39.2	140.0	1.32	102.0	64.0	0.7

N. A. Not available.

(1) Flaked TNT.

(2) Height of burst.

(3) Distance from ground zero to model and/or pressure pickup.

(A) Estimated range of peak overpressure in Mach reflection region (psi);  
Kirkwood-Brinkley theory - see Figures III. 1 and III. 3.

(B) Reflection factor for hard clay surface as function of HOB (see Figure III. 2).

(C) Peak overpressure based on R<sub>F</sub> from Column (B).

(D) Experimentally measured peak overpressure (psi).

(E) Adjusted reflection factor based on measured peak overpressure.

TABLE III.2. TIME OF ARRIVAL, POSITIVE PHASE DURATION  
IN MACH REFLECTION REGION (EXPERIMENTAL DATA)

Shot No.	Charge <sup>(1)</sup> (lb)	HOB <sup>(2)</sup> (ft)	Ground <sup>(3)</sup> Range (ft)	(A) (msec)	(B) (msec)	(C) (msec)	(D) (msec)
D1	30	2.5	26	11.5	N. A.	---	---
D2	30	2.5	22	9.3	7.9	---	---
D3	30	2.5	16	5.0	5.3	---	---
E1	5	0.25	10	3.4	N. A.	2.6	2.7
E2	5	0.25	10	3.4	N. A.	2.6	2.8
E3	5	0.25	10	3.4	N. A.	2.6	2.2
F1	30	1.5	20	7.4	N. A.	5.1	4.2
F2	30	1.5	16	4.9	N. A.	4.0	4.3
G1	5	0.25	10	3.4	4.5	2.6	2.4
G2	5	0.25	10	3.4	3.9	2.6	2.3
G3	5	0.25	10	3.4	3.9	2.6	2.5
G4	5	0.25	10	3.4	3.8	2.6	2.7
H1	30	2.5	20	7.4	7.1	5.1	N. A.
H2	30	2.5	20	7.4	N. A.	5.1	6.0
H3	30	2.5	20	7.4	N. A.	5.1	~4.5
H4	30	2.5	15	3.7	N. A.	3.9	N. A.
J1	5	0.25	10	3.4	N. A.	2.6	3.1
J2	5	0.25	10	3.4	N. A.	2.6	3.4
J3	5	0.25	5	1.2	N. A.	1.6	1.1

N. A. Not available.

(1) Flaked TNT.

(2) Height of burst.

(3) Distance from ground zero to model and/or pressure pickup.

(A) Estimated time of arrival -  $t_a$

(B) Recorded time of arrival -  $t_a$  (from high speed photography).

(C) Estimated positive phase duration -  $t_+$

(D) Recorded positive phase duration -  $t_+$

TABLE III. 3. SUMMARY OF PEAK INCIDENT OVERPRESSURES  
AND POSITIVE PHASE DURATIONS

(1) E: end-on loading; S: side-on  
loading; O: oblique loading

(2) Peak incident overpressure

(3) Positive phase duration

(4) E - elastic; F - fixed;  
S - simple support

(5) Experimental - See  
Table III. 1 or III. 2

<u>Model</u>	<u>Shot No.</u>	<u>Model (1) Orientation</u>	<u>P<sub>I</sub> (2) (psi)</u>	<u>t<sub>+</sub> (3) (msec)</u>	<u>Boundary Restraint (4)</u>
CC1	A1	E	4	7	E
↓	A2	↓	10	6	↓
↓	A3	↓	24	4	↓
↓	B1	S	18	5	↓
↓	B2	↓	23	4.5	↓
↓	B3	↓	32	4	↓
CC2	A1	↓	2	9	↓
↓	A2	↓	6	7	↓
↓	A3	↓	17	5	↓
↓	B1	↓	29	4	↓
↓	B2	↓	38	3	↓
CC3	C1	↓	31	5	↓
CC4	C1	E	22	6	↓
CC4	C2	E	27	5	↓
CC5	C1	O	13	7	↓
CC5	C2	O	17	6	↓
CA1	C1	E	22	6	↓
CA1	C2	E	27	4	F
CA2	C1	S	27	4	↓
CA3	D1	↓	15	6.5	↓
↓	D2	↓	19	5.5	↓
↓	D3	↓	42	3.8	↓
CB1	F1	↓	27	4	S
CB1	F2	↓	46	4	↓
CB2	G1	↓	20 (5)	2.4 (5)	↓
↓	G2	↓	16 (5)	2.3 (5)	↓
↓	G3	↓	17 (5)	2.3 (5)	↓
↓	G4	↓	18	2.5	↓
↓	H1	↓	25	5.1	↓
CB3	H3	↓	23 (5)	4.5	↓
CB3	H4	↓	53 (5)	3.9	↓
P1	J1	-	25	3	↓
P2	J2	-	25	3	↓
P2	J3	-	102	1	↓

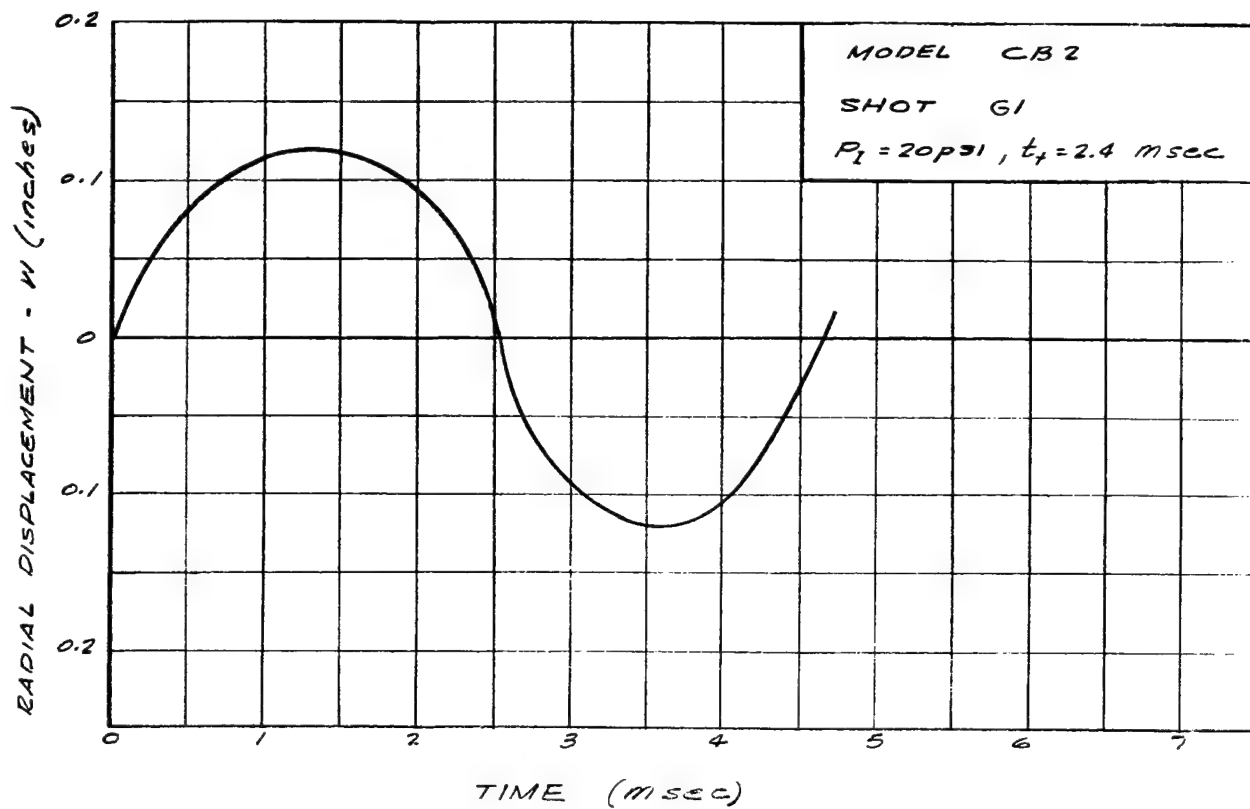


FIGURE III. 4. RADIAL DISPLACEMENTS AT  $x = L/2$ ,  $\phi = 0^\circ$  OBTAINED FROM HIGH SPEED PHOTOGRAPH OF CYLINDRICAL MODELS

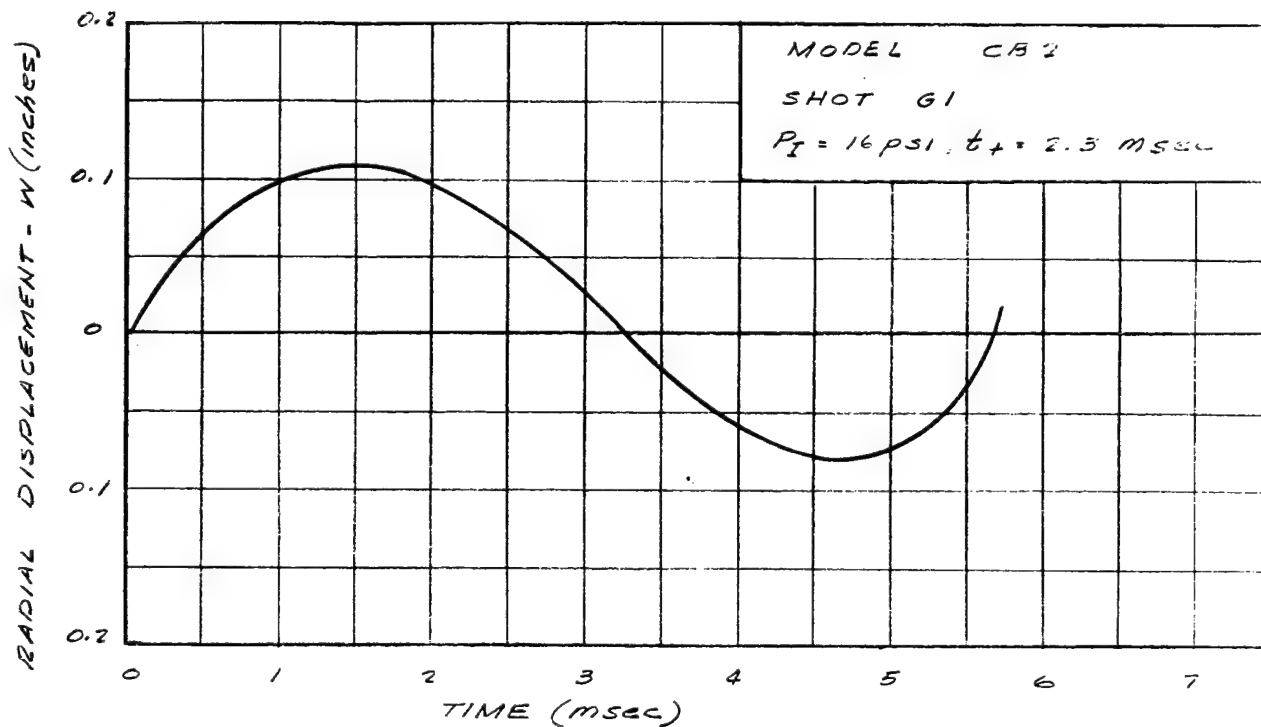


FIGURE III. 5. RADIAL DISPLACEMENTS AT  $x = L/2$ ,  $\phi = 0^\circ$  OBTAINED FROM HIGH SPEED PHOTOGRAPH OF CYLINDRICAL MODELS

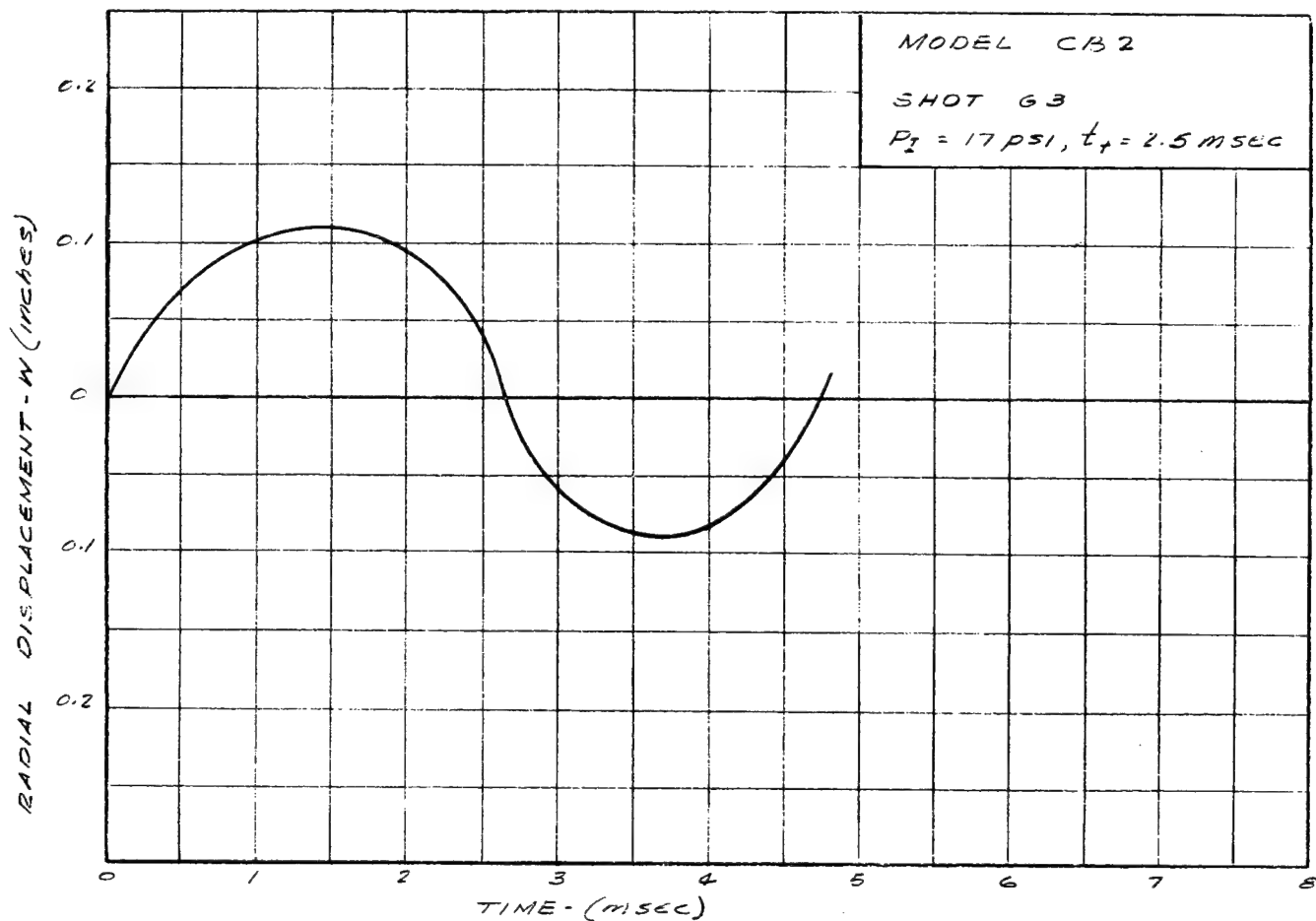


FIGURE III. 6 RADIAL DISPLACEMENTS AT  $x = L/2$ ,  $\phi = 0^\circ$  OBTAINED FROM HIGH SPEED PHOTOGRAPH OF CYLINDRICAL MODELS

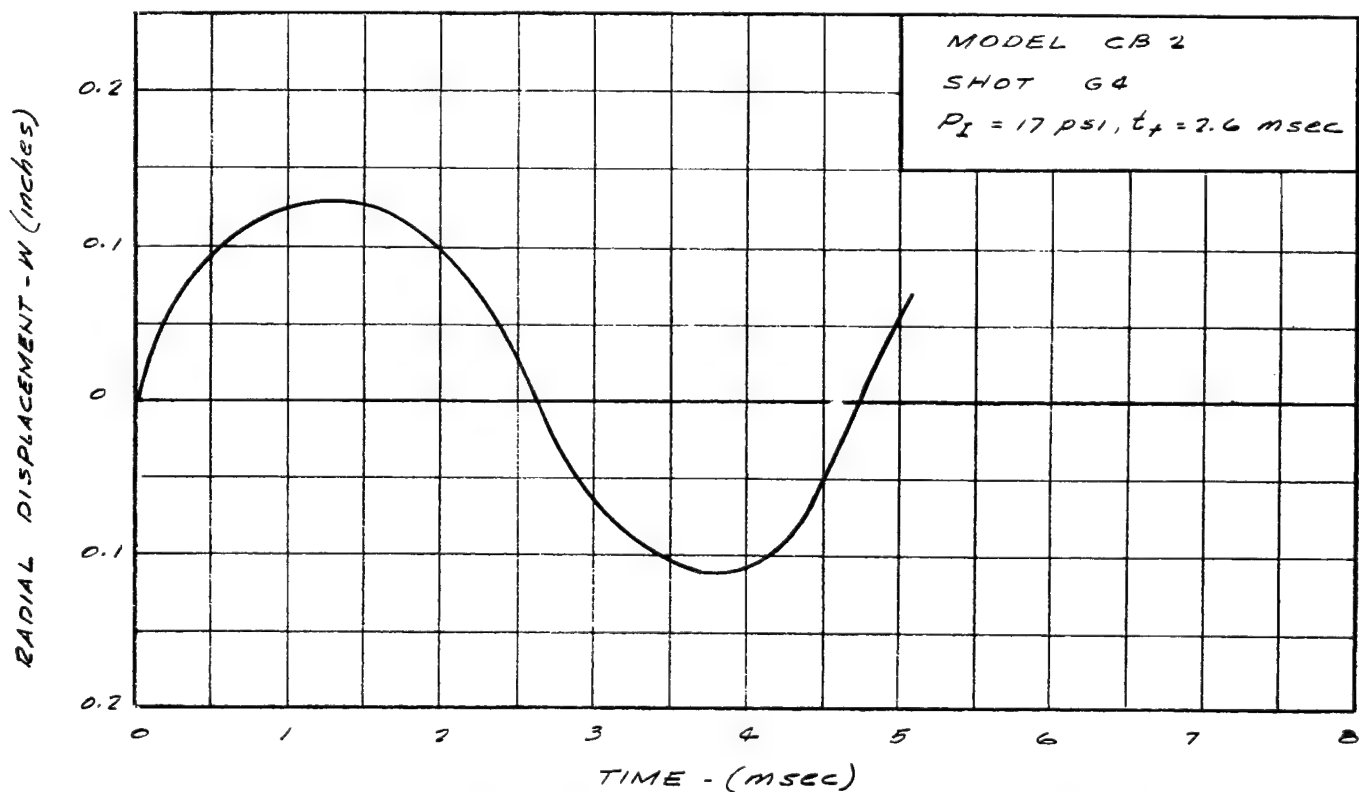


FIGURE III. 7. RADIAL DISPLACEMENTS AT  $x = L/2$ ,  $\phi = 0^\circ$  OBTAINED FROM HIGH SPEED PHOTOGRAPH OF CYLINDRICAL MODELS

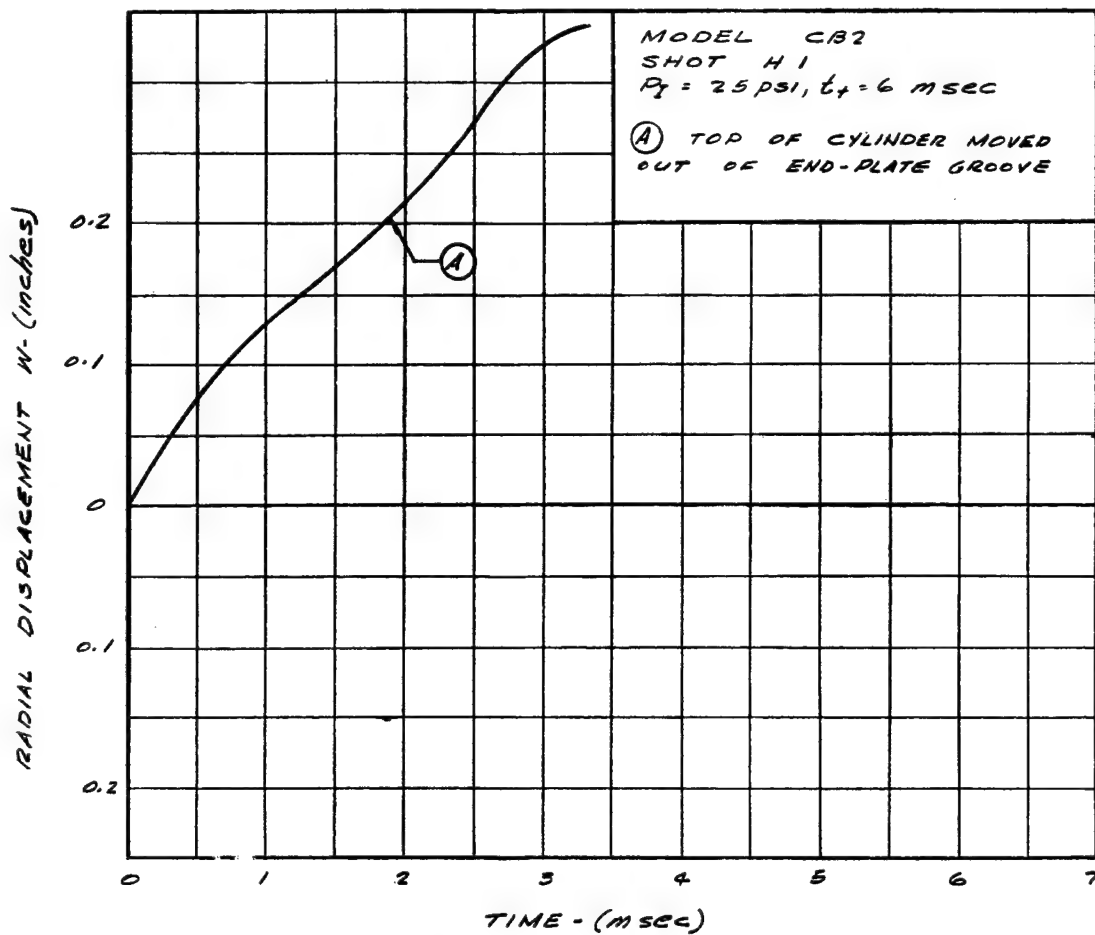


FIGURE III.8. RADIAL DISPLACEMENTS AT  $x = L/2, \phi = 0^\circ$  OBTAINED FROM HIGH SPEED PHOTOGRAPH OF CYLINDRICAL MODELS

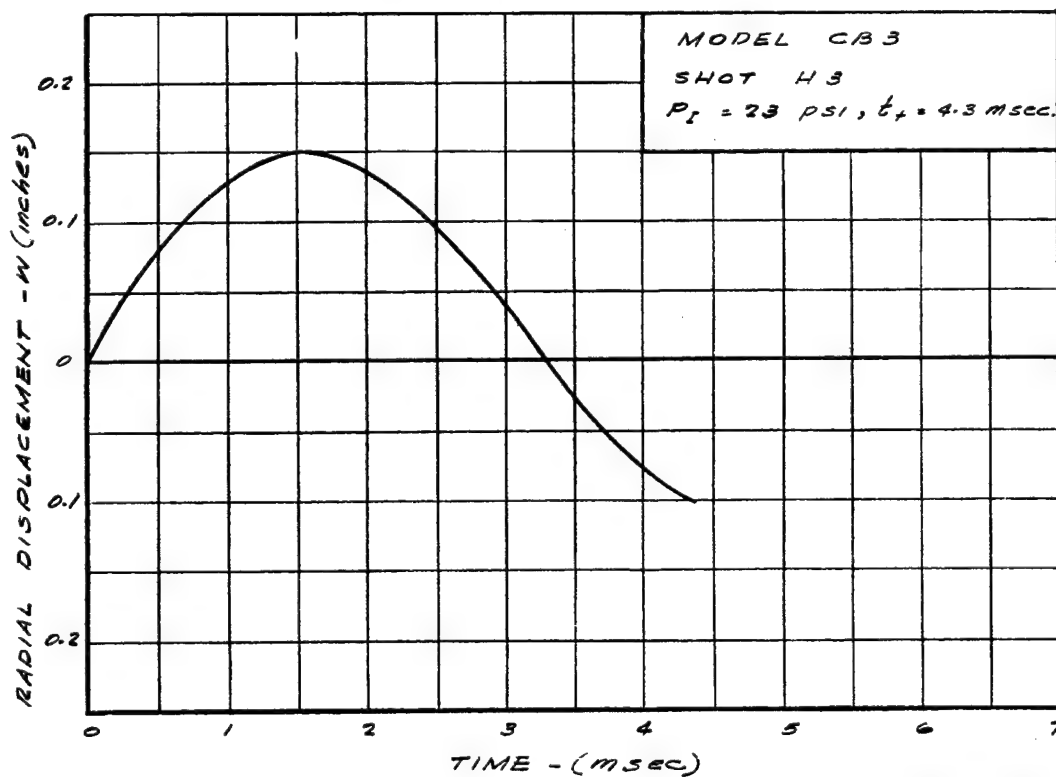


FIGURE III.9. RADIAL DISPLACEMENTS AT  $x = L/2, \phi = 0^\circ$  OBTAINED FROM HIGH SPEED PHOTOGRAPH OF CYLINDRICAL MODELS

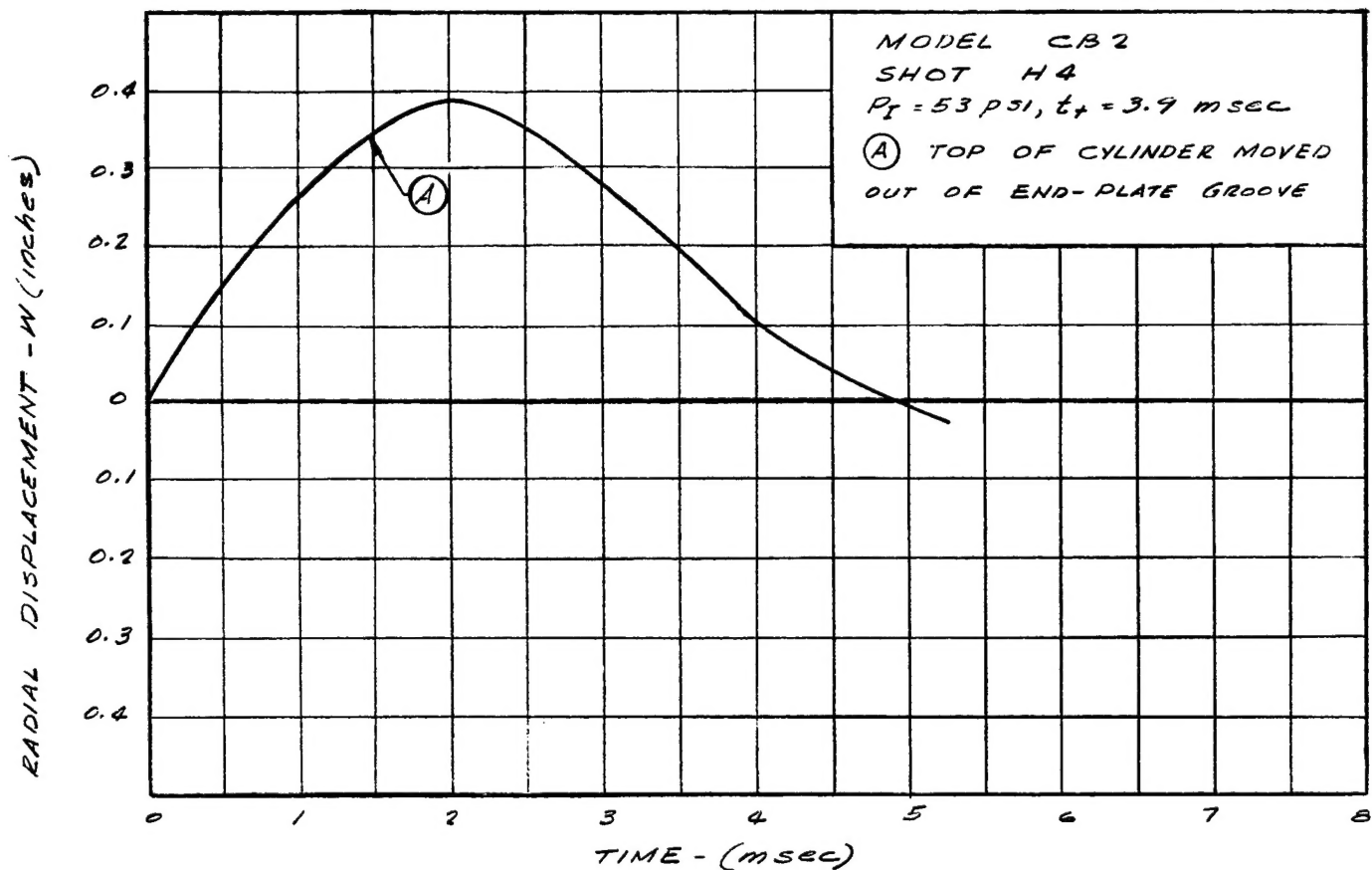


FIGURE III. 10. RADIAL DISPLACEMENTS AT  $x = L/2$ ,  $\phi = 0^\circ$  OBTAINED FROM HIGH SPEED PHOTOGRAPH OF CYLINDRICAL MODELS

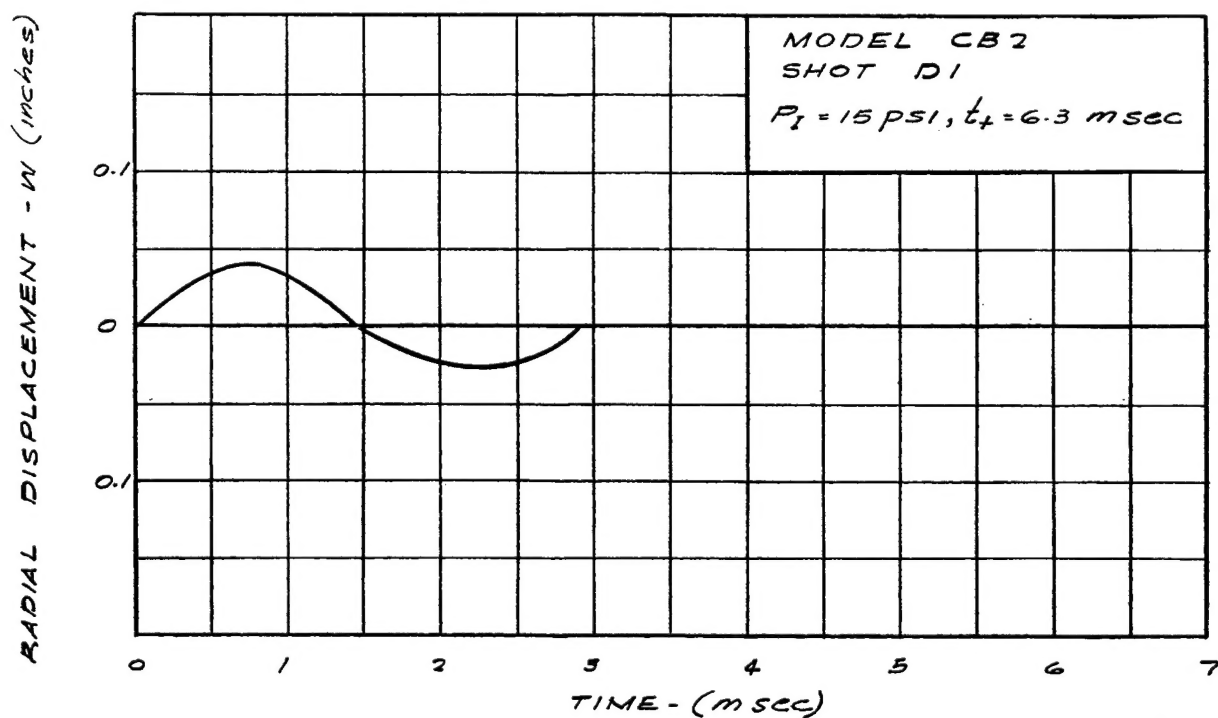


FIGURE III. 11. RADIAL DISPLACEMENTS AT  $x = L/2$ ,  $\phi = 0^\circ$  OBTAINED FROM HIGH SPEED PHOTOGRAPH OF CYLINDRICAL MODELS

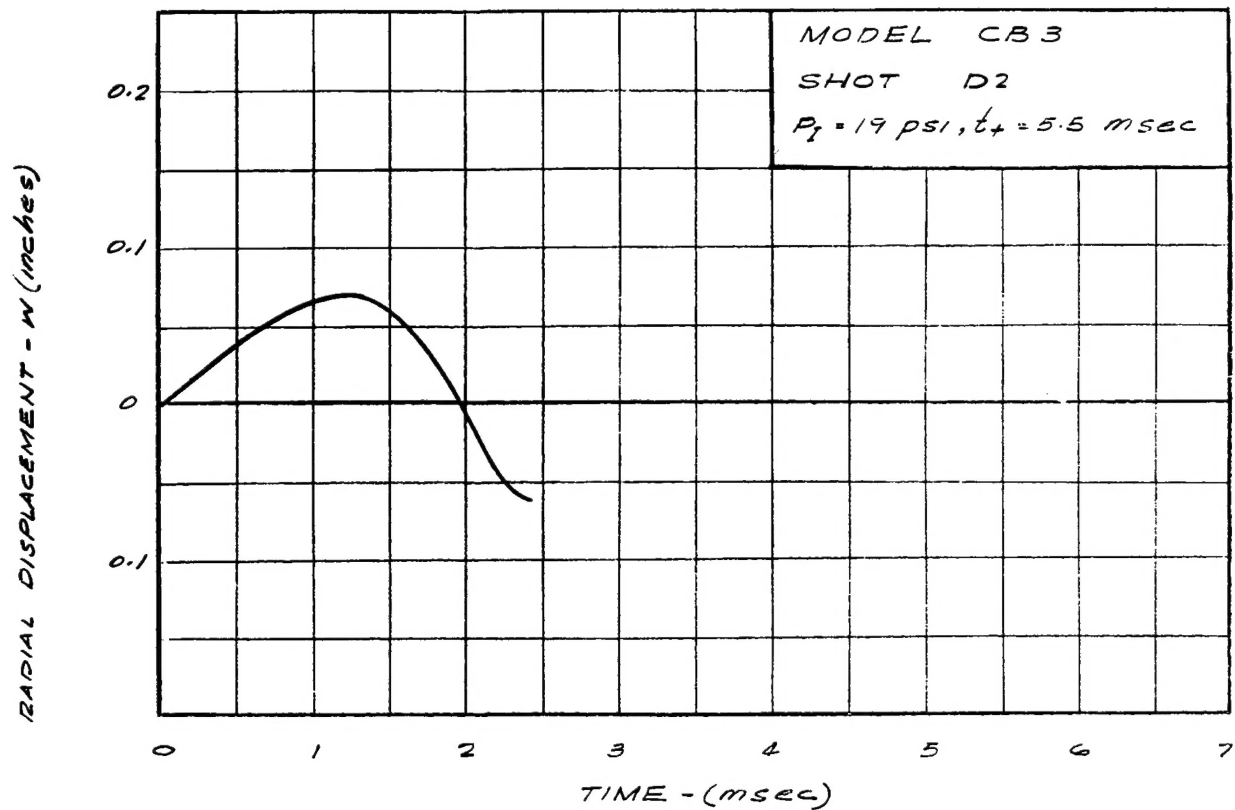


FIGURE III. 12. RADIAL DISPLACEMENTS AT  $x = L/2$ ,  $\phi = 0^\circ$  OBTAINED FROM HIGH SPEED PHOTOGRAPH OF CYLINDRICAL MODELS

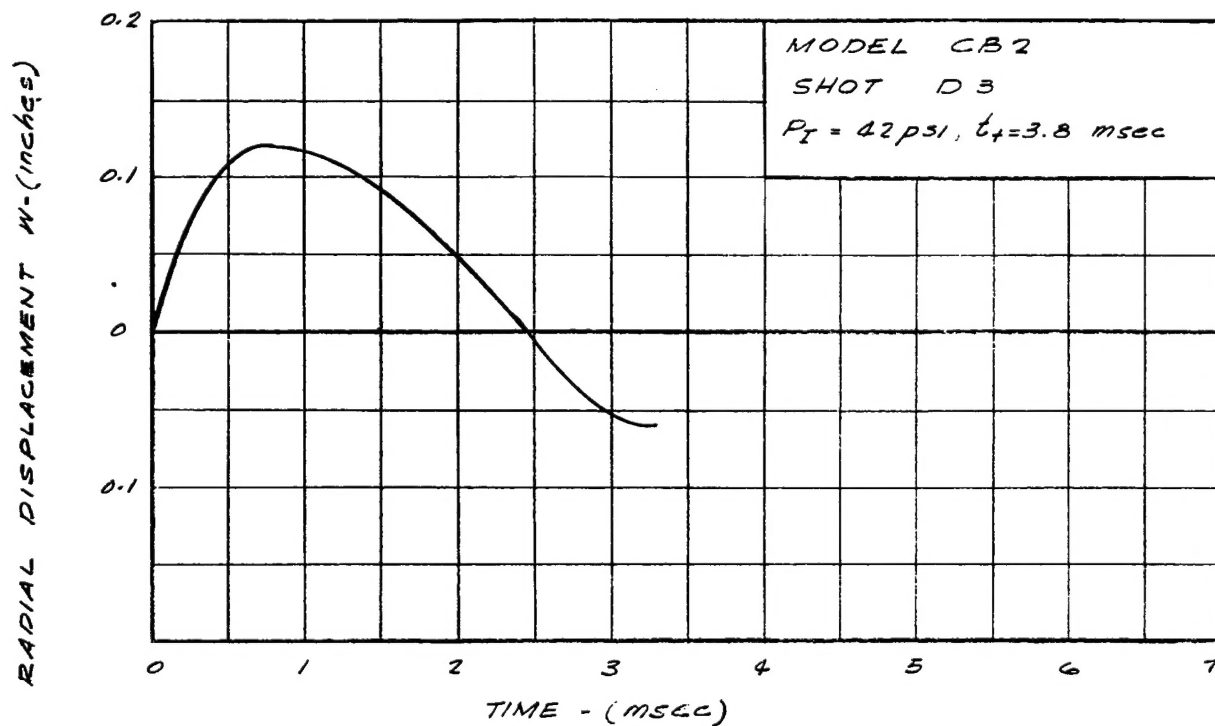


FIGURE III. 13. RADIAL DISPLACEMENTS AT  $x = L/2$ ,  $\phi = 0^\circ$  OBTAINED FROM HIGH SPEED PHOTOGRAPH OF CYLINDRICAL MODELS

### REFERENCES (APPENDIX III.)

- III. 1. Moulton, James F., Jr., Nuclear Weapons Blast Phenomena, Vols. I, II and III, Defense Atomic Support Agency, DASA 1200, March 1960, (Secret).
- III. 2. Kirkwood and Brinkley, "Theoretical Blast Wave Curves for Cast TNT," OSRD 5481, NDRC A-341, Aug. 1945 (Unc.).
- III. 3. Fisher, "Spherical Cast TNT Charges, Air Blast Measurements on," NOLM-10780, Jan. 1950 (Unc.).
- III. 4. Weibull, "Explosion of Spherical Charge in Air," BRL Translation Report X-127, Feb. 1950 (Unc.).

Aeronautical Systems Division, Dir/Aero-  
mechanics, Flight Dynamics Lab, Wright-  
Patterson AFB, Ohio.  
Rpt No. ASD-TDR-62-475. RESPONSE OF MISSILE  
STRUCTURES TO IMPULSE LOADING. Final report,  
Mar 63, 102p. incl illus., tables, 17 refs.

Unclassified Report

Procedures for analytically predicting the  
response of missile bodies to blast loadings  
are presented. The investigation involves  
the behavior of cylindrical shells (with  
various end-closures) and circular, flat  
plates. The numerical results obtained from  
the analytical methods compare favorably with

( )  
( over )

the experimental data acquired during the  
study.

1. Structural shells  
2. Dynamics  
3. Missile damage

I. AFSC Project 6906,  
Task 690601

II. Contract No.  
AF 33(616)-7956

III. Southwest Res.

Inst., San Antonio  
Texas

IV. T. Wah, et al.

V. Aval fr OTS

VI. In ASTIA collection

Aeronautical Systems Division, Dir/Aero-  
mechanics, Flight Dynamics Lab, Wright-  
Patterson AFB, Ohio.

Rpt No. ASD-TDR-62-475. RESPONSE OF MISSILE  
STRUCTURES TO IMPULSE LOADING. Final report,  
Mar 63, 102p. incl illus., tables, 17 refs.

Unclassified Report

Procedures for analytically predicting the  
response of missile bodies to blast loadings  
are presented. The investigation involves  
the behavior of cylindrical shells (with  
various end-closures) and circular, flat  
plates. The numerical results obtained from  
the analytical methods compare favorably with

( )  
( over )

the experimental data acquired during the  
study.

1. Structural shells  
2. Dynamics  
3. Missile damage

I. AFSC Project 6906,  
Task 690601

II. Contract No.  
AF 33(616)-7956

III. Southwest Res.

Inst., San Antonio  
Texas

IV. T. Wah, et al.

V. Aval fr OTS

VI. In ASTIA collection